Doctoral Thesis

Analytical Modeling of Pneumatic Soft Grippers Based on Finite-Strain Membrane and Beam Theories

September 2022

Doctoral Program in Advanced Mechanical Engineering and Robotics
Graduate School of Science and Engineering
Ritsumeikan University

SACHIN

Doctoral Thesis Reviewed
by Ritsumeikan University

Analytical Modeling of Pneumatic Soft Grippers Based on Finite-Strain Membrane and Beam Theories

(有限ひずみ膜理論と梁理論に基づく空気圧ソフトグリッパの解析的モデリング)

September 2022

2022 年 9 月

Doctoral Program in Advanced Mechanical Engineering and Robotics

Graduate School of Science and Engineering

Ritsumeikan University

立命館大学大学院理工学研究科

機械システム専攻博士課程後期課程

SACHIN

サチン

Supervisor：Professor HIRAI Shinichi

研究指導教員：平井　慎一　教授

Abstract

Soft actuators are compliant structures that are generally made of elastomers and generate large deformations. Finite deformation is the principal actuation basis of elastomer-based pneumatic soft actuators. Desired deformation behavior is the key design requirement for such actuators. The behavior of these structures is complex due to the presence of both geometric and material nonlinearities. The objective of soft robotics applications is the controlled large deformation of these structures. This dissertation is focused on studying the behavior of two such pneumatic soft actuators: 1) flat shell actuator and 2) pneu-net actuator. Analytical models of the actuators are developed for various states.

The objective of flat shell actuator model is to optimize its design and investigate its interaction with a cylindrical object. The cylindrical object grasp is a case of partial contact, and such interactions need special consideration on object geometry, especially in case of inflatable actuators. Here, the grasping operation is governed by the deformed shape of actuator, and is highly dependent on object geometry. The model is based on finite-strain membrane theory and neo-Hookean material. The developed model considers contact interaction of the actuator with both flat and cylindrical rigid substrates. The model is developed for three different states of the actuator: 1) free-space; 2) contact with a flat substrate; and 3) contact with a cylindrical substrate. In application, the model is used to predict the relative position and air pressure required to grasp a cylindrical object using a parallel two-finger shell gripper.

The pneu-net actuator model is based on the Euler–Bernoulli finite-strain hyperelastic thin cantilever beam theory. The deformation of actuator air chambers is modeled using finite-strain membrane theory. The analytical model is developed for two different states of the actuator: 1) free space and 2) when the actuator is subjected to tip contact. The theoretical formulation of the developed model is different from previously developed infinitesimal-strain models of the actuator, since it considers axial stretch and forces applied to the actuator. In addition, it can be theoretically implemented on similar structured actuators for various applications.

The developed analytical models predict deformation and force characteristics of the actuators. The models involve solving nonlinear algebraic and differential equations and are

computationally efficient. The analytical model predicted deformation and force characteristics of the pneu-net actuator are compared with the finite element (FE) model. The results suggest that the developed model can predict deformation and force characteristics of the actuator as accurately as the FE model, but the computation time of the developed model is less than 1% that of the FE model.

The analytical model predicted deformation behavior of the actuators is validated experimentally via free-space deformation, force measurement, and grasping tests. The frictional properties of the actuators are investigated for contact scenarios similar to the grasping state. In application, the developed models are used to predict the air pressure required to attain a successful grasp. The predicted pressure is validated experimentally on two-finger flat shell and three-finger pneu-net grippers for grasping different objects.

Acknowledgements

I would like to express my sincere gratitude to my advisor Prof. Shinichi Hirai for his guidance, motivation, immense knowledge, financial aid, and continuous support in my doctoral study. His guidance helped me in all aspects of my research and the writing of this thesis. I could not have imagined having a better advisor and mentor for my doctoral study.

I would like to heartily thank Dr Zhongkui Wang for his mentorship throughout my study. His guidance on academic report writing was very helpful in this journey. I would also like to thank Dr Takahiro Matsuno for helping me on several occasions and for being a good friend.

I would like to thank my labmates Mimori, Furuta, Iida, Sreyas, and Zheng for being good friends during this period. I would also like to thank my Indian friends for organizing holiday trips. I would also like to thank my family without whom this would have not been possible. Last but not least, I want to thank my dearest friend Bablu for his appreciation and belief in me.

I would like to dedicate this thesis to my loving family.

Table of contents

List of figures

List of tables

Nomenclature

Roman Symbols

$2a$	width of membrane or height of air chamber
$2b$	length of membrane or width of air chamber
$2h_x$	initial gap between adjacent air chambers
A_c	area of contact region
B	width of pneu-net actuator cover
C	constant that depends on Poisson's ratio and membrane dimensions
c_i	contact widths
d	offset between membrane and substrate. For pneu-net actuator, initially $d = h_x$
df	differential traction force element
ds	deformed length of beam
E	Young's modulus
$e,\ e_1,\ e_2$	deformed portion of membrane with zero curvature
e_y	eccentricity of air pressure generated axial force at air chamber contact interface
F_c	normal contact force
F_L	lifting force
F_p	eccentric axial force generated at air chamber's contact interface
F_t	traction force

F_z	component of normal contact force in Z-direction
g_x, g_y	distributed forces per unit length, acting on pneu-net actuator cover
H	thickness of pneu-net actuator cover
h	object offset (vertical) along length of flat shell gripper
H_{ext}	lifting force for pneu-net actuator
h_L	length of air chamber (along X-axis)
I_i	strain invariant
L	length of pneu-net actuator
M	bending moment acting on pneu-net actuator cover
m	distributed bending moment acting on pneu-net actuator cover
$m_h g$	weight of grasping object for pneu-net gripper
M_m, M_{p_i}, M_{g_i}, M_{F_i}	bending moments acting on beam segments
M_T	bending moment generated by air pressure on pneu-net actuator cover
mg	weight of grasping object for flat shell gripper
P	point force along X-direction or component of stress resultant
p	air pressure
p_{in}	initial guess pressure
Q	point force along Y-direction or component of stress resultant
R	radius of curvature
r	radius of cylindrical object
R_a	radius of curvature of deformed membrane along actuator width for section across contact midplane
R_c	radius of curvature of free membrane at contact initiation
R_e	radius of curvature at contact edge along actuator width

R_f radius of curvature of free membrane before contact

T axial stress resultant of pneu-net actuator cover

T_c turning moment

T_i stress resultant or line tension

t_m thickness of membrane

T_R resisting turning moment

U strain energy density function

u_0, v_0 displacement components of material line coordinates of beam

V volume displaced by the membrane

W work done on membrane by air pressure

x_e eccentricity of center of mass of cylindrical object in horizontal posture along actuator width

X_{L_i} length of beam segment

x_{t_i} position of beam segment from free end

y_c vertical tip offset for pneu-net actuator

Greek Symbols

α distance of any arbitrary point from contact center

β base angle of cone

δ midplane inflation of membrane

κ_i curvature

λ_i stretch

μ_f coefficient of friction

μ material shear modulus

ρ^* undeformed location of contact initiation point C_p

ρ_1 undeformed location of interior contact edge

ρ_2 undeformed location of exterior contact edge

θ rotation angle of deformed plane of beam

θ_c angle of contact for cylindrical substrate

θ_i slope of free membrane at clamp edge at contact initiation

θ_{m_1} deformed membrane interior angle

θ_{m_2} deformed membrane exterior angle

θ_{m_a} arc angle of deformed membrane along actuator width for section across contact midplane

θ_{m_c} angle subtended by interior arc at contact initiation

θ_{m_e} arc angle of deformed membrane along actuator width for section across contact edge

θ_{m_f} slope of free membrane at clamp edge before contact

θ_{m_s} slope at interior clamp edge

θ_m arc or clamp angle of deformed membrane surface

θ_s substrate inclination angle or half of the inclination angle between adjacent air chambers

Subscripts

i subscript index

Chapter 1

Introduction

1.1 Pneumatic Soft Robots

Soft robots are compliant structures. The compliance is provided either by the integration of a few soft parts in the structure or the structure is made entirely of soft materials, usually elastomers. The operating principle of these robots is their large deformation behavior. The field of soft robotics is evolving in multiple directions, such as fabrication process, actuation mechanism, sensory feedback, and application specific designs. The applications of soft robots are endless, ranging from collaborative robots to space exploration [1]. Soft robots are often categorized on the basis of their actuation mechanisms [2]. Fluid-driven soft actuators (also referred as fluidic elastomer actuators) are mainly operated by the pressure differential of working or driving fluid. Pneumatic soft actuators is one category of such actuators that uses air pressure as the power source. Pneumatic soft actuators are among the oldest and most widespread actuation technologies for soft robots. These actuators are popular because of their compliance inheritance, robustness, easy fabrication, and low cost elastomer materials [3]. The deformation or working operation of such actuators is usually governed by their geometric structure and fabrication material [4].

1.2 Pneumatic Soft Grippers

Soft actuators have the potential to serve as a versatile gripper for grasping variety of objects with moderate precision. These actuators have the ability to address challenges of soft body interactions, especially during handling soft objects [5]. Such interactions are generally encountered while handling products in food and agriculture industries [6–8], living creatures during oceanographic exploration [9, 10], and in healthcare applications [11].

The early soft grippers as presented by Suzumori *et al.* [12] were also developed using pneumatic soft actuators. Fluidic elastomer actuators were also used to develop an anthropomorphic hand that was capable of dexterous grasping [13]. Pneumatic soft grippers made of elastomers have recently gained extensive attention among researchers because of their low fabrication cost, maintenance cost, and wide application domain [2]. There are numerous architectures for pneumatic soft actuators, such as bellows-like structures, elongated elastomeric chambers with the addition of reinforcing fibers and layers, and tube-like tentacles [3]. These actuators can generate high forces due to the large strain behavior of fabricating material. The forces are proportional to fluid pressure and the surface area where active pressure is applied. The reaction time of pneumatically powered bending actuators is quite low, ranging from ≈0.05 to 1.0 s [14]. Casting or molding process is generally followed for the fabrication of these actuators. The molding process deals with the material in liquid form, and offers the flexibility of incorporating functional elements in the actuator such as inextensible layers [15], strain sensors [6, 16, 17], fibers [18, 19], variable stiffness elements [20, 21], origamis, porous materials [22, 23], and adhesion [24]. Recent advancement in 3D printing technology also enables the fabrication of these actuators as a single entity. Researchers demonstrated rapid fabrication of pneumatic soft grippers through printing. A hand made of pneumatic pouch motors and a flexible structure can be printed in 15 min [25]. MacCurdy *et al.* [26] developed a two-finger gripper by inkjet printing of a soft elastomer. A 3D printed gripper can handle different types of food filled in paper containers [7, 27]. Patel *et al.* [28] and Thrasher *et al.* [29] demonstrated 3-finger grippers made of UV curable elastomers that are 3D printed via digital light processing.

These grippers are best suited for grasping objects with highly irregular geometry, fragile properties, and objects in an unknown environment [5]. When actuated, elastomeric soft actuators deform in a designed geometric shape [4]. However, the design of these actuators is challenging because of their large deformation behavior. Many of these grippers have membrane-based design [14, 30–34]. Membrane-based structures generate large deformations even at low actuation pressure and thus well suited for such actuators. Choi *et al.* [35] conducted a study on the design and feasibility of a flexible gripper made of inflatable rubber pockets. Wang *et al.* [31, 36] presented circular and parallel shell grippers for handling food products. A membrane-based needle gripper for grasping and piercing food materials was presented in [37]. Based on soft membrane, a bistable valve for the autonomous control of a soft actuator was presented in [38]. A soft-bubble gripper for robust and perceptive manipulation was presented in [39]. Membrane-based jamming and self-sealing grippers were presented in [40, 41].

Recently, pneu-net soft actuators have gained significant attention owing to their fast actuation in bending [14, 42]. These actuators have numerous applications [43–45]. Low *et al.* [46] used two fingers to manipulate a surgical wire. Galloway *et al.* [9] showed the manipulation of delicate deep reefs and Zhou *et al.* [47] reported picking up of various food items, such as a banana, a pear, a piece of tofu, and an egg. Manipulation of objects in an amphibious environment was demonstrated by Hao *et al* [48].

To improve the design and performance of these actuators, various approaches have been presented [1, 49–55]. Researchers have integrated functional elements in their structure, exploiting the versatility offered by the molding process. Curvature sensing was implemented using resistive strain sensors made of stretchable or flexible electrodes [56], stretchable optical waveguides [16], as well as force sensing using a piezoresistive fabric component [57]. The integration of variable stiffness elements can offer increased holding weight. The proposed solutions include particle jamming [20], shape memory polymers [58], thermoplastic ligaments [59], and low melting point alloys [60]. Hao *et al.* [61] manually added a nylon wire around the fingers of the gripper to change their functional length and handle objects of different sizes, such as a screw, a pen, a chain of keys, and a cactus.

Recently, materials that are highly unconventional for robotics have been used for soft grippers. Yuk *et al.* [62] developed hydraulic hydrogel actuators and robots that are optically and sonically camouflaged in water. Walker *et al.* [63] developed an environmentally safe device using a biodegradable elastomer, i.e., poly(glycerol sebacate) with calcium carbonate. Shintake *et al.* [44] developed an edible gripper using a gelatin–glycerol material. Terryn *et al.* [64] developed self-healing soft pneumatic gripper using thermo-reversible Diels–Alder polymers.

1.3 Modeling of Soft Robots

The operating principle of soft robots is their controlled large deformation. To design and manufacture soft actuators, accurately and efficiently, their physics needs to be explored [65]. For the efficient design of these actuators, accurate models are needed to examine their deformation behavior [5]. To understand the deformation behavior, the modeling of these actuators, which involves both geometric and material nonlinearities, has attracted significant attention [66–72]. The existing models of pneumatic soft actuators are Euler–Bernoulli beam-based constant curvature [73–77], piecewise constant curvature [78, 79], Cosserat rod approach [80], lumped parameter [81], and finite element (FE) models [48, 82, 83]. FE-based simulations are widely used for the structural optimization of these actuators [84–88].

Coevoet *et al.* [86] presented a FE-based unified software framework for the modeling, simulation, and control of soft robots.

Additionally, analytical models for soft actuators have been developed [70, 72, 83, 89]. Polygerinos *et al.* [83] presented a quasi-static analytical and FE model for a fiber-reinforced actuator. Sadati *et al.* [79] presented geometric deformation-based constant and variable curvature models for a braided continuum manipulator. Paoletti *et al.* [70] presented an analytical model of a soft actuator to grasp soft and stiff objects. A recent study by Casanovas *et al.* [72] discussed a general approach for analytical modeling and design of soft extending and contracting devices. Connolly *et al.* [71] presented an analytical model of a soft actuator for trajectory tracking.

To model membrane-based actuators, both infinitesimal and finite-strain membrane models from the literature on finite elasticity and continuum mechanics can be adopted. To model a pneumatically driven membrane with clamped edge conditions, various finite-strain-based modeling approaches have been presented [90, 91]. Finite-strain models for membrane-based soft actuators were presented in [30, 92].

Analytical models of pneu-net actuators were presented in [30, 92–96]. Alici *et al.* [74] and Zhong *et al.* [77] presented Euler–Bernoulli beam-based models for a pneu-net actuator. Cao *et al.* [94] developed a constant-curvature model of a pneu-net actuator for model-based control of the actuator. Based on the constant curvature assumption, Liu *et al.* [92] calculated the bending angle and the tip forces of a pneu-net actuator by considering the deformation of air chambers. Based on the principles of elasticity and friction, Majidi *et al.* [93] presented an analytical model for a locomotion soft robot. Wang *et al.* [30] presented an analytical model of a pneu-net actuator based on the deformation of air chambers and serial robot assumption. Fang *et al.* [95] presented a geometry-based framework for computing the deformation of a pneu-net actuator within the range of linear elasticity. Xu *et al.* [96] developed a mathematical model of a pneu-net actuator based on the multiple point contact approach for contact between air chambers. Based on Euler's elastica theory, Payrebrune *et al.* [97] presented a rod-based model for pneu-net actuator. Gu *et al.* [98] presented a rod theory-based analytical model for a pneu-net actuator with oblique chambers. Wang *et al.* [99] presented a simplified line-segment model for a pneu-net actuator using an optimization-based parameter identification method. Zhou *et al.* [100] presented an analytical model for a pneumatic soft actuator made of symmetrical chambers that was part of a bionic robotic fish.

Table 1.1 Survey on Existing Models of Pneu-net Actuator [© 2022 IEEE]

Model	Cover Modeling	Chamber Modeling	Material Model	Output
Alici *et al.* [74]	Euler–Bernoulli beam-based constant curvature	—	Linear	Deformation, Force
Zhong *et al.* [77]	Euler–Bernoulli beam-based constant curvature	—	Linear	Deformation
Cao *et al.* [94]	Euler–Bernoulli beam-based constant curvature	—	Linear	Deformation
Liu *et al.* [92]	Serially connected constant curvature	Membrane-based	neo-Hookean	Deformation, Force
Wang *et al.* [30]	Serial robot	Surface-based	Yeoh	Deformation, Force, Dynamics
Fang *et al.* [95]	Fitting geometric profile	Fitting geometric profile	Linear	Deformation
Xu *et al.* [96]	Finite element-based approach	Finite element-based approach	Yeoh	Deformation
Payrebrune *et al.*[97]	Rod theory	—	Linear	Deformation, Force
Gu *et al.* [98]	Rod theory	—	Linear, Multi-material	3D-deformation, Force
Wang *et al.* [99]	Optimization-based parameter identification method	—	Linear	Deformation, Force, Dynamics

1.4 Aim of Present Work

The analytical modeling of soft actuators is in its developmental phase and is still not sufficiently mature. Despite the aforementioned developments, well-understood analytical models of these actuators are yet to be developed because their intrinsic deformation is continuous, complex, and highly compliant. The behavior of these structures is complex due to the presence of geometric and material nonlinearities, and hence, is difficult to capture accurately using infinitesimal-strain theories. This study is focused on the development of analytical and computationally less expensive model for pneumatic soft actuators. In this work, we focused on analytical modeling of two actuators: 1) flat shell actuator; and 2) pneu-net actuator. The photo snapshots of these actuators are shown in Fig. 1.1.

The flat shell gripper is primarily developed to grasp agriculture products, such as cucumbers. The design of this actuator is relatively simple and is basically a replica of one of the standard geometric structures, i.e., a flat rectangular membrane. Various approaches to model the behavior of a flat shell membrane are reported in literature, but the contact interaction of the membrane is not well investigated yet. The flat shell actuator model is based on the finite-strain membrane theory. The contact interaction of the actuator with flat and cylindrical substrates is investigated [101].

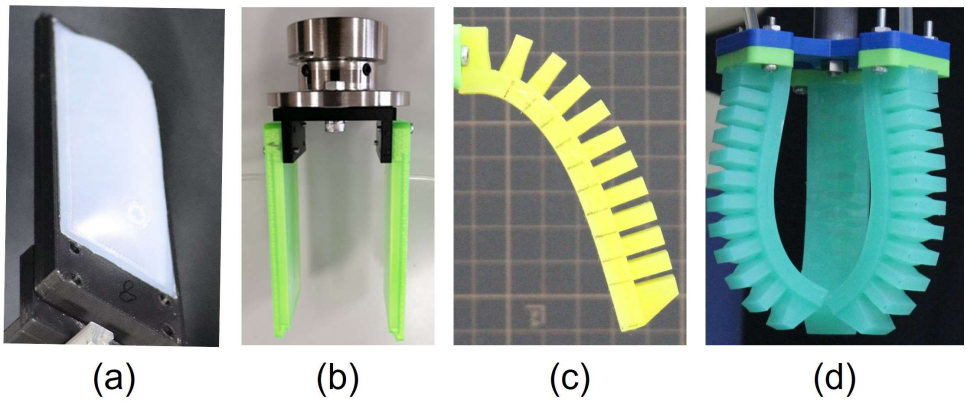

Fig. 1.1 Snapshots of pneumatic soft actuators. (a) Flat shell actuator, (b) two-finger flat shell gripper, (c) pneu-net actuator, and (d) three-finger pneu-net gripper.

A brief analysis of the features of existing analytical models of pneu-net actuators is presented in Table 1.1. From the analysis, as an outcome, the modeling of air chambers is not much explored. Most pneu-net actuator analytical models considered the free-space deformation but did not account for external contact. The actuators contain many passive degrees of freedom, and when driven at a low input pressure, the available pneumatic power cannot compensate for gravity loading [67]. FE-based simulations have been widely used to

model and simulate the behavior of a pneu-net actuator and they work well for reproducing the deformation and stress of the actuator. However, for real time applications or applications requiring fast calculations, computationally efficient models are required. Therefore, it is necessary to develop methods to account for these factors. The pneu-net actuator model is based on finite-strain membrane and Euler–Bernoulli beam theories [102]. The air chambers of the pneu-net actuator are modeled using membrane theory, and the actuator cover is modeled using beam theory. The incompressible neo-Hookean material model is considered to account for the hyperelastic behavior of actuator material.

1.5 Dissertation Organization

In Chapter 2, a brief introduction to the membrane and beam theories is presented. These theories are part of existing literature on elasticity and continuum mechanics. We followed these theories to formulate analytical models of the actuators.

In Chapter 3, modeling approach for the flat shell gripper is discussed. The models are developed for four different states of the actuator: 1) free-space; 2) contact with flat substrate; 3) contact with cylindrical substrate; and 4) grasping cylindrical objects. The analytical models consist of nonlinear algebraic equations as the final governing equations.

In Chapter 4, modeling approach for the pneu-net actuator is discussed. The models are developed for two different states of the actuator: 1) free-space; and 2) grasping state. The models consist of nonlinear algebraic and differential equations as the final governing equations.

In Chapter 5, numerical solution procedure for the formulated equations and applications of the presented modeling approaches are discussed.

In Chapter 6, experimental validation of the developed models is presented. Different sets of experiments were performed to test the validity of developed models. Experiments were also conducted to extract mechanical properties of the actuators.

Chapter 7 concludes the dissertation and suggested applications and future perspective of the presented work.

Chapter 2

Theoretical Background

A brief introduction to the membrane and beam theories followed for the modeling of soft actuators is discussed in this chapter. The membrane theory is followed for modeling the inflatable part of the actuators, and the beam theory is followed for modeling the pneu-net actuator. The analytical results presented here are based on existing literature.

2.1 Infinitesimal-Strain Membrane Theory

The analytical analysis for small deflections of membranes having different contours was presented by Storakers [103]. The midplane extension of a rectangular membrane subjected to lateral pressure as derived by Storakers has the following form

$$p = \frac{CEt_m\delta^3}{a^4} \tag{2.1}$$

where p is pressure applied on the membrane, E is modulus of elasticity of membrane material, t_m is membrane thickness, δ is membrane midplane extension, $2a$ is membrane width or smaller dimension, and C is a constant that depends on the Poisson's ratio and major dimensions of the membrane.

The infinitesimal-strain membrane model is followed for the modeling of pneu-net actuator air chambers.

2.2 Finite-Strain Membrane Theory

The analytical analysis for finite deformation of thin membranes was presented in [90, 104]. For an isotropic and incompressible membrane, the principal stretches can be defined as

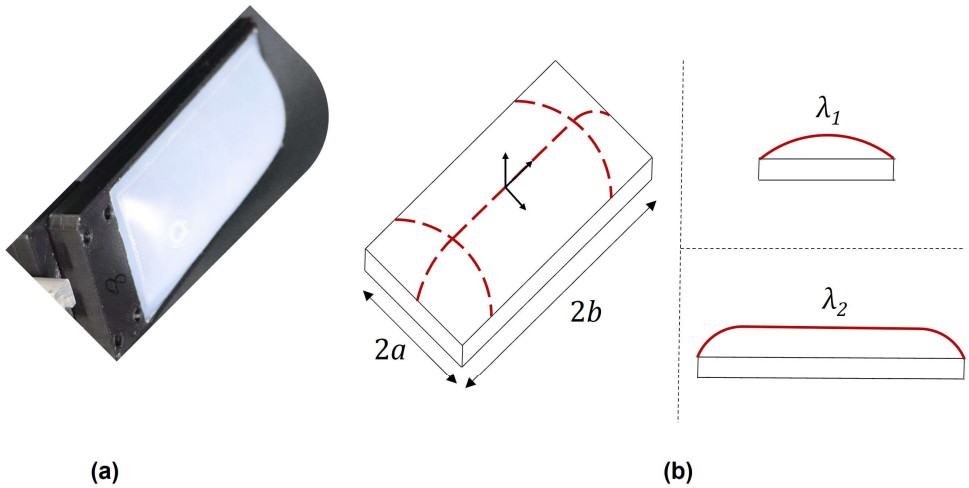

Fig. 2.1 (a) Flat shell actuator prototype. (b) Schematic of free-space deformation of flat shell actuator (rectangular membrane). λ_1 and λ_2 are stretches defined along membrane width and length, respectively.

λ_1, λ_2, and $\lambda_3 = (\lambda_1\lambda_2)^{-1}$ (see Fig. 2.1). For hyperelastic membranes [90, 104], the stress resultants or line tensions T_i in principal directions are defined as

$$\begin{aligned} T_1 &= 2\, t_m\, \lambda_3 \left({\lambda_1}^2 - {\lambda_3}^2\right)\left(U_1 + {\lambda_2}^2\, U_2\right) \\ T_2 &= 2\, t_m\, \lambda_3 \left({\lambda_2}^2 - {\lambda_3}^2\right)\left(U_1 + {\lambda_1}^2\, U_2\right) \end{aligned} \tag{2.2}$$

where U is strain energy density function and U_i denotes $\dfrac{\partial U}{\partial I_i}$. The strain energy density $U(I_1, I_2)$ is a function of strain invariants I_1 and I_2. The strain invariants are defined as

$$I_1 = {\lambda_1}^2 + {\lambda_2}^2 + {\lambda_3}^2 \;\; ; \;\text{and}\;\; I_2 = \lambda_1^{-2} + \lambda_2^{-2} + \lambda_3^{-2}\,. \tag{2.3}$$

The equilibrium equation for the membrane is defined as [104]

$$\kappa_1 T_1 + \kappa_2 T_2 = p \tag{2.4}$$

where κ_i is the principal curvature. The strain energy density function U for a neo-Hookean material [105] is defined by

$$U = \frac{\mu}{2}\,(I_1 - 3) \tag{2.5}$$

where μ is shear modulus. After substituting (2.5) into (2.2), the line tensions become

$$T_1 = \mu\ t_m\ \lambda_3 \left({\lambda_1}^2 - {\lambda_3}^2\right)$$
$$T_2 = \mu\ t_m\ \lambda_3 \left({\lambda_2}^2 - {\lambda_3}^2\right). \tag{2.6}$$

Next, based on the deformed geometry, we defined stretches λ_i and curvatures κ_i for each actuator, separately. The finite-strain membrane model is followed for the modeling of flat shell gripper and for the air chambers of pneu-net actuator.

2.3 Finite-Strain Beam Theory

The analytical analysis of plane-strain hyperelastic thin beams with thickness stretching effect was presented by He *et al.* [106]. A schematic of deformed and undeformed geometries of a thin beam is shown in Fig. 2.2. The rotation angle θ and stretch λ are defined as

$$\theta = \arctan \frac{v_0'}{1+u_0'} \tag{2.7}$$
$$\lambda = \sqrt{(1+u_0')^2 + {v_0'}^2} \tag{2.8}$$

where $u_0,\ v_0$ are displacement components of the material line and $(.)'$ represents the derivative with respect to coordinate X. The curvature κ of the deformed midplane of the beam is defined as

$$\kappa = \frac{d\theta}{ds} = \frac{d\theta}{\lambda dX} = \frac{\theta'}{\lambda} \tag{2.9}$$

where ds is the deformed length of line element dX that lies on the geometric midplane. The beam is made of incompressible neo-Hookean material.

He *et al.* [106] developed the following Euler–Lagrange equations for hyperelastic beams

$$\left(T\cos\theta + \frac{M'+m}{\lambda}\sin\theta\right)' + g_x = 0 \tag{2.10}$$
$$\left(T\sin\theta - \frac{M'+m}{\lambda}\cos\theta\right)' + g_y = 0 \tag{2.11}$$

where T is axial stress resultant, M is bending moment, m is distributed bending moment per unit length, and $g_x,\ g_y$ are distributed forces per unit length acting along X and Y-directions,

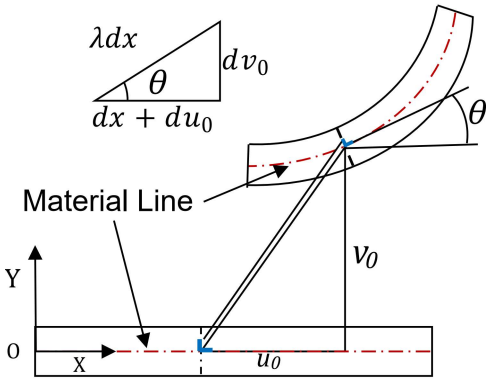

Fig. 2.2 Geometry of deformed and undeformed configurations of a plain-strain hyperelastic beam [© 2022 IEEE].

respectively. The axial stress resultant T and bending moment M are defined as

$$\frac{T}{\mu BH} = \lambda - \frac{1}{\lambda^3} - \frac{\kappa^2 H^2}{\lambda^7} \tag{2.12}$$

$$\frac{M}{\mu BH^3} = \frac{\kappa}{3\lambda^6} \, . \tag{2.13}$$

The boundary conditions associated with these equations are derived as

$$\begin{aligned} &P = P_X \text{ or } \delta u_0 = 0, \text{ at } X = 0 \text{ and } X = L \\ &Q = Q_X \text{ or } \delta v_0 = 0, \text{ at } X = 0 \text{ and } X = L \\ &M = M_X \text{ or } \delta \theta_0 = 0, \text{ at } X = 0 \text{ and } X = L \end{aligned} \tag{2.14}$$

where P, Q are components of stress resultant vector along X and Y-directions, respectively. The components are defined as

$$P = T\cos\theta + \frac{M' + m}{\lambda}\sin\theta \tag{2.15}$$

$$Q = T\sin\theta - \frac{M' + m}{\lambda}\cos\theta \, . \tag{2.16}$$

The finite-strain beam model was followed for modeling the pneu-net actuator cover. We reformulated these equations to capture the deformation of the actuator and developed the governing equations for its different states.

Chapter 3

Analytical Modeling of Flat Shell Gripper

Pneumatic soft actuators are usually designed to attain a predefined geometry upon actuation. The deformed geometry attained by the flat shell gripper is one of the fundamental geometries, i.e., inflation of a rectangular membrane. In this chapter, the formulation of governing equations for the membrane part of flat shell gripper is presented. The flow of modeling is presented in Fig. 3.1.

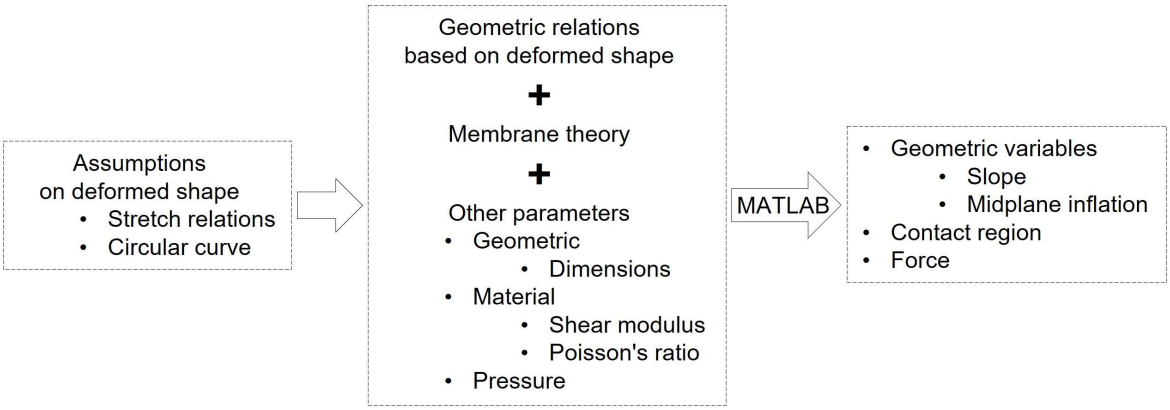

Fig. 3.1 Flow of modeling for the flat shell actuator made of rectangular membrane.

3.1 Actuator Design

The actuator comprised a rigid shell and a soft thin membrane. The rigid shell (see Fig. 3.2), which is typically fabricated using a 3D printer with PLA or PETG materials, serves not only the mold for casting the thin membrane, but also as a component of the actuator for providing support to the membrane. The fabrication method is relatively simple and it requires only a one-time casting procedure that does not involve demolding. The detailed design and

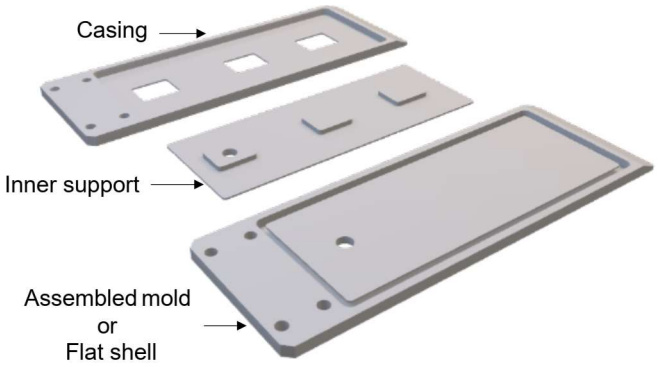

Fig. 3.2 Rigid shell or mold for the flat shell gripper. The mold is comprised of an outer casing and an inner support.

fabrication of a similar actuator was presented in [36]. The actuator is pneumatically driven and can generate a relatively large force because of the rigid shell. To reduce modeling

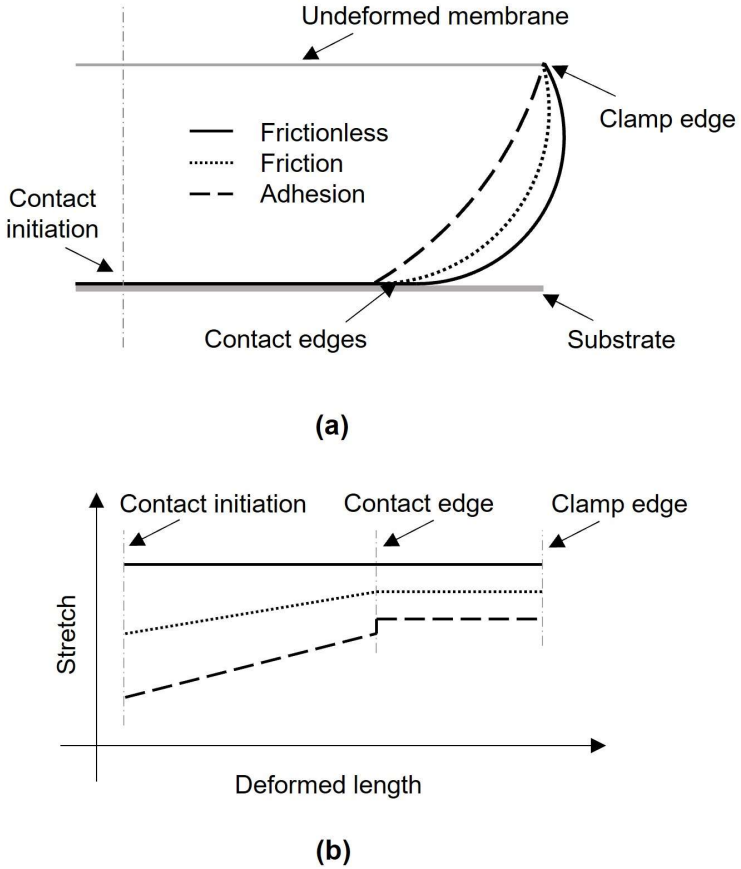

Fig. 3.3 (a) Schematic of deformed membrane profile in contact with a flat substrate in friction-less, friction, and adhesion modes. (b) The variation of stretch along deformed membrane profile in different contact modes.

complexity, certain assumptions were made on the design and behavior of the actuator. The actuator is assumed to be a rectangular membrane with clamped end condition. The pressure is assumed to be uniformly distributed on the membrane surface and at the contact region. The deformed profile of the membrane is considered continuous and smooth. The free portion of deformed membrane is assumed to follow a circular shape. The contact between membrane and substrate is assumed to be friction-less [see Fig. 3.3(a)], and the stretch variation along the deformed curve is assumed to be uniform [see Fig. 3.3(b)]. In Fig. 3.3, the contact is initiated at the middle of membrane and due to symmetry, only one half is shown. Here, the contact edges are shown at an identical location for all contact modes. This is shown only for better comparative analysis of stretch variation. However, physically the contact edges do not lie at the same location. Also, the slope of stretch curves for friction and adhesion cases are not related with other. The slopes are arbitrary.

The formulation of governing equations for free-space deformation of the actuator is presented in the next section.

3.2 Free-Space Deformation

For a rectangular membrane, the change in dimensions along the principal directions is assumed to be $\Delta a = \Delta b$ [see Fig. 3.4(a)]. Using this assumption, the principal stretches λ_1

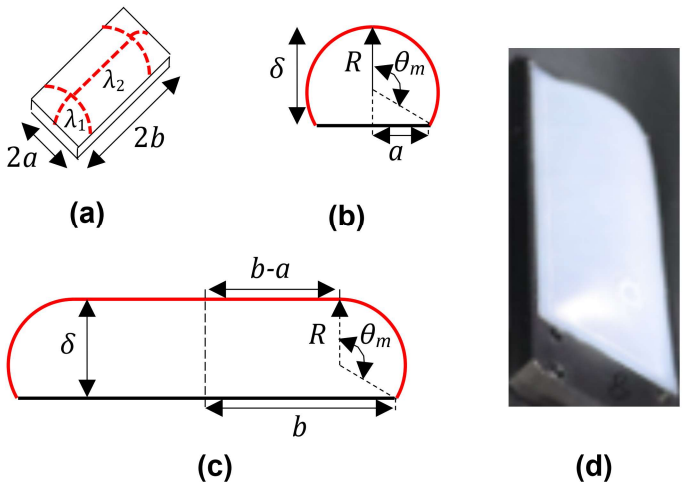

Fig. 3.4 Schematic illustration of free deformation of a rectangular membrane. (a) Isometric view, (b) section view along actuator width, (c) section view along actuator length, and (d) experimental snapshot of inflated actuator [© 2022 IEEE].

and λ_2 can be expressed as

$$\lambda_1 = \lambda \quad ; \text{ and } \quad \lambda_2 = 1 + \frac{a}{b}(\lambda - 1) \, . \tag{3.1}$$

The membrane material is assumed to be isotropic and incompressible. For an incompressible material, the principal stretch λ_3 can then be written as

$$\lambda_3 = (\lambda_1 \, \lambda_2)^{-1} \, . \tag{3.2}$$

The deformed profile along actuator width is assumed to exhibit a circular shape with curvature $\kappa_1 = \dfrac{1}{R}$ [see Fig. 3.4(b)]. The average curvature [107] along actuator length can be written as [due to symmetry, only one-half is considered; see Fig. 3.4(c)]

$$\kappa_2 = \frac{\theta_m}{R \, \theta_m + (b-a)} \tag{3.3}$$

where θ_m is arc or clamp angle of deformed membrane surface. Based on deformed geometry of the membrane, we can express the radius of curvature R as

$$R = \frac{a}{\sin \theta_m} \, . \tag{3.4}$$

From deformed geometry, the stretch λ_1 along actuator width can be written as

$$\lambda_1 = \frac{\theta_m}{\sin \theta_m} \, . \tag{3.5}$$

The maximum inflation δ of the membrane is derived from the deformed geometry as

$$\delta = a \tan \left(\frac{\theta_m}{2} \right) . \tag{3.6}$$

After substituting the curvatures into membrane equilibrium equation (2.4), it can be written as

$$\frac{1}{R} \, T_1 + \frac{\theta_m}{R \, \theta_m + (b-a)} \, T_2 = p \, . \tag{3.7}$$

Equation (3.7) is the final governing equation for free-space deformation of the membrane. After substituting (2.6), (3.1), (3.2), (3.4), and (3.5) into (3.7), it reduced to a nonlinear algebraic equation, having θ_m as the only variable.

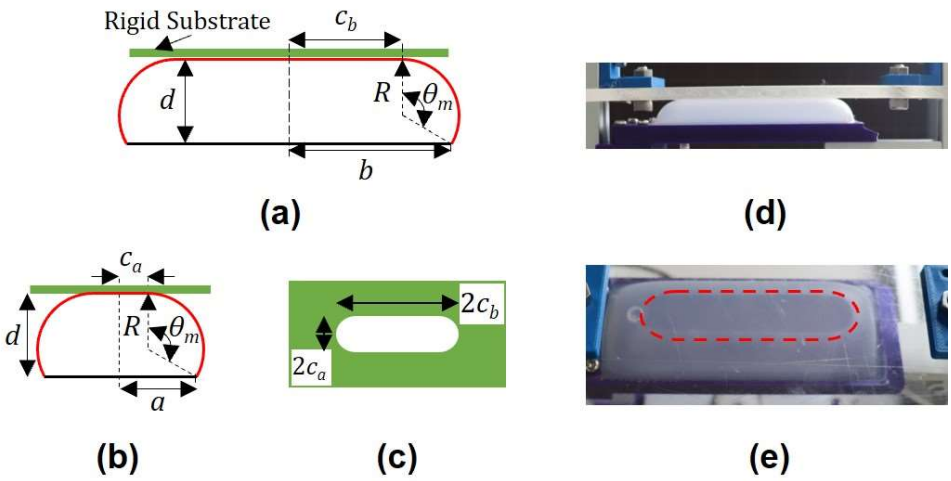

Fig. 3.5 Schematic illustration of a rectangular membrane in contact with a flat rigid substrate. (a) Section view along actuator length, (b) section view along actuator width, (c) assumed shape of contact region, (d) experimental setup to determine actual shape of contact region, and (e) actual contact region. In (e), the dotted red curve represents an oval shape [© 2022 IEEE].

3.3 Full Contact with Flat Substrate

The formulation of governing equations for predicting the contact force and deformed geometry of the actuator in full contact with a parallel flat substrate is presented in this section. From the deformed geometry [see Fig. 3.5(a)], the radius of curvature R can be written as

$$R = \frac{d}{1-\cos\theta_m} \tag{3.8}$$

where d is the offset between membrane and substrate. The contact width c_a along actuator width [see Fig. 3.5(b)] can be written as

$$c_a = a - d\cot\left(\frac{\theta_m}{2}\right). \tag{3.9}$$

The contact width c_b along actuator length can be expressed in terms of c_a as

$$c_b = \lambda_2\, b - \lambda_1\, a + c_a\,. \tag{3.10}$$

The stretch λ_1 along actuator width can be expressed as

$$\lambda_1 = 1 + \frac{d}{a}\left[\frac{\theta_m}{2}\csc^2\left(\frac{\theta_m}{2}\right) - \cot\left(\frac{\theta_m}{2}\right)\right]. \tag{3.11}$$

After substituting (2.6), (3.1), (3.2), (3.8), and (3.11) into equilibrium equation (3.7), it gets reduced to a nonlinear algebraic equation, having θ_m as the only variable. The contact region exhibits an oval shape, as validated experimentally in Fig. 3.5(d) and (e). The contact area A_c for an oval-shaped region [see Fig. 3.5(c)] can then be calculated as

$$A_c = 2c_a\,(2c_b - 2c_a) + \pi\ {c_a}^2\ . \tag{3.12}$$

The normal contact force F_c can be calculated as

$$F_c = p\,A_c\ . \tag{3.13}$$

3.4 Contact with Cylindrical Substrate

In this section, we formulate the model of membrane actuator in contact with a cylindrical substrate for applications in grasping agricultural products, such as cucumbers [36]. Here, we consider the axis of substrate to be parallel to the width of actuator, as shown in Fig. 3.6.

3.4.1 Contact Along Actuator Length

Based on deformed geometry of the membrane [see Fig. 3.6(a)], stretch λ_2 can be expressed as (due to symmetry, only one-half is considered)

$$\lambda_2 = \frac{r\ \theta_c + R\ \theta_c + e + R\ \theta_m}{b} \tag{3.14}$$

where θ_c is contact angle and e is portion of deformed membrane with zero curvature. The undeformed length b can be expressed as

$$b = r\sin\theta_c + R\sin\theta_c + e + R\sin\theta_m\ . \tag{3.15}$$

The object offset d can be expressed as

$$d = r\cos\theta_c + R\cos\theta_c - R\cos\theta_m\ . \tag{3.16}$$

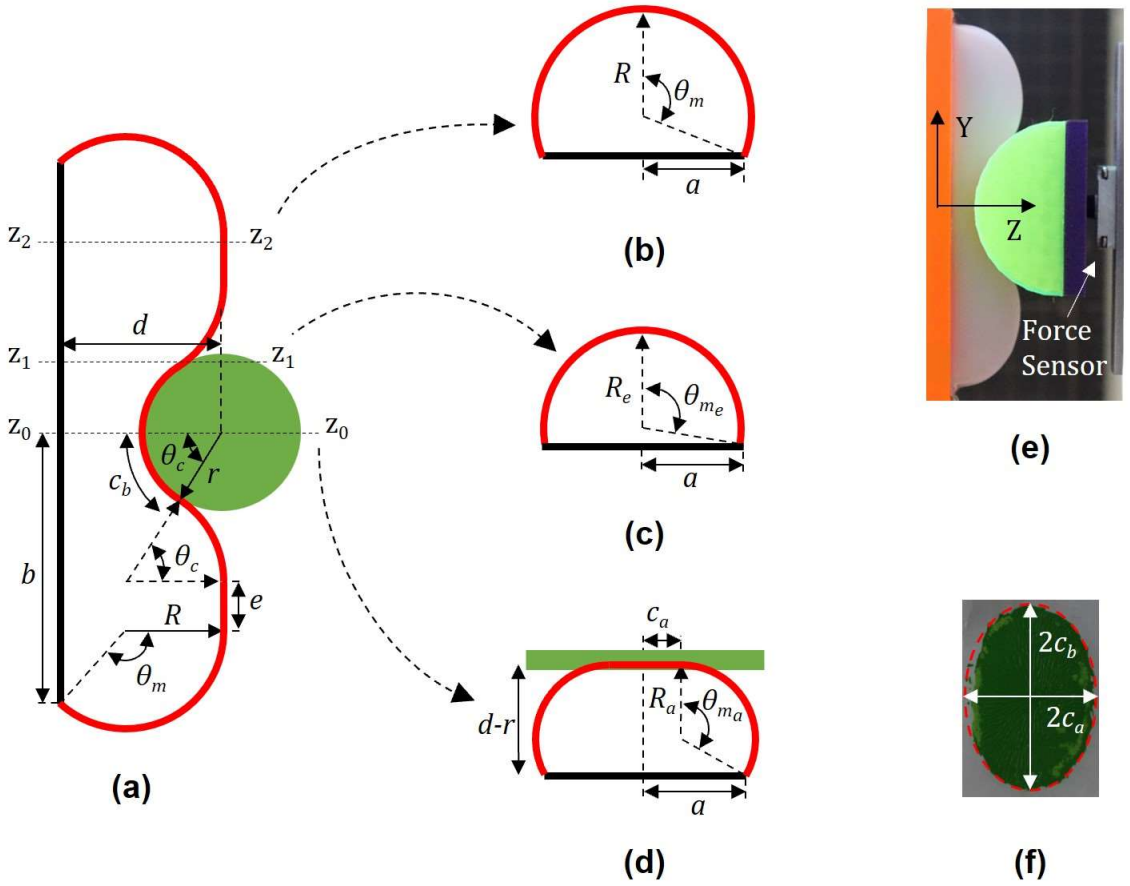

Fig. 3.6 Schematic illustration of a rectangular membrane in contact with a rigid cylindrical substrate. (a) Section view of contact along actuator length, (b) free deformation along actuator width (section z_2-z_2), (c) deformation at contact edge (section z_1-z_1), (d) contact at the mid-plane (section z_0-z_0), (e) photo snapshot of experimental setup for force measurement, and (f) experimentally validated assumed shape of elliptical contact region [© 2022 IEEE].

The contact width c_b along actuator length can be written as

$$c_b = r\,\theta_c\ . \tag{3.17}$$

3.4.2 Contact Along Actuator Width

The deformed profile of the membrane is assumed to be spherical at the ends [see Fig. 3.4(a)]. From the deformed geometry for section z_2-z_2, as shown in Fig. 3.6(b), the undeformed width a can be expressed as

$$a = R\sin\theta_m\ . \tag{3.18}$$

The stretch λ_1 along actuator width can be expressed as

$$\lambda_1 \; a = R \; \theta_m \; . \tag{3.19}$$

From the deformed geometry for section z_0-z_0 as shown in Fig. 3.6(d), the object offset can be expressed as

$$d - r = R_a - R_a \cos \theta_{m_a} \tag{3.20}$$

where R_a is radius of curvature and θ_{m_a} is arc angle. The undeformed width a of the membrane can be expressed as

$$a = c_a + R_a \sin \theta_{m_a} \; . \tag{3.21}$$

Along actuator width, the stretch is assumed to be constant throughout the contact region, i.e., the stretch at section z_0-z_0 and z_1-z_1 are equal [see Fig. 3.6(c) and (d)]. From deformed geometry, the stretch λ_{1_0} at section z_1-z_1 can be calculated as

$$\lambda_{1_0} = \frac{\theta_{m_e}}{\sin \theta_{m_e}}. \tag{3.22}$$

The inflation height δ_e at contact edge (section z_1-z_1) can be calculated from the deformed geometry along actuator width as

$$\delta_e = R_e - R_e \cos \theta_{m_e} \; . \tag{3.23}$$

It can also be calculated from the deformed geometry along actuator length as

$$\delta_e = R \cos \theta_c - R \cos \theta_m \; . \tag{3.24}$$

The undeformed membrane width a can be expressed as

$$a = R_e \sin \theta_{m_e} \; . \tag{3.25}$$

The arc angle θ_{m_e} for section z_1-z_1 can be calculated from (3.23), (3.24), and (3.25) as

$$\theta_{m_e} = 2 \; \tan^{-1} \left[\frac{R \left(\cos \theta_c - \cos \theta_m \right)}{a} \right] . \tag{3.26}$$

The stretch λ_{1_0} can be expressed as

$$\lambda_{1_0}\, a = c_a + R_a\, \theta_{m_a}\ . \tag{3.27}$$

The contact region is assumed to be elliptical and is validated experimentally, as shown in Fig. 3.6(f). In this case, the contact area can be calculated as

$$A_c = \pi\, c_a\, c_b\ . \tag{3.28}$$

In force-measuring experiment (for force data see Section-6.2.3), the sensor recorded force data corresponding to the Z-direction, as shown in Fig. 3.6(e). The component F_z of the contact force along the Z-direction can be calculated by projecting the contact area normal to the Z-direction as

$$F_z = p\ \pi c_a\, r \sin\theta_c\ . \tag{3.29}$$

3.4.3 Curvature

Along actuator width, the stretch is maximum at section $z_2{-}z_2$. The curvature at this section is: $\kappa_1 = \dfrac{1}{R}$. The average curvature of free portion of the membrane along actuator length is defined as

$$\kappa_2 = \frac{\theta_m + \theta_c}{R\theta_c + e + R\theta_m}\ . \tag{3.30}$$

We now have sufficient number of equations for the number of unknown variables. Therefore, by solving (2.4), (3.15), (3.16), (3.18), and (3.27) as a set of nonlinear algebraic equations, we can obtain all the unknown variables.

3.4.4 Axial Offset State (offset along actuator length)

The vertical offset between the membrane and cylindrical object is defined by $b-h$, as shown in Fig. 3.7(a). Based on the assumed deformed profile of the membrane, a limit exists on h, below which the membrane cannot grasp the object. The restriction on h is imposed by parameter e_2. A successful grasp can only be achieved if $e_2 \geq 0$. For $e_2 < 0$, the object does not get a stable enclosure because the net resultant grasping force is in the downward direction [see Fig. 3.7(b) and (c)]. For $e_2 > 0$, the contact along actuator width remains the same as that for $b = h$. Here, the deformed profile along actuator length becomes asymmetric,

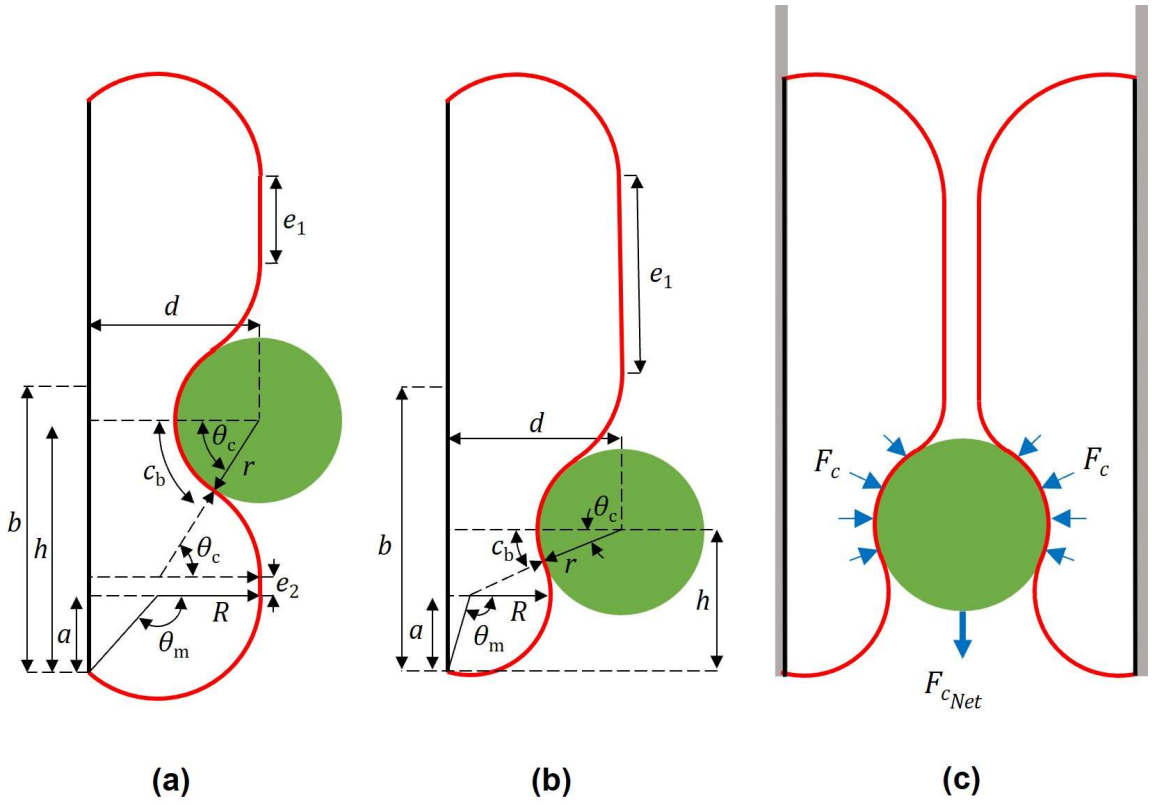

Fig. 3.7 Schematic illustration of a rectangular membrane in contact with a rigid cylindrical substrate. (a) Offset state ($e_2 > 0$), (b) offset state $h < (r+a)$ or $e_2 < 0$, and (c) a two-finger shell gripper [© 2022 IEEE].

as shown in Fig. 3.7(a). For this case, the stretch λ_2 can be defined as

$$\lambda_2 = \frac{2r\ \theta_c + 2R\ \theta_c + e_1 + 2R\ \theta_m + e_2}{2b}. \tag{3.31}$$

The undeformed length b can be expressed as

$$2b - h = r\sin\theta_c + R\sin\theta_c + e_1 + R\sin\theta_m\ . \tag{3.32}$$

The vertical offset h can be expressed as

$$h = r\sin\theta_c + R\sin\theta_c + e_2 + R\sin\theta_m\ . \tag{3.33}$$

The horizontal object offset d can be expressed as

$$d = r\cos\theta_c + R\cos\theta_c - R\cos\theta_m\ . \tag{3.34}$$

For such configurations, the contact along actuator width and the remaining equations are the same as those for $b = h$ (Section-3.4.2).

Offset Height h for Successful Grasp

The minimum value of offset height h for a successful grasp can be calculated corresponding to $e_2 = 0$. We can calculate h by substituting $e_2 = 0$ into (3.31) and (3.33) and then solving the system of nonlinear equations for h. Vertical offset is a critical parameter for achieving a grasp with the gripper.

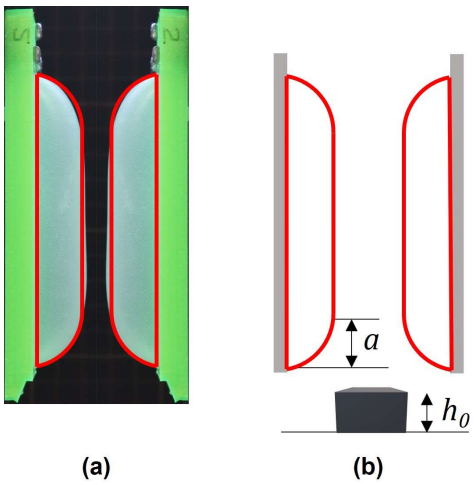

Fig. 3.8 Schematic of flat shell gripper showing grasp dependency on object size.

We can also define the grasping capabilities of flat shell actuator in terms of the minimum size of object that it can grasp. Based on deformed membrane profile, the minimum size of object that can be grasped by the gripper can be predicted using the smaller dimension a of the membrane. The actuator is assumed to have spherical deformed geometry at the ends [see Fig. 3.4(a) and (d)], and based on this assumption, it will not be able to grasp an object having height $h_0 \leq a$, as shown in Fig. 3.8. This kind of relationship between the deformed profile of actuator and the size of grasping object is usually absent in grippers made of rigid finger-tips but for membrane based grippers, it is important to consider this behavior.

3.4.5 Eccentric Grasp (offset along actuator width)

The objective of this section is to account the eccentricity of the center of mass of the cylindrical object, as shown in Fig. 3.9. Such conditions are encountered while grasping objects within a limited space. Physically, this condition was encountered while grasping multiple cucumbers using a gripper made of multiple flat shell actuators [36].

The center of mass of the cylinder is at a distance x_e from the center of the actuator. The eccentric mass applied a turning moment T_c at the contact region as

$$T_c = mg\, x_e \,. \tag{3.35}$$

The effect of turning moment T_c is counter acted by a resisting turning moment T_R , as shown in Fig. 3.9(c). The resisting turning moment T_R can be calculated from the contact region and traction force as

$$T_R = \int \alpha \, df \tag{3.36}$$

where α is the distance of any arbitrary point from the center and df is differential traction force element. The differential force element can be expressed in terms of pressure and area as

$$\begin{aligned} T_R &= \int \alpha \, df \\ &= \int \alpha \, \mu_f \, p \, dA \end{aligned} \tag{3.37}$$

where p is pressure, μ_f is coefficient of friction, and dA is differential area element. In Cartesian coordinates, the distance α can be written as

$$\alpha = \sqrt{x^2 + y^2} \,. \tag{3.38}$$

The area of elliptical contact region can be calculated by taking the integral over the boundary as

$$\begin{aligned} A &= 4 \int_0^{c_b} x \, dy \\ &= 4 \int_0^{c_b} \left[{c_a}^2 \left(1 - \frac{y^2}{{c_b}^2} \right) \right]^{\frac{1}{2}} dy \,. \end{aligned} \tag{3.39}$$

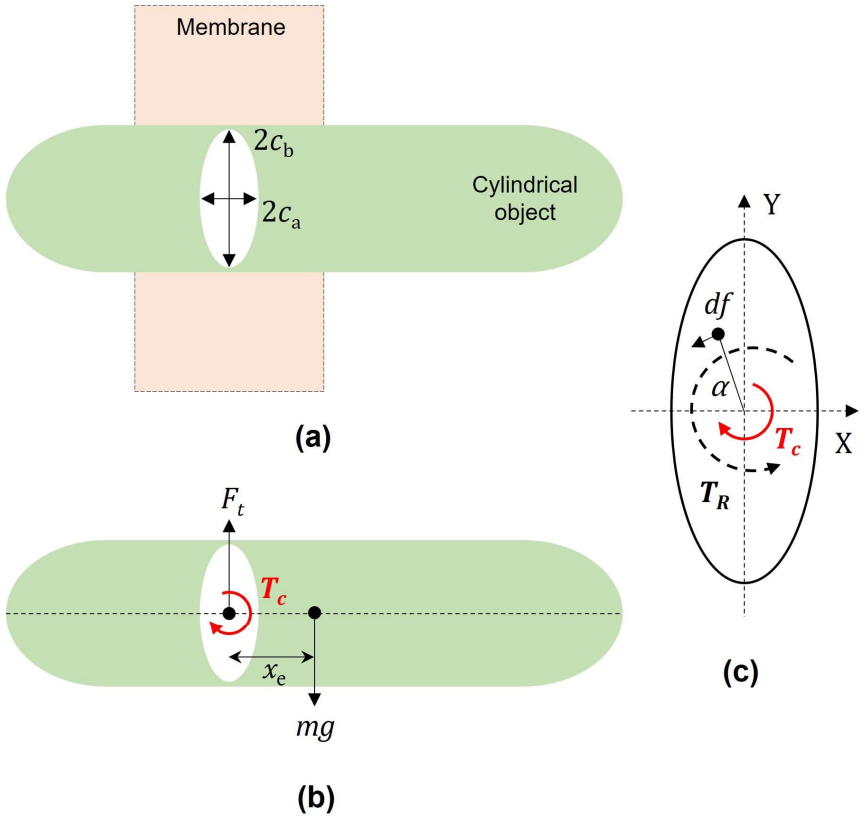

Fig. 3.9 Schematic of eccentric grasp of a cylindrical object. (a) Position of object with respect to actuator and shape of contact region, (b) free-body diagram, and (c) detailed free-body diagram. The center of mass is at a distance x_e from the center of contact region.

Substituting (3.38) and (3.39) into (3.37), we get the resisting turning moment as

$$T_R = 4\mu_f \, p \int_0^{c_b} \left[{c_a}^2 \left(1 - \frac{y^2}{{c_b}^2} \right) + y^2 \right]^{\frac{1}{2}} \left[{c_a}^2 \left(1 - \frac{y^2}{{c_b}^2} \right) \right]^{\frac{1}{2}} dy \, . \tag{3.40}$$

To resist the tilting effect, the resisting turning moment must be

$$T_c \leq T_R$$

$$\text{i.e.,} \quad mg \, x_e \leq 4\mu_f \, p \int_0^{c_b} \left[{c_a}^2 \left(1 - \frac{y^2}{{c_b}^2} \right) + y^2 \right]^{\frac{1}{2}} \left[{c_a}^2 \left(1 - \frac{y^2}{{c_b}^2} \right) \right]^{\frac{1}{2}} dy \, . \tag{3.41}$$

Physically, the contact force required to resist the tilting will be greater than the lifting force. We can calculate the pressure required to resist the tilting motion of the cylindrical object using (3.41).

Chapter 4

Analytical Modeling of Pneu-net Actuator

The desired deformation behavior of pneu-net actuator is bending motion, like human fingers. However, the actuator experiences both stretching and bending. Air chambers are the principal driving element of the actuator. An overview of the modeling approach for the pneu-net actuator is presented in Fig. 4.1. In order to capture the deformation behavior of the actuator, it is important for us to first understand the deformation behavior of air chambers.

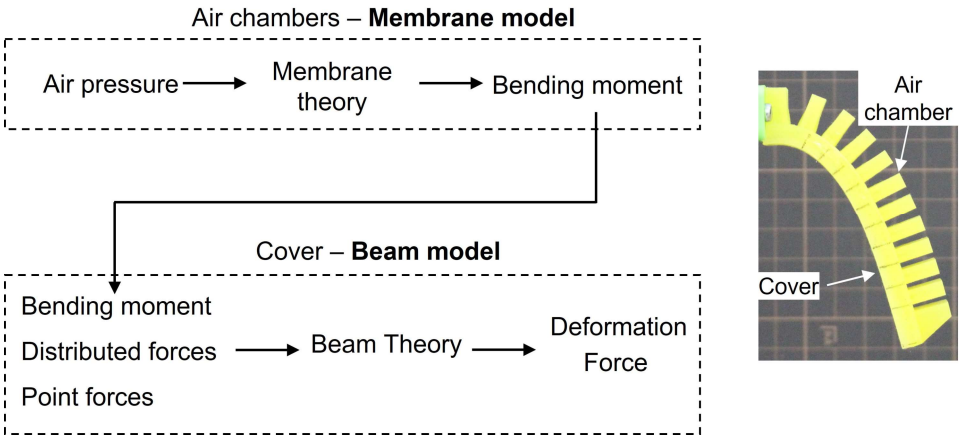

Fig. 4.1 Flow of modeling approach for pneu-net actuator.

4.1 Actuator Design and Theoretical Assumptions

The soft actuator design is based on the pneu-net morphology of elastomer robot. A detailed discussion on actuator design was presented in [108]. The casting process was employed to fabricate the actuator using silicone rubber. Certain assumptions were made while modeling the actuator. The pressure is assumed to be uniform throughout the actuator, and the friction

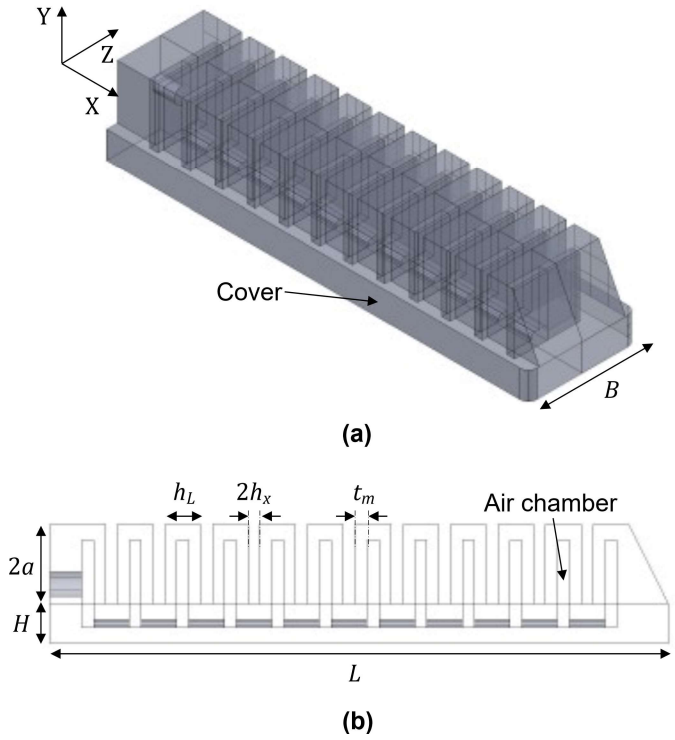

Fig. 4.2 Design of pneu-net actuator. (a) An isometric view and (b) section view along actuator length [© 2022 IEEE].

at the contact between adjacent chambers is not considered. As shown in Fig. 4.2, the cover pad at the base of actuator is modeled as a hyperelastic cantilever beam with a rectangular cross-section. The air chambers are modeled as independent elements that apply a distributed as well as an eccentric axial force on the cover. The distributed force is due to the weight of air chambers. The eccentric axial force is induced by the air pressure, and it is predicted using the deformation of the side walls of air chambers. The bending stiffness of the air chambers is not considered. The model assumes that the applied air pressure is adequate and all air chambers are in contact. The modeling approach considers only flat geometry chambers as the initial undeformed state.

4.2 Infinitesimal-Strain Air Chamber Model

The pneu-net soft actuator consists of several serially connected air chambers. In the geometric design of air chambers, the thickness of chamber walls facing the adjacent chambers (in YZ plane, see Fig. 4.2) is lower than that of the remaining walls. When inflated in free-space state, the actuator attains the deformed shape shown in Fig. 4.3(a). A schematic of adjacent chambers in contact is shown in Fig. 4.3(b). The eccentric axial force applied to the actuator

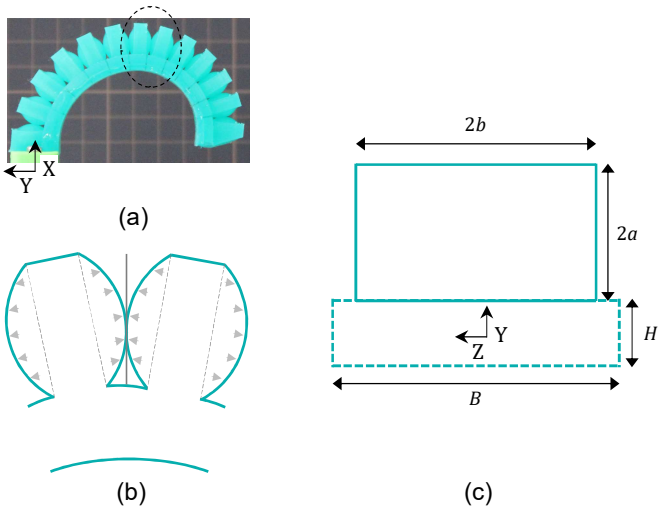

Fig. 4.3 Geometry of air chambers. (a) Snapshot of a soft pneu-net actuator subjected to air pressure in free-space deformation state, (b) enlarged sketch of deformed air chambers, and (c) section view of air chamber along YZ plane, representing undeformed side wall. In (c) the solid boundary represents air chambers side walls (membrane) and dotted boundary represents actuator cover (beam) [© 2022 IEEE].

cover is calculated from the deformation of air chambers using the membrane theory. The adjacent side walls (in YZ plane) of the chambers are modeled as initially flat membranes with clamped edge condition, subjected to lateral pressure. The deformation of the remaining walls is not considered. A schematic of an undeformed membrane with sides $2a$ and $2b$ is shown in Fig. 4.3(c). When subjected to air pressure, the membranes get inflated and come into contact with the adjacent membranes. A detailed schematic of deformed air chambers is shown in Fig. 4.4.

The work done by internal pressure W on the membrane can be calculated using the displaced volume V as

$$W = \int_0^{p_1} V \, dp \, . \tag{4.1}$$

The membrane is assumed to displace a volume equal to

$$V = \pi \, a^2 \, \delta \, . \tag{4.2}$$

The midplane extension δ of the membrane is calculated from (2.1) as

$$\delta = \left(\frac{pa^4}{CEt_m} \right)^{-3} . \tag{4.3}$$

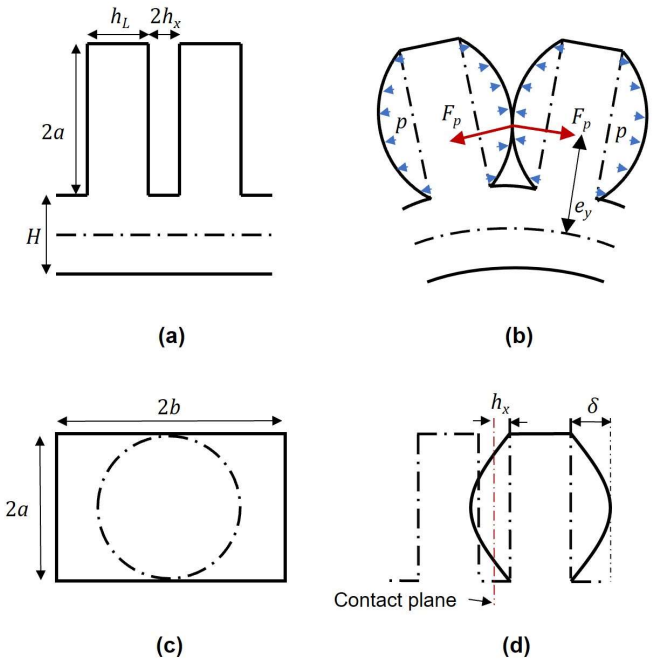

Fig. 4.4 Schematic of air chambers geometry. (a) Undeformed state, (b) deformed state, (c) section view along actuator width showing contact region by dotted curve, and (d) section view along actuator length showing deformed and undeformed geometry [© 2021 IEEE].

After substituting V (4.2) and δ (4.3) into (4.1) and solving the integral, we get

$$W = \frac{3\pi\, a^2\, \delta\, p_1}{4}\,. \tag{4.4}$$

The contact force F_p generated at the contact region is calculated from the work done as

$$\begin{aligned} W &= F_p\,(\delta + h_x) \\ F_p &= \frac{3\pi\, a^2\, \delta\, p_1}{4\,(\delta + h_x)}. \end{aligned} \tag{4.5}$$

The eccentric axial force F_p induced a bending moment M_T on the cover, acting along the Z-axis as

$$M_T = F_p\, e_y\,. \tag{4.6}$$

The developed air chamber model was followed for modeling the free-space and blocked force states of a uniform air chamber geometry actuator [89].

4.3 Finite-Strain Air Chamber Model

The finite-strain modeling of air chambers as an initially flat membrane is presented in this section.

4.3.1 Deformation of Air Chambers

For thin films or membranes, the bending stiffness is negligible. In this study, the inflated membrane is assumed to have a circular geometry, as shown in Fig. 4.3(b). A detailed schematic for the deformation of adjacent air chambers in contact is shown in Fig. 4.5.

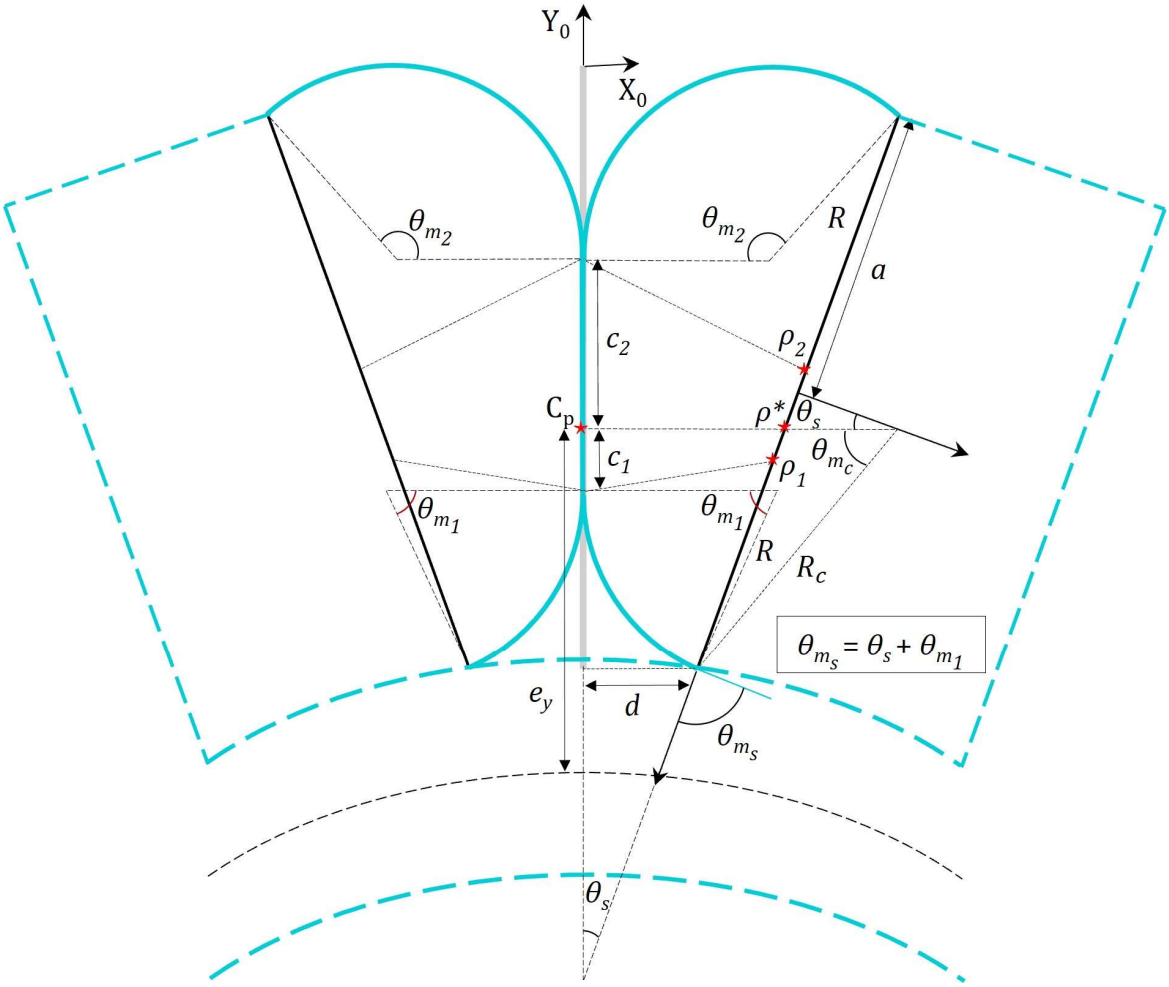

Fig. 4.5 Schematic of deformed geometry of air chambers. The solid aquamarine color lines represents the deformed profile of membranes and dashed lines represent air chambers and actuator cover [© 2022 IEEE].

The derivation of various geometric parameters mentioned in the schematic is presented in subsequent sections.

The deformation of the membranes is assumed to be symmetric about contact plane Y_0Z_0. Initially, in undeformed state, the contact plane is parallel to the membranes (i.e., $\theta_s = 0$), but once the actuator deforms, it becomes inclined to the membranes (i.e., $\theta_s \neq 0$). Towards the interior of deformed air chambers, the membrane is at a distance d from the contact plane (initially, $d = h_x$) that is inclined to the undeformed membrane surface at an angle θ_s, as shown in Fig. 4.6(a). In later derivations, the contact plane is assumed to be a rigid substrate. The deformed profile of an initially flat membrane in contact with an inclined substrate is shown in Fig. 4.6(b). We refer the deformation to cartesian coordinates that are defined along the undeformed membrane surface. We define the surface of the deformed membrane that is not in contact with the substrate as free surface, and it has a circular geometry [91]. The dotted curve in Fig. 4.6(b) denotes the deformed profile of the membrane at contact initiation. The contact begins at point $C_p(x^*, y^*)$ and its location is dependent on parameters d and θ_s. The contact width, unlike that in contact with parallel substrate is not symmetric about the point of contact initiation and is defined by c_1 and c_2 from the point of contact initiation along the substrate. The next subsection discussed the constitutive relations for a square membrane. The deformation of rectangular membrane is predicted from the deformation of square membrane using stretch mapping.

Constitutive Relations for Membrane

The free deformation of the membrane is symmetric about X-axis and two of the principal stretches at the center of the membrane are assumed to be equal (square membrane assumption). The membrane is assumed to be isotropic, incompressible, and hyperelastic. The principal stretches are defined as $\lambda_1 = \lambda_2 = \lambda_m$, and from the incompressibility condition $\lambda_3 = \lambda_m^{-2}$. From the assumption on the deformation state or the principal stretches defined above, the tensions and curvatures become $T_1 = T_2 = T_m$ and $\kappa_1 = \kappa_2 = \kappa_m$, respectively. The equilibrium equation (2.4) for the membrane can then be written as

$$T_m = \frac{p}{2\kappa_m} \,. \tag{4.7}$$

The equilibrium equations are independent of membrane material. We considered the membrane material to be neo-Hookean. For the stretches defined above, the tension T_m for a

neo-Hookean membrane can be written using (2.6) as

$$T_m = \mu \; t_m \left(1 - \frac{1}{\lambda_m^6}\right). \tag{4.8}$$

From (4.7) and (4.8), we get the final equilibrium equation as

$$\frac{p}{2\kappa_m} = \mu \; t_m \left(1 - \frac{1}{\lambda_m^6}\right). \tag{4.9}$$

Now, curvature κ_m is the only unknown parameter and it is defined from the deformed geometry of the membrane.

4.3.2 Free Inflation of Membrane

The membrane experiences free inflation before contact initiation. Before contact, the membrane is symmetric about X-axis and makes an angle θ_{m_f} at the clamped edge, as shown in Fig. 4.6(a). The stretch in the deformed membrane is uniform and from geometry, it can be calculated as

$$\lambda_m = \frac{R_f \; \theta_{m_f}}{a}. \tag{4.10}$$

From the deformed geometry, the radius of curvature R_f can be calculated as

$$R_f = \frac{a}{\sin\theta_{m_f}}. \tag{4.11}$$

From (4.10) and (4.11), the stretch λ_m can be written as

$$\lambda_m = \frac{\theta_{m_f}}{\sin\theta_{m_f}}. \tag{4.12}$$

The maximum inflation δ of the deformed membrane can be calculated as

$$\delta = R_f \left(1 - \cos\theta_{m_f}\right) = a \tan\left(\frac{\theta_{m_f}}{2}\right). \tag{4.13}$$

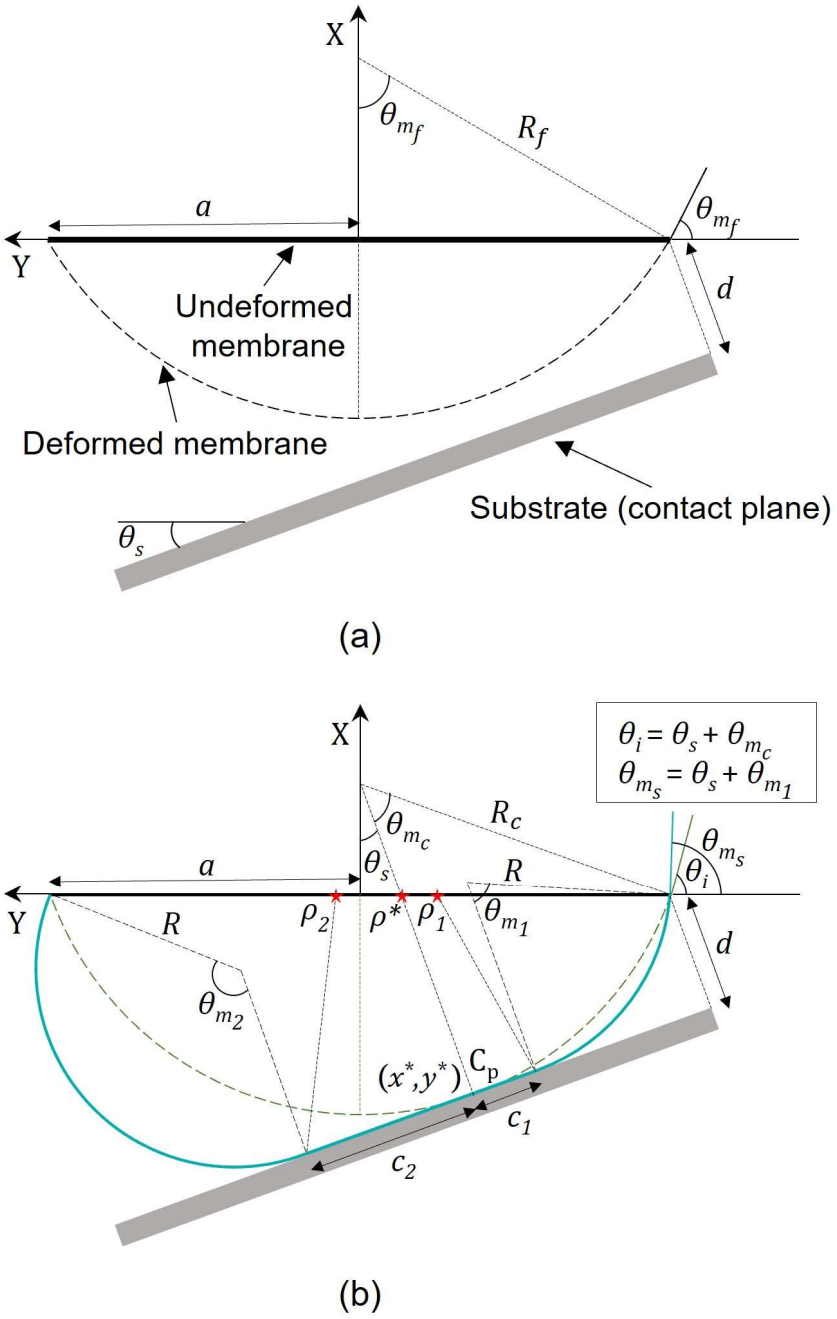

Fig. 4.6 Deformed geometry of an initially flat membrane, (a) before contact and (b) in contact with an inclined substrate. The dotted curve indicates free deformation [© 2022 IEEE].

For deformed circular membrane, the curvature is $\kappa_m = \dfrac{1}{R_f}$. Substituting (4.11) and (4.12) into (4.9), we get the relation between θ_{m_f} and applied pressure p as

$$\sin\theta_{m_f} - \frac{\sin\theta_{m_f}^7}{\theta_{m_f}^6} = \frac{ap}{2\mu t_m} \,. \tag{4.14}$$

Equation (4.14) has a upper limit for pressure p. After a certain value of pressure, the equation has no solution. However, for membrane in contact, the stretch λ_m and R_f are defined using different expressions. In that case, the upper bound on pressure is imposed by θ_{m_2}, with an upper limit π.

For the pneu-net actuator, we can define the minimum pressure p_{in} required to initiate the contact between adjacent air chambers using (4.14). The minimum inflation of air chambers required to make contact with adjacent chambers is $\delta = h_x$. By substituting $\delta = h_x$ into (4.13) and solving it for θ_{m_f}, we get

$$\theta_{m_f} = 2\tan^{-1}\left(\frac{h_x}{a}\right). \tag{4.15}$$

By rearranging (4.14), we get the expression for pressure as

$$p_{in} = \frac{2\mu t_m}{a}\left(\sin\theta_{m_f} - \frac{\sin\theta_{m_f}^7}{\theta_{m_f}^6}\right). \tag{4.16}$$

Contact Initiation

The geometry of the membrane in contact with an inclined substrate is shown in Fig. 4.6(b). The contact begins from point $\mathrm{C}_p(x^*, y^*)$. From deformed geometry, the location of point C_p can be calculated as

$$x^* = -R_c\left(\cos\theta_s - \cos\theta_i\right) \text{ ; and } \quad y^* = R_c\sin\theta_s\ . \tag{4.17}$$

The slope θ_i can be calculated as

$$\frac{d}{a} = \csc\theta_i - \cos\theta_s\cot\theta_i - \sin\theta_s\ . \tag{4.18}$$

The undeformated location $(0, \rho^*)$ of contact initiation point $\mathrm{C}_p(x^*, y^*)$ can be written as

$$\rho^* = a\frac{\theta_s}{\theta_i}\ . \tag{4.19}$$

The contact initiation point is assumed to be stationary and the contact widths are defined with respect to this point.

4.3.3 Inclined Contact Between Membrane and Substrate

First, the left side (exterior) of contact initiation point is investigated and an expression for contact width c_2 is obtained; then from the deformed geometry, the correlation between c_1 and c_2 is developed. If the contact between the membrane and substrate is assumed to be frictionless, then the stretch in the membrane is going to be uniform, i.e., same stretch in free and contact surface. The stretch at the contact edge can be defined either from the free membrane λ_{out} or from the membrane in contact λ_{in}. For frictionless contact, the stretches λ_{in} and λ_{out} are equal. From the deformed geometry, the stretch at the contact edge can be written as

$$\lambda_{in} = \frac{c_2}{\rho^* - \rho_2} \tag{4.20}$$

and

$$\lambda_{out} = \frac{R\theta_{m_2}}{a + \rho_2} \, . \tag{4.21}$$

The undeformed location ρ_2 of the contact edge can be obtained by equating (4.20) and (4.21) as

$$\rho_2 = \frac{R\theta_{m_2}\rho^* - ac_2}{R\theta_{m_2} + c_2} \, . \tag{4.22}$$

The radius of curvature R can be obtained from the deformed geometry as

$$R = \frac{(a+\rho^*)\cos\theta_s - c_2}{\sin\theta_{m_2}} \, . \tag{4.23}$$

The undeformed contact width ρ_2 can be expressed in terms of θ_{m_2} by substituting (4.23) into (4.22) as

$$\rho_2 = \frac{\theta_{m_2}\rho^*\left((a+\rho^*)\cos\theta_s - c_2\right) - ac_2\sin\theta_{m_2}}{\theta_{m_2}\left((a+\rho^*)\cos\theta_s - c_2\right) - c_2\sin\theta_{m_2}} \, . \tag{4.24}$$

From the deformed geometry, the relation between radius of curvature R and offset d can be written as

$$d = R(1 - \cos\theta_{m_2}) - 2a\sin\theta_s \, . \tag{4.25}$$

The contact width c_2 can be expressed in terms of θ_{m_2} by substituting (4.23) into (4.25) as

$$c_2 = (a+\rho^*)\cos\theta_s - (d+2a\sin\theta_s)\cot\left(\frac{\theta_{m_2}}{2}\right). \tag{4.26}$$

The radius of curvature R can be expressed in terms of θ_{m_2} by substituting (4.26) into (4.23) or from (4.25) as

$$R = \frac{d+2a\sin\theta_s}{2\sin^2\left(\frac{\theta_{m_2}}{2}\right)}. \tag{4.27}$$

The stretch λ_m can be calculated by substituting (4.24) and (4.26) into (4.20) as

$$\lambda_m = \cos\theta_s + \frac{d+2a\sin\theta_s}{2(a+\rho^*)}\left[\frac{\theta_{m_2}}{\sin^2\left(\frac{\theta_{m_2}}{2}\right)} - 2\cot\left(\frac{\theta_{m_2}}{2}\right)\right]. \tag{4.28}$$

The tension T_m can be obtained by substituting (4.27) into (4.7) as

$$T_m = \frac{p}{2}\frac{d+2a\sin\theta_s}{2\sin^2\left(\frac{\theta_{m_2}}{2}\right)}. \tag{4.29}$$

By substituting (4.27) and (4.28) into (4.9) we get the final equilibrium equation as

$$1-\lambda_m^{-6} = \frac{p(d+2a\sin\theta_s)}{4\mu\, t_m \sin^2\left(\frac{\theta_{m_2}}{2}\right)}. \tag{4.30}$$

Equation (4.30) is a nonlinear algebraic equation with θ_{m_2} as variable. We can obtain θ_{m_2} by solving (4.30) and c_2 and λ_m by substituting it into (4.26) and (4.28), respectively. Now, c_1 and the contact width c_z along Z_0-direction are the unknown parameters.

Contact Widths

The free-standing portions of the membrane have a uniform radius of curvature. Using this argument, we can define the correlation between c_1, θ_{m_1}, and R. From the deformed

geometry, the clamp angle θ_{m_1} can be expressed in terms of radius R as

$$\theta_{m_1} = \cos^{-1}\left(1 - \frac{d}{R}\right). \tag{4.31}$$

The contact width c_1 on the right half (interior) can be calculated from stretch as

$$c_1 = 2a\lambda_m - R(\theta_{m_1} + \theta_{m_2}) - c_2 \ . \tag{4.32}$$

The contact width c_y along Y_0-axis can be written as

$$c_y = c_1 + c_2 \ . \tag{4.33}$$

The maximum contact width along Z_0-direction exists along the point of contact initiation and it can be calculated by equating the deformed and undeformed lengths along the Z_0-direction; in final form, it can be written as

$$c_z = (c_1 + c_2)\frac{b(a-\rho^*)}{a^2} \ . \tag{4.34}$$

In the equations derived above, if the substrate inclination angle θ_s is set to zero then, we get the parallel contact model, and in that case, $\theta_{m_1} = \theta_{m_2}$ and $c_1 = c_2$.

Finally, we can get the deformed profile of the membrane from (4.27), (4.30), and (4.31). And, from (4.26), (4.32), and (4.34), we can calculate the contact widths to predict the contact force. The developed square membrane model for contact with an inclined substrate is tested on a flat shell actuator. The results are presented in Appendix-B.

4.3.4 Bending Moment for Uniformly Distributed Air Chambers

The contact region between air chambers is assumed to be elliptical and the minor and major axes are defined as c_y and c_z (along Y_0 and Z_0, respectively, see Fig. 4.5). The contact area A_c for the elliptical region can be written as

$$A_c = \frac{\pi}{4} c_y c_z \ . \tag{4.35}$$

The contact force F_p generated by the air chambers can then be calculated as

$$F_p = pA_c \ . \tag{4.36}$$

The force F_p induced a bending moment M_m on the segment $2h_x$ (initially, $d = h_x$) and it can be calculated as

$$M_m = F_p \, e_y \tag{4.37}$$

where e_y is the eccentricity and from the deformed geometry (see Fig. 4.5), it is defined as

$$e_y = \left(\frac{H}{2} + a - \rho^* \right) \cos \theta_s \, . \tag{4.38}$$

The bending moment M_m induced on segment $2h_x$ is one of the driving forces that causes the bending deformation of the cover pad. The gross effect of this driving force is also dependent on other design parameters, i.e., density and length of the air chambers h_L. For segment X_{L_i} the bending deformation caused by M_m is equivalent to the bending deformation caused by an unknown moment M_{p_i} which is applied on the span of X_{L_i}, as represented in schematics Fig. 4.7(a) and (b). The unknown moment M_{p_i} can be calculated by equating the change in strain energy caused by M_m and M_{p_i}, and in final form it has the following expression

$$M_{p_i} = \left(\frac{2h_x \, {M_m}^2}{2h_x + h_L} \right)^{\frac{1}{2}} . \tag{4.39}$$

For a uniform geometry actuator, the bending moment M_{p_i} is uniform throughout actuator length, and in later derivations, it is represented as $M_{p_i} = M_T$. The actuator has a pneu-net geometry and the application point of force F_p is at an offset of e_y from the actuator cover. Thus, the bending moment M_{p_i} is the primary component of F_p. The effect of axial component of F_p is not significant when compared with the effect of bending moment; hence, it is not considered in further discussion.

4.3.5 Bending Moment for Nonuniformly Distributed Air Chambers

For a nonuniform geometry actuator, the deformation and force characteristics of each beam segment are evaluated separately. The free body diagram of a beam segment in the undeformed state is represented in Fig. 4.7(c). At the free end, the bending moments M_{g_i} and M_{F_i} are introduced by the distributed and tip forces, and can be written as

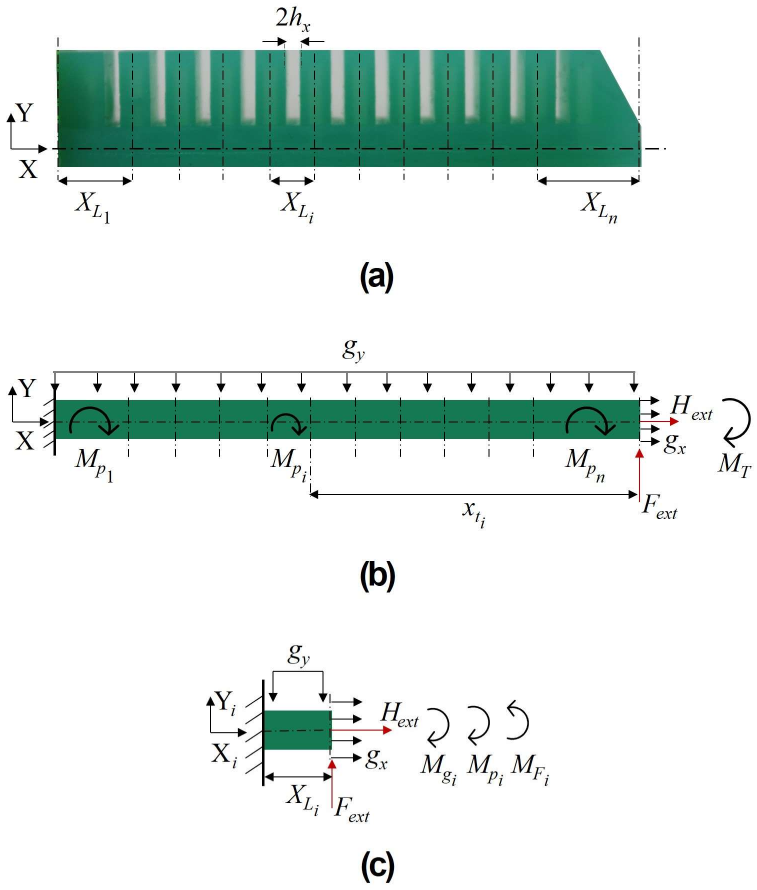

Fig. 4.7 Schematic of (a) beam segments, (b) free body diagram of actuator cover in undeformed state, and (c) free body diagram of a beam segment in undeformed state [© 2022 IEEE].

$$M_{g_i} = \frac{g_y \, x_{t_i}^2}{2} \tag{4.40}$$

$$M_{F_i} = F_{ext} \, x_{t_i} \, . \tag{4.41}$$

For free-space deformation state, the equivalent bending moment M_T at the free end is considered as

$$M_{T_i} = \max\left(M_{p_i}, M_{g_i}\right) \, . \tag{4.42}$$

In the presence of tip forces, the equivalent bending moment M_T is considered as

$$M_{T_i} = M_{p_i} + M_{g_i} - M_{F_i} \, . \tag{4.43}$$

The expressions for M_T are different for the free-space and tip contact states because the application of bending moment M_p is dependent on other forces. The beam segments are serially connected to each other. The final deformation of the actuator is derived by transforming the individual beam segment deformation to a common inertial frame.

Now, the developed air chamber models are integrated with the actuator cover model to formulate the final governing equations of the actuator. The modeling of the actuator cover as a thin beam with a rectangular cross-section is discussed in the next section.

4.4 Modeling of Actuator Cover

The modeling of actuator cover followed the plane-strain hyperelastic thin beam model developed by He *et al.* [106] (see Section-2.3). We reformulated these equations to capture the deformation of the actuator and developed governing equations for the free-space and tip contact states of the actuator.

4.4.1 Free-Space State

In this state, the actuator is subjected to gravitational force and internal pressure. As a general case, an initially inclined state of the actuator is considered for study, as shown in Fig. 4.8. From Section-2.3, for this state, the boundary conditions of the Euler-Lagrange

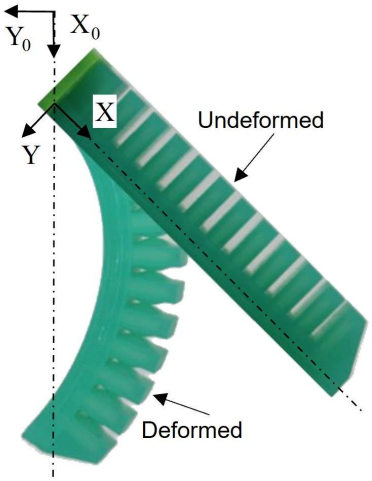

Fig. 4.8 Schematic of free-space deformation state of the actuator [© 2022 IEEE].

beam equations are defined as

$$\begin{aligned} &u_0 = 0,\ v_0 = 0, \text{ and } \theta_0 = 0, \text{ at } X = 0 \\ &P = 0,\ Q = 0, \text{ and } M = M_T, \text{ at } X = L. \end{aligned} \tag{4.44}$$

Integrating the Euler-Lagrange beam equations (2.10) and (2.11) with respect to X yields the following equations

$$T\cos\theta + \frac{M' + m}{\lambda}\sin\theta = -g_x X + C_1 \tag{4.45}$$

$$T\sin\theta - \frac{M' + m}{\lambda}\cos\theta = -g_y X + C_2\ . \tag{4.46}$$

The constants of integration C_1 and C_2 are evaluated by substituting the boundary conditions (4.44) into (4.45) and (4.46). Here, g_x and g_y are components of the gravitational force per unit length along X and Y-directions, respectively, and $m = 0$, as the distributed moment is not applied. After substituting the values of C_1, C_2, T (2.12) and M (2.13) into (4.45) and (4.46), the equations get reduced to the following governing equations

$$\frac{1}{\lambda}\left(\frac{H^2\kappa}{3\lambda^6}\right)' = \frac{g_x(L-X)}{\mu BH}\sin\theta - \frac{g_y(L-X)}{\mu BH}\cos\theta \tag{4.47}$$

$$\lambda - \frac{1}{\lambda^3} - \frac{\kappa^2 H^2}{\lambda^7} = \frac{g_x(L-X)}{\mu BH}\cos\theta + \frac{g_y(L-X)}{\mu BH}\sin\theta. \tag{4.48}$$

The third boundary condition $M = M_T$ at $X = L$ (4.44) is modified using (2.13) as

$$\theta' = \frac{3M_T\lambda^7}{\mu BH^3}. \tag{4.49}$$

To consider terminal forces in the free-space state, modify the boundary conditions at $X = L$ as: $P = H_{ext}$ and $Q = F_{ext}$.

4.4.2 Grasping State

In this state, the actuator is subjected to gravitational force, internal pressure, and constraints at the tip. As a general case, the state of the actuator while grasping an object in pinching mode is considered for study. A grasp between a three-finger gripper and a hexagonal cylinder, as shown in Fig. 4.9(a) is considered. The local coordinates for each finger are attached to the fixed end, and the global coordinates for the gripper are attached to the center of the gripper base. To grasp the object, the actuator has to apply a defined amount of force

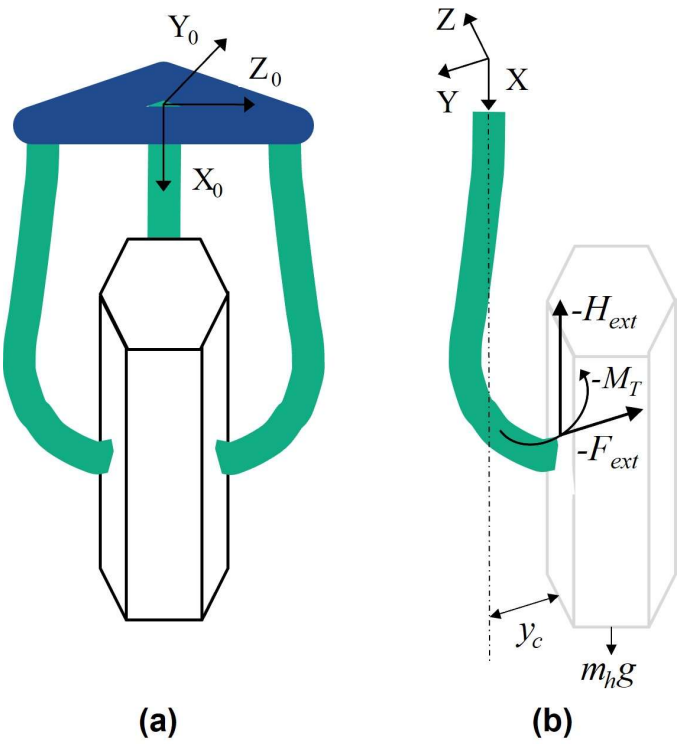

Fig. 4.9 Schematic of (a) deformed state of a three-finger gripper holding a hexagonal cylinder and (b) free body diagram of single finger during the grasp [© 2022 IEEE].

and maintain a specific posture with respect to the object. The amount of force applied by the actuator depends on the weight of the object and contact conditions (static case). The posture depends on the geometry and position of the object with respect to the actuator. As shown in Fig. 4.9(a) and (b), the actuator applied a lifting force H_{ext} along X-direction and maintained an offset y_c at the tip along Y-direction during the grasp. The boundary conditions for this state are defined as

$$\begin{aligned} &u_0 = 0,\ v_0 = 0,\ \text{and}\ \theta_0 = 0,\ \text{at}\ X = 0 \\ &P = H_{ext},\ v_0 = y_c,\ \text{and}\ M = M_T,\ \text{at}\ X = L. \end{aligned} \tag{4.50}$$

The boundary condition at $X = L$ along Y-direction is defined by a functional-type constraint as

$$\int_0^L G(u_0', v_0')dX - y_c = \int_0^L \lambda\ \sin\theta dX - y_c = 0\,. \tag{4.51}$$

The effect of the integral functional constraint $G(u_0', v_0')$ is incorporated into the Euler–Lagrange equations (2.10) and (2.11) using the Lagrange multiplier Λ. The modified governing equa-

tions can then be written as

$$\left(T\cos\theta+\frac{M'+m}{\lambda}\sin\theta\right)'-\left(\Lambda\frac{\partial G}{\partial u_0'}\right)'+g_x=0 \tag{4.52}$$

$$\left(T\sin\theta-\frac{M'+m}{\lambda}\cos\theta\right)'-\left(\Lambda\frac{\partial G}{\partial v_0'}\right)'+g_y=0\ . \tag{4.53}$$

The partial differentials of functional $G(u_0', v_0')$ have the values

$$\frac{\partial G}{\partial u_0'}=0\ \ ;\text{and}\ \ \frac{\partial G}{\partial v_0'}=1\ . \tag{4.54}$$

From variational calculus, the natural boundary condition at $X=L$, along Y-direction is defined as

$$T\sin\theta-\frac{M'+m}{\lambda}\cos\theta-\Lambda=0\ . \tag{4.55}$$

From (2.16) and (4.55), it is concluded that for this state, the Lagrange multiplier Λ represents component Q of stress resultant vector along Y-direction. The stress resultant component Q for this state is the reaction force generated by the actuator at the tip $(X=L)$ along Y-direction. If the coefficient of friction (COF) μ_f at the contact region is known, then from boundary condition $P=H_{ext}$ at $X=L$, the value of Lagrange multiplier should be $\Lambda\geq H_{ext}/\mu_f$, using Coulomb's law of friction. Integrating (4.52) and (4.53) with respect to X yields the following equations

$$T\cos\theta+\frac{M'+m}{\lambda}\sin\theta=-g_xX+C_1 \tag{4.56}$$

$$T\sin\theta-\frac{M'+m}{\lambda}\cos\theta-\Lambda=-g_yX+C_2\ . \tag{4.57}$$

The constants of integration C_1 and C_2 are evaluated by substituting the boundary conditions (4.50) into (4.56) and (4.57) as

$$\begin{aligned}C_1&=H_{ext}+g_x\,L\\ C_2&=g_y\,L\ .\end{aligned} \tag{4.58}$$

Substituting the values of C_1, C_2, T (2.12), and M (2.13) into (4.56) and (4.57) yields the following governing equations

$$M'=\lambda\left(H_{ext}+g_x(L-X)\right)\sin\theta-\lambda\left(\Lambda+g_y(L-X)\right)\cos\theta \tag{4.59}$$

$$\lambda - \frac{1}{\lambda^3} - \frac{\kappa^2 H^2}{\lambda^7} = \frac{H_{ext} + g_x(L-X)}{\mu BH}\cos\theta + \frac{\Lambda + g_y(L-X)}{\mu BH}\sin\theta. \tag{4.60}$$

Equation (4.49) is also part of the set of governing differential equations, when expressed in first order form. The local material line coordinates of actuator cover in the deformed state are determined using the following equations

$$X = \int_0^L \lambda\cos\theta\, dX \tag{4.61}$$

$$Y = \int_0^L \lambda\sin\theta\, dX\ . \tag{4.62}$$

Equation (4.62) also adds an equation to the set of first order differential equations as

$$Y' = \frac{dY}{dX} = \lambda\sin\theta\ . \tag{4.63}$$

For the grasping state shown in Fig. 4.9(a), it is assumed that the deformations of all fingers are identical. The global material line coordinates of the fingers are determined by transforming the coordinates from local to global frame.

Finally, by solving the governing differential [(4.49), (4.59), and (4.63)] and algebraic (4.60) equations, we can calculate the axial stretch and slope at the material line coordinates of the actuator cover in the deformed state. The material line coordinates of the actuator cover in the deformed state can be calculated from (4.61) and (4.62) by substituting the values of the axial stretch and slope.

Chapter 5

Numerical Solution and Applications of the Modeling Approach

5.1 Numerical Solution for Flat Shell Gripper

The governing equations for the shell gripper are nonlinear algebraic equations. The equations were solved numerically using "fsolve, MATLAB R2019b" nonlinear algebraic equation solver. The computations were performed on a desktop computer [Dell Optiplex; Windows 10 Pro; Intel® Core™ i7-9700 CPU @3.00 GHz ×64-based processor; 8 GB RAM]. The average computation time was 1.57 s. The numerical solution of a nonlinear equation depends on the initial guess. In simulations, the initial guesses were chosen on the basis of practically feasible solution range. The simulations were performed for four different states of the actuator: 1) free-space; 2) contact with a flat substrate; 3) contact with a cylindrical substrate; and 4) grasping cylindrical objects. The geometric dimensions of the membrane are: $2a = 32$ mm; $2b = 86$ mm; and $t_m = 1.1$ mm. The Poisson's ratio ν was taken as 0.50.

5.1.1 Free-Space Deformation Simulations

The pseudocode to predict the free-space deformation of the actuator is presented in Algorithm 1. Here, the desired output variable is membrane midplane inflation δ. The predicted deformed geometry of the actuator is shown in Fig. 5.1 (MATLAB figure).

Algorithm 1 Free-Space Deformation

Input: a, b, t_m, μ, p

Output: δ

1 $\theta_m \leftarrow$ Solve (3.7) after substituting (2.6), (3.1), (3.2), (3.4), and (3.5) into it

2 $\delta \leftarrow$ Solve (3.6)

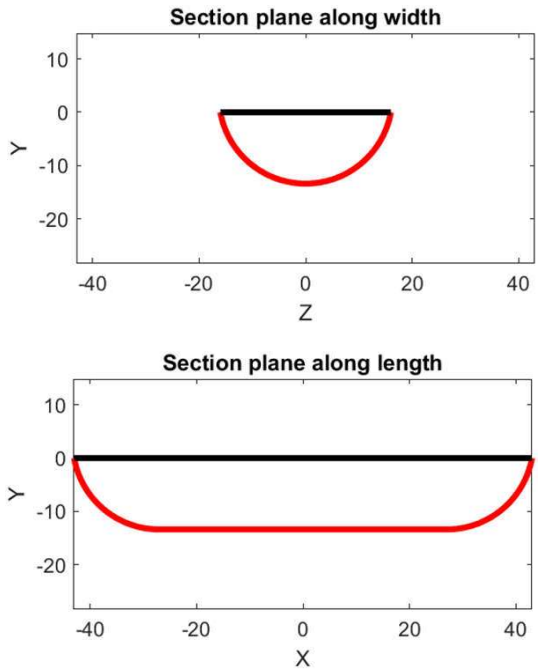

Fig. 5.1 Free-space deformation of the membrane at 15 kPa. The thick black color line represents the undeformed state and the red curve represents the deformed geometry. The predicted midplane inflation δ is 13.38 mm.

5.1.2 Full Contact with Flat Substrate

The pseudocode for the membrane in contact with flat substrate is presented in Algorithm 2. Here, the desired output variable is the normal contact force F_c. The predicted deformed geometry of the membrane is shown in Fig. 5.2.

Algorithm 2 Contact with Flat Substrate

Input: a, b, t_m, d, μ, p

Output: F_c

1 $\theta_m \leftarrow$ Solve (3.7) after substituting (2.6), (3.1), (3.2), (3.8), and (3.11) into it

2 $A_c \leftarrow$ Solve (3.12)

3 $F_c \leftarrow$ Solve (3.13)

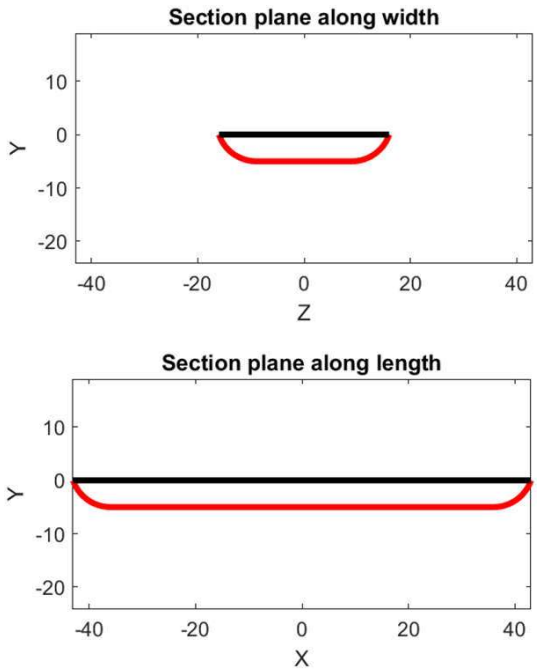

Fig. 5.2 Deformation of the membrane in contact with a flat substrate having 5 mm offset at 15 kPa. The predicted force was 18.33 N.

5.1.3 Contact with Cylindrical Substrate

The pseudocode for the membrane in contact with cylindrical substrate is presented in Algorithm 3. Here, the desired output variable is component F_z of the normal contact force F_c in Z-direction. The predicted deformed geometry of the membrane for symmetric contact case is shown in Fig. 5.3.

Algorithm 3 Contact with Cylindrical Substrate

Input: a, b, t_m, d, r, μ, p

Output: F_z

1 θ_c, θ_{m_a}, R, θ_m, $e \leftarrow$ Solve (2.4), (3.15), (3.16), (3.18), and (3.27) as a set of nonlinear algebraic equations

2 $F_z \leftarrow$ Solve (3.29)

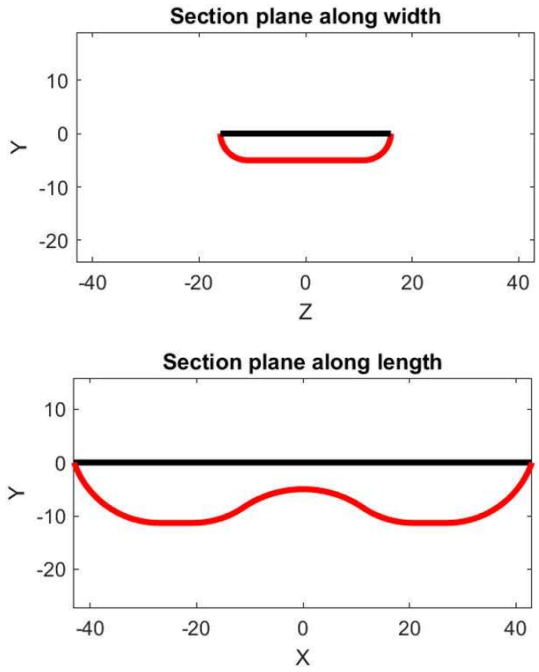

Fig. 5.3 Deformation of the membrane in contact with a cylindrical substrate having 20 mm radius and 5 mm offset at 15 kPa. The predicted force was 5.74 N.

5.1.4 Grasping Simulations

The simulations were performed to predict the air pressure and vertical offset h required to grasp cylindrical objects. The pseudocode of our solution algorithm for grasping state is presented in Algorithm 4. Here, the output variables are offset height h and pressure p that can warrant a successful grasp. The pressure value p_{in} for the initial guess is the pressure required for contact initiation (see Appendix-A, for calculation of pressure required for contact initiation). The cut-off condition or the acceptable force error ε_f was set to 10^{-6} N. The predicted deformed geometry and relative position of the membrane while grasping a circular cylinder is shown in Fig. 5.4.

Algorithm 4 Grasping Cylindrical Objects

Input: F_{ext}, a, b, d, r, t_m, μ

Output: h, p

1 $p \leftarrow p_{in}$ {initial guess pressure}
2 **repeat**
3 θ_c, θ_{m_a}, R, θ_m, e_1, $h \leftarrow$ Solve (2.4), (3.18), (3.27), (3.32), (3.33), and (3.34) as a set of nonlinear algebraic equations
4 $F_c \leftarrow$ Solve (3.13) and (3.28)
5 $p \leftarrow p + \Delta p$
6 **until** $|F_{ext} - F_c| \leq \varepsilon_f$ **or** $(F_{ext} - F_c) \leq 0$

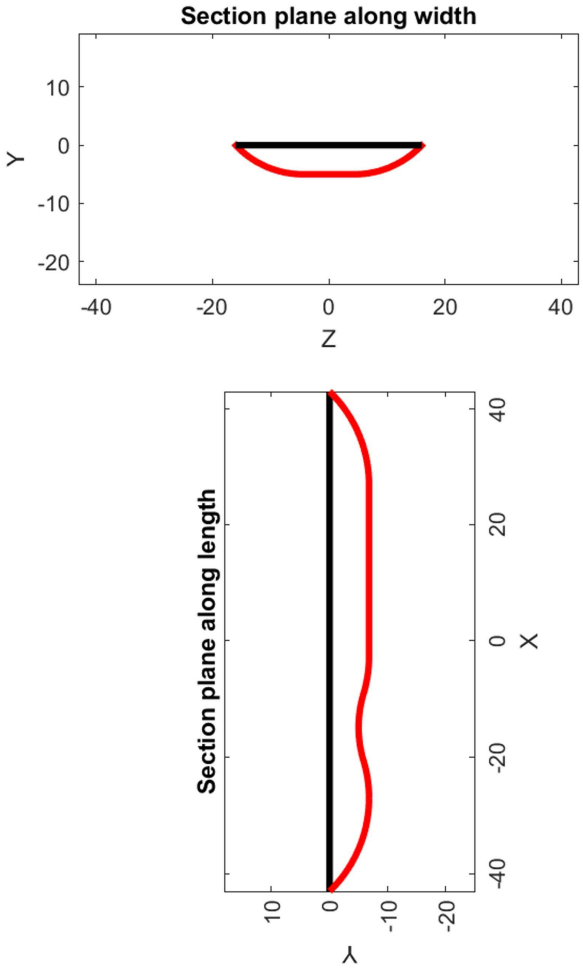

Fig. 5.4 Deformed state of the membrane while grasping a circular cylinder weighing 137 g and having radius 20 mm at 5 mm offset. The predicted pressure and offset h are 5.5 kPa and 28.1 mm, respectively.

5.2 Numerical Solution for Pneu-net Actuator

The governing equations form a set of nonlinear differential and algebraic equations with θ and λ as variables. These equations were solved using an iterative approach. The governing equations for free-space state are (4.47) and (4.48). If we consider λ as a constant parameter, then (4.47) becomes a second-order differential equation, with θ as the variable. Similarly, if θ is considered as a constant parameter, then (4.48) becomes a nonlinear algebraic equation, with λ as the variable. The solution procedure involves the following steps:

1. Solve (4.47) for $\lambda = 1$.
2. Solve (4.48) for θ and θ' obtained from the solution of (4.47).
3. Solve (4.47) for λ obtained from the solution of (4.48).
4. Repeat the above procedure until it meets a specific tolerance for θ.

The differential equations were solved using "bvp5c, boundary value problem solver" while the algebraic equations were solved using "fsolve, nonlinear equation solver". The integral equations (4.61) and (4.62) were solved using "cumtrapz, cumulative trapezoidal numerical integration". The analytical computations were performed for three different states of the actuator: 1) free-space; 2) blocked force; and 3) grasping state. The simulations were

Table 5.1 Pneu-net Actuator Material and Geometric Parameters [© 2022 IEEE]

Actuator Type	**A**	**B**	**C**	**D**
Shore A Hardness	20	30	20	30
Color	Green	Aquamarine	White	Yellow
E (kPa)	409	595	409	595
μ (kPa)	136	198	136	198
$2h_x$ (mm)	1.8		1.5	
t_m (mm)	1.1		1.5	
h_L (mm)	4.2		4.5	
$2a$ (mm)	10		10	
$2b$ (mm)	16		16	
H (mm)	5		5	
B (mm)	20		20	
L (mm)	77		77	

performed for four actuators, made of different geometries and materials of different hardness. The geometric and material parameters of the actuators are listed in Table 5.1.

5.2.1 Free-Space Deformation Simulations

The undeformed state of the actuator was considered horizontal during the simulation. Here, gravity was considered as: distributed forces $g_x = 0$ N/mm and $g_y = -0.002$ N/mm. The pseudocode of our solution algorithm is presented in Algorithm 5. Here, the desired output variables are the material line coordinates $(X,\ Y)$ of the actuator cover. The predicted deformed shape of actuator cover is shown in Fig. 5.5.

Algorithm 5 Free-Space Deformation

Input: Parameters listed in Table 5.1, p, membrane equations (ME), differential (DE) and algebraic (AE) beam equations, and boundary conditions

Output: Material line coordinates $X,\ Y$

repeat
  $\theta_{s_j} \leftarrow 0$ {initial inclination}
  $M_T \leftarrow$ Solve ME, nonlinear algebraic equations
  $\lambda_i \leftarrow 1$ {initial stretch}
  $\theta_i,\ \theta_i' \leftarrow$ Solve DE (4.47)
  $\lambda_{i+1} \leftarrow$ Solve AE (4.48)
  repeat
    $\theta_{i+1},\ \theta_{i+1}' \leftarrow$ Solve DE (4.47)
    $\lambda_{i+2} \leftarrow$ Solve AE (4.48)
  until $|\theta_{i+1} - \theta_i| \leq \varepsilon_0$
  $\theta_{s_{j+1}} \leftarrow$ update θ_s from the deformed geometry of beam
until $|\theta_{s_{j+1}} - \theta_{s_j}| \leq \varepsilon_1$
$X, Y \leftarrow$ Solve (4.61) and (4.62)

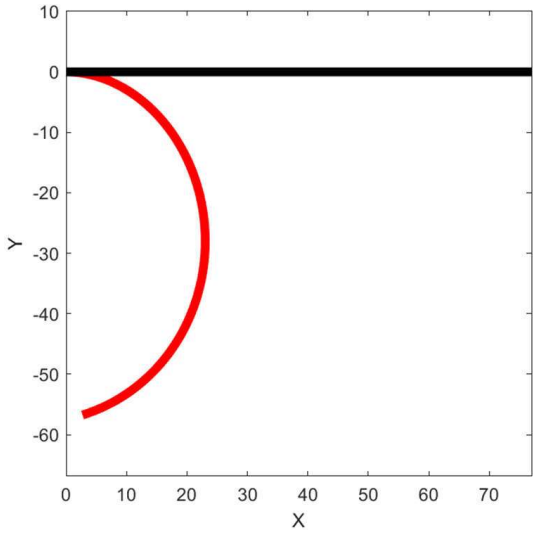

Fig. 5.5 Free-space deformation of type A actuator at 31 kPa.

5.2.2 Blocked Force Simulations

Simulations for the blocked force state were performed to predict the tip force generated by the actuator. The governing equations for the tip contact state were considered, and the boundary conditions were modified as follows: $P = 0$ and $v_0 = y_c = 0$, at $X = L$. The objective of this simulation is to calculate the Lagrange multiplier Λ, which is the force generated at the tip along Y-direction. The pseudocode for our solution algorithm is presented in Algorithm 6. The predicted deformed shape of the actuator cover for zero tip offset in vertical direction is shown in Fig. 5.6.

Algorithm 6 Blocked Force State

Input: Parameters listed in Table 5.1, p, ME, DE, AE, and boundary conditions

Output: Force Λ and material line coordinates X, Y

$\theta_s \leftarrow 0$ {here, inclination is assumed to be fixed}
$M_T \leftarrow$ Solve ME
$\lambda_i \leftarrow 1$ {initial stretch}
θ_i, θ_i', $\Lambda \leftarrow$ Solve DE (4.49), (4.59), and (4.63)
$\lambda_{i+1} \leftarrow$ Solve AE (4.60)
repeat
    θ_{i+1}, θ_{i+1}', $\Lambda \leftarrow$ Solve DE (4.49), (4.59), and (4.63)
    $\lambda_{i+2} \leftarrow$ Solve AE (4.60)
until $|\theta_{i+1} - \theta_i| \leq \varepsilon_0$
$X, Y \leftarrow$ Solve (4.61) and (4.62)

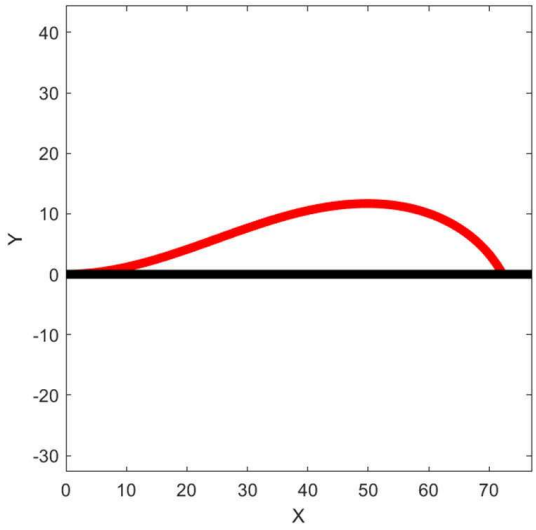

Fig. 5.6 Blocked force deformation of type A actuator at 31 kPa. The predicted tip force was 0.12 N.

5.2.3 Grasping Simulations

Simulations for grasping state were performed to predict the air pressure required to hold an object (static case). These simulations were performed on a three-finger gripper to grasp a hexagonal cylinder (side 15 mm and height 80 mm), circular cylinder (radius 18 mm and height 80 mm), 3-face cone (base side 50 mm and height 80 mm), and right circular cone (radius 30 mm and height 80 mm). The pinching mode was considered for grasping in the simulations. The undeformed state of the actuator was considered to be vertical during the simulation. Here, gravity was considered as: distributed forces $g_x = 0.002$ N/mm and $g_y = 0$ N/mm. The boundary condition at $X = L$ was modified as follows: $P = H_{ext} = m_h g/3$. The force value vertical to the actuator (tip force) required for a stable grasp was obtained using Coulomb's law of friction as $F_{ext} \geq H_{ext}/\mu_f$. For 3-face and circular cones it was obtained as: $F_{ext} \geq H_{ext}/(\mu_f \sin^2\beta)$, where β is the base angle of the 3-face and circular cones.

Algorithm 7 Grasping State

Input: Parameters listed in Table 5.1, F_{ext}, ME, DE, AE, and boundary conditions, y_c

Output: Pressure p and material line coordinates X, Y

$p_j \leftarrow p_{in}$ {initial guess pressure}
repeat
  $\theta_s \leftarrow 0$ {here, inclination is assumed to be fixed}
  $M_T \leftarrow$ Solve ME
  $\lambda_i \leftarrow 1$ {initial stretch}
  $\theta_i,\ \theta_i',\ \Lambda \leftarrow$ Solve DE (4.49), (4.59), and (4.63)
  $\lambda_{i+1} \leftarrow$ Solve AE (4.60)
  repeat
    $\theta_{i+1},\ \theta_{i+1}',\ \Lambda \leftarrow$ Solve DE (4.49), (4.59), and (4.63)
    $\lambda_{i+2} \leftarrow$ Solve AE (4.60)
  until $|\theta_{i+1} - \theta_i| \leq \varepsilon_0$
  $p_j \leftarrow p_j + \Delta p$
until $|F_{ext} - \Lambda| \leq \varepsilon_2$ **or** $p_j \geq p_{max}$
$X, Y \leftarrow$ Solve (4.61) and (4.62)

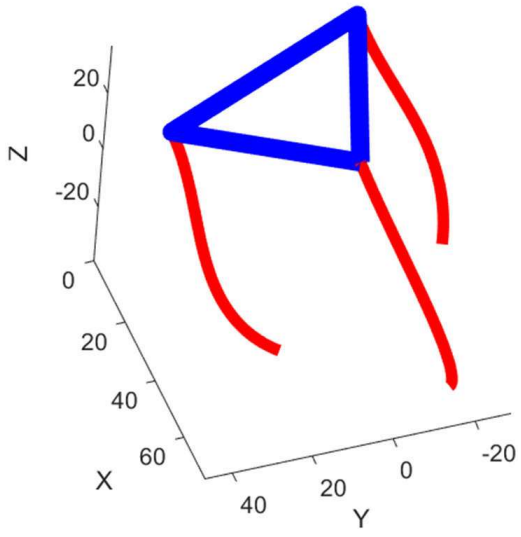

Fig. 5.7 Grasping state deformation of a 3-finger gripper made of type A actuators while grasping a circular cylinder weighing 26 g and having diameter 36 mm . Here, y_c was -1.61 mm and the predicted air pressure was 28 kPa.

The pseudocode for our solution algorithm is presented in Algorithm 7. Here, the pressure value for the initial guess is the minimum pressure required for contact initiation between adjacent air chambers [see Section-4.3.2, equation (4.15) and (4.16)]. If the solution does not converge within a defined number of iterations, then an upper limit on pressure p_{max} can be set to abort the solution. The predicted deformed shape of a 3-finger gripper while grasping the circular cylinder is shown in Fig. 5.7.

The differential equations were solved for 120 discrete node points. The error tolerances ε_0, ε_1, and ε_2 were set to 10^{-3}, 10^{-5}, and 10^{-5}, respectively. For the prescribed error tolerances, the solver usually requires three to ten iterations to determine a solution. The accuracy of the solution improves with an increase in the number of nodes, but after 30 nodes, the variation in solution was very small (less than 1% of solution value). The computation time for the solution was usually less than 60 s. Approximately 60–90% of the computation time was consumed by the "bvp5c" solver. To calculate the deformation of actuator, the solvers have to solve the two governing equations. This is the main reason for lower computation time requirement of the model when compared with the FE-based model, which requires several hours to predict the deformation of the actuator subjected to similar loading conditions. The governing algebraic equation calculates the axial stretch induced in the actuator. The maximum recorded axial stretch was less than 10%. The variation in tip coordinates of the actuator was less than 5% when calculated without considering the axial stretch. In finger-based grippers, bending deformation is the primary objective; hence, the axial stretching effect is optional.

The computation time depends on the number of iterations. For large deformation gradients, the "bvp5c" solver required more iterations to converge. Large deformation gradients occur when the actuator is subjected to forces and moments of higher magnitude. At a higher number of nodes, the solution does not satisfy the solver's internal function tolerances, which results in premature termination of the solver. The numerical solution of a differential equation depends on the initial guess of the solution. For the first iteration, the initial guess was set to $\theta = 0$ and $\theta' = 0$, and from the second iteration, the solution of the previous iteration was considered as the initial guess.

5.3 Finite Element Simulations for Pneu-net Actuator

FE models for simulating the free-space and block force states were constructed using Abaqus, 2017 (Dassault Systèmes, MA). The CAD designs of the actuators were input into Abaqus and meshed with 10-node quadratic tetrahedron elements (C3D10) and the global mesh seed was set to 1 mm. Gravity was included in the simulations and the material densities were set to 1,080 kg/m^3 for DS 20 and DS 30 according to the material datasheet. The same Young's modulus given in Table 5.1 was used in the material property settings. In the block force state, a force sensor was modeled as a cubic part and meshed with 8-node linear hexahedron elements (C3D8R). The contact interactions between the air chambers and between the actuator and the force sensor were modeled using the penalty method with the measured COF. The geometrical nonlinearity was included in the model to account for large deformation. Standard/static simulations were conducted. The reaction force in the vertical direction on the sensor was recorded as the block force and compared with the experimental

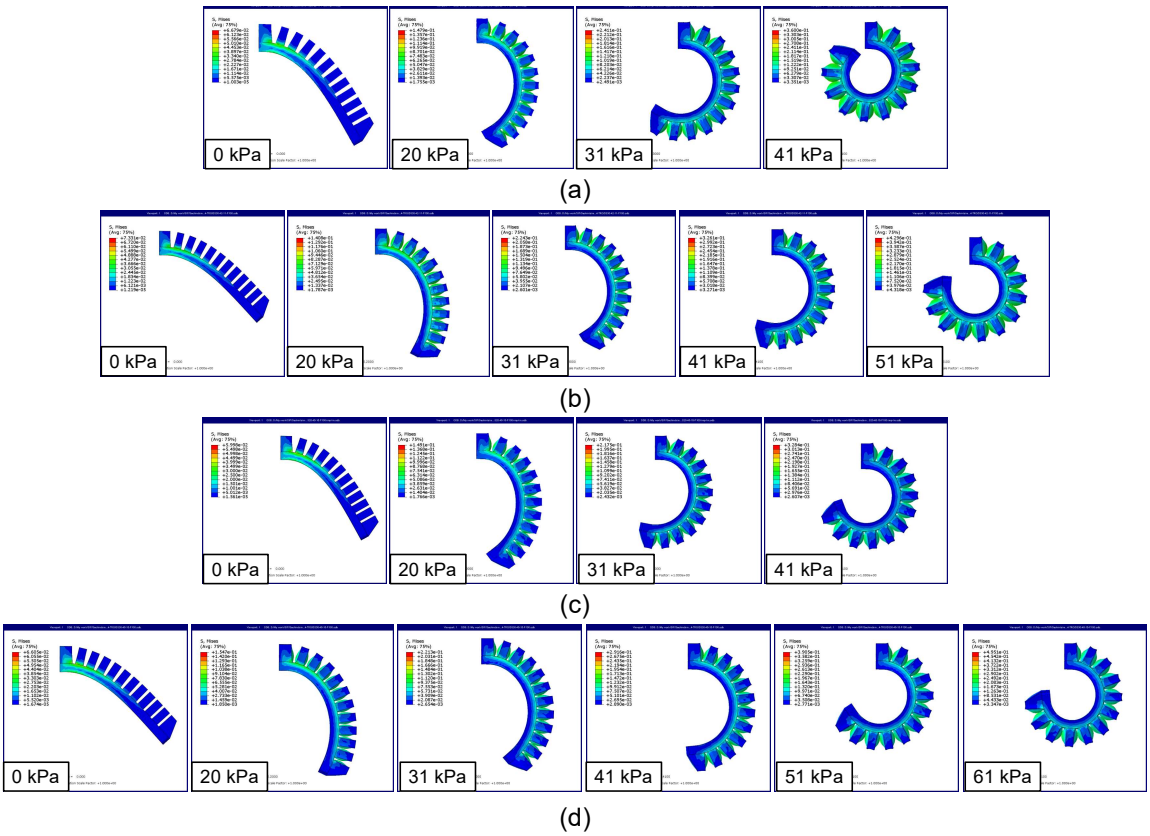

Fig. 5.8 FE simulated free-space deformation of (a) type A, (b) type B, (c) type C, and (d) type D actuators [© 2022 IEEE].

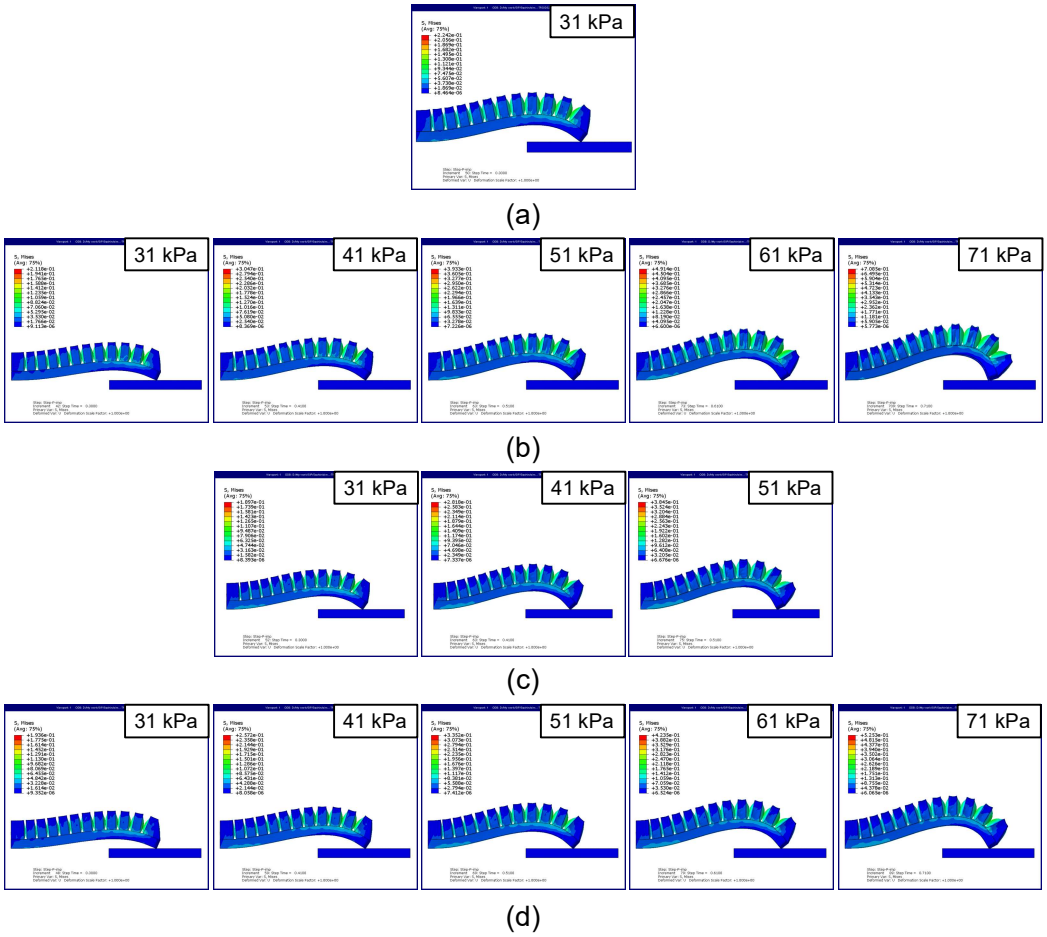

Fig. 5.9 FE simulated block force deformation of (a) type A, (b) type B, (c) type C, and (d) type D actuators [© 2022 IEEE].

measurements. The free-space and blocked force deformations of the actuators as predicted by FE model are shown in Fig. 5.8 and 5.9, respectively.

5.4 Applications of Modeling Approach

The modeling approach discussed in Chapter 3 and 4 is based on the deformed geometric shape assumptions. The assumed geometric shape can be expressed in terms of mathematical equations, thus resulting in simplified governing equations for the actuators. The applications of the presented modeling approach are:

- It is abstract and only requires the geometric and material parameters value, so it can be used at the initial design stage over a large design space as it does not need a CAD file for simulation.
- It provides nonlinear algebraic and differential equations as the final governing equations. From the equations, we can easily see the variation in deformation behavior of the actuators with respect to individual parameters.
- The governing equations can be solved using nonlinear algebraic and differential equation solver using a mathematics software package, like MATLAB or Scilab.
- It is computationally less expensive.
- It can be used to predict the pressure required to grasp objects of known geometry.
- For flat shell gripper, it can also be used to predict the optimum or required relative position of the actuator with respect to the object, i.e., offset h. We can also define the minimum dimension of flat objects (i.e., limit on object height) that the gripper can pick.
- The pneu-net actuator model can be used for other applications as well by modifying the boundary conditions of the governing equation.
- The developed models simultaneously predict the deformation and force characteristics of the actuators.
- The material properties of elastomers are not fixed and in the developed models we can easily tune them to best fit the experimental deformation behavior. As an example, we can tune the material parameters for free space deformation and then use them to predict the force behavior.

Chapter 6

Experiments and Validation of Analytical Models

6.1 Experiments

To capture actual deformation and force characteristics of the actuators, experiments were performed for free-space deformation, force measurement, and grasping states. Air pressure was generated using an off-board compressor (ANEST IWATA SLP-15EFD) and controlled using a digital pressure regulator (SMC ITV2030). The deformation of actuators was captured using a camera (Canon Inc.). The camera images were processed for lens distortion using the "MATLAB R2019b Single Camera Calibrator App". The nodal coordinates of the actuator in the deformed state were extracted using the ImageJ software[1]. The force was measured using a 3-axis force sensor (USL06-H5 Force Sensor, Tech Gihan). The force measurement setup for the shell actuator is shown in Fig. 6.5. Grasping tests for the shell gripper were performed to grasp cylindrical objects using parallel two-finger shell grippers. The objective of grasping tests is to validate analytical model predicted air pressure and vertical offset h required to attain a grasp.

In blocked force state, the pneu-net actuator was initially horizontal and the free end of the actuator was resting on the force sensor, which was rigidly attached to the base, as shown in Fig. 6.18(c). Grasping tests were performed on three-finger grippers to grasp a hexagonal cylinder, circular cylinder, 3-face cone, and right circular cone. The experiments were performed to validate the air pressures predicted by the developed model to attain successful grasps.

[1] [Online]. Available: https://imagej.nih.gov/ij/

6.1.1 Material Properties

The analytical models are based on incompressible neo-Hookean material and they require material shear modulus as an input parameter. Tension tests were performed for Dragon Skin (DS) 20 and DS 30 silicone rubbers (Smooth-On, Inc., PA) using a tensile tester (EMX-275, IMADA, Japan). The test setup is shown in the inset of Fig. 6.1(a) and the dog bone sample used in the tests is shown in the inset of Fig. 6.1(b). Four test samples with a thickness of 2.25 mm were fabricated using casting process. The tests were conducted at a speed of 100 mm/min. The Young's modulus E is obtained from a linear fit to the stress strain data and the shear modulus μ is calculated using the relation

$$\mu = \frac{E}{2(1+\nu)} \,. \tag{6.1}$$

The calculated shear modulus is presented in Table 5.1.

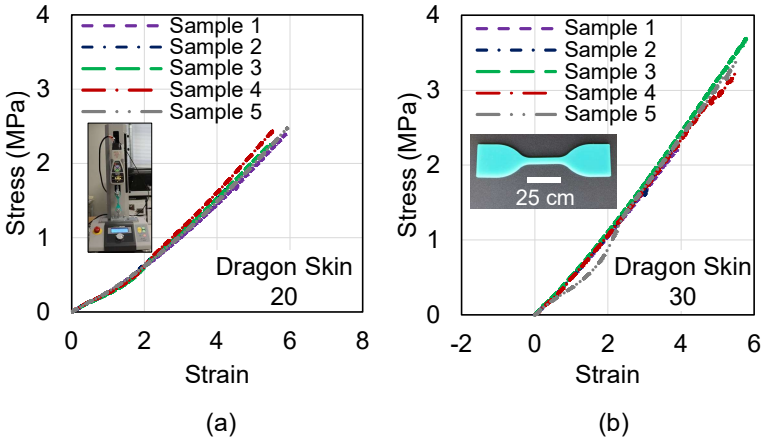

Fig. 6.1 Stress versus Strain curves for (a) DS 20 and (b) DS 30 silicone rubbers [© 2022 IEEE].

6.1.2 Frictional Properties

The frictional properties of actuator material are required for both the analytical and FE simulations. The COF was obtained by conducting experiments on a friction measuring machine (TL201 Tt, Trinity-Lab. Inc., Japan). For the shell gripper, the frictional properties of actuator material are needed for grasping state simulations. To replicate the grasping test conditions, cylindrical shaped test specimens were fabricated using DS silicone rubber and PLA materials. The test specimens are shown in Fig. 6.2(a) and (b). The COF was measured for the contact between DS and PLA materials and the test data is presented in Fig. 6.2(c).

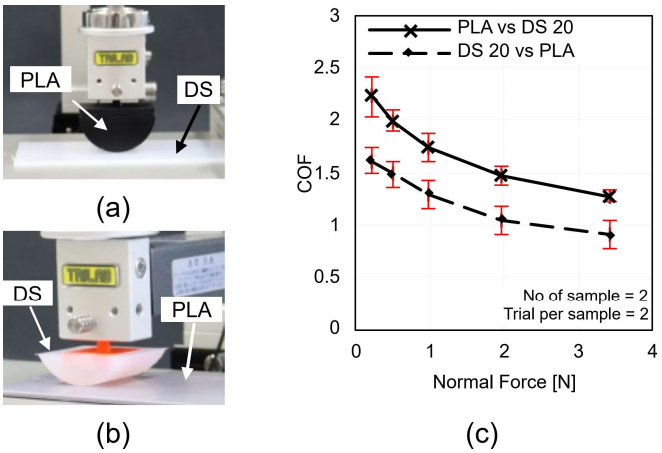

Fig. 6.2 COF measurement experiment for shell gripper. (a) Setup for PLA versus DS 20 (interaction of hard specimen on soft surface), (b) setup for DS 20 versus PLA (soft specimen on hard surface), and (c) test data [© 2022 IEEE].

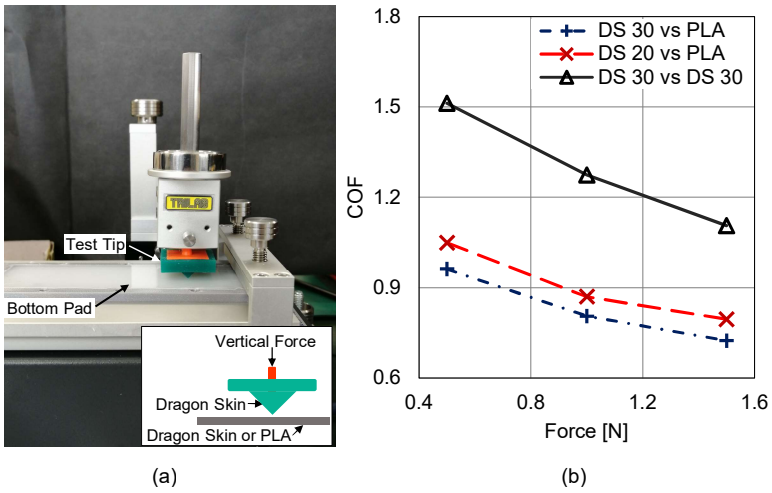

Fig. 6.3 COF measurement experiment for pneu-net actuator. (a) Experimental setup and schematic of friction tester tip and (b) friction test data for DS 30 versus PLA, DS 20 versus PLA, and DS 30 versus DS 30 [© 2022 IEEE].

The test setup for the pneu-net actuator specimen is shown in Fig. 6.3(a). A V-shaped test specimen fabricated using DS material was used to replicate the tip contact conditions. The COF was measured for the contact between DS versus DS silicone rubber and DS versus PLA materials. The friction test data is presented in Fig. 6.3(b). In pneu-net actuator simulations, we considered the COF value corresponding to $0-0.5$ N since the force magnitude in the grasping simulations was in this range.

6.2 Flat Shell Gripper Results

For the experiments, we fabricated shell grippers using DS 20 silicone rubber. The experimental shear modulus was 136 kPa; however, in simulations, it was assumed to be 175 kPa. The shear modulus was tuned to best fit the theoretical free-space deformation with experimental deformation.

6.2.1 Free-Space Deformation

The snapshots of free-space deformation of the actuators are shown in Fig. 6.4(a). The theoretical and experimental mid-plane inflation δ of the membrane is presented in Fig. 6.4(b). The root mean square error (RMSE) for mid-plane extension is 0.56 mm. The experimental deformed profiles differ slightly from the theoretical profiles. This happens due to the boundary conditions of the membrane. In the analytical model, the membrane was assumed to be rigidly clamped at the ends; however, in experiments, the boundaries have little flexibility. In addition, due to manual fabrication, the experimental deformed profiles vary slightly among different actuators [see standard deviations in Fig. 6.4(b)].

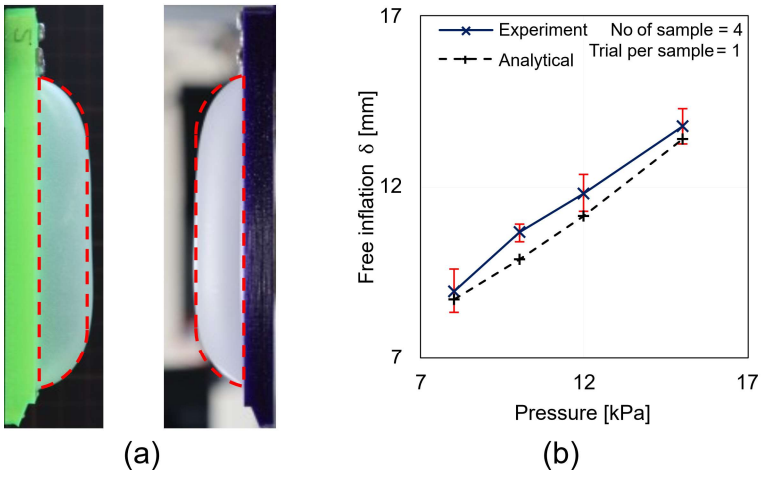

Fig. 6.4 Free-space deformation of the actuators. (a) Experimental snapshots at 15 kPa and (b) plot of mid-plane inflation δ versus air pressure. Dotted red curve in (a) represents theoretical deformed profile of the membrane at 15 kPa [© 2022 IEEE].

6.2.2 Full Contact with Flat Substrate

The theoretical and experimental deformed profiles and contact forces for the actuators in contact with a rigid flat substrate are presented in Fig. 6.5(a) and 6.6, respectively. In experiments, the force was measured for 5 mm and 10 mm offsets. The contact width

predicted by the analytical model [see Fig. 6.5(a)] matches well with the experimental contact width. The force behavior predicted by the analytical model is also similar to the experimental behavior. The RMSE's for 5 mm and 10 mm offsets are 1.32 N and 2.44 N, respectively.

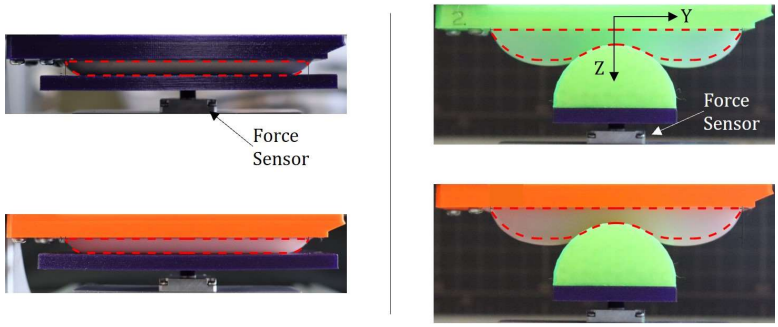

Fig. 6.5 Theoretical (dotted red curve) and experimental deformed profile of the actuators for 5 mm offset. (a) Full contact with flat substrate and (b) contact with cylindrical substrate at 15 kPa [© 2022 IEEE].

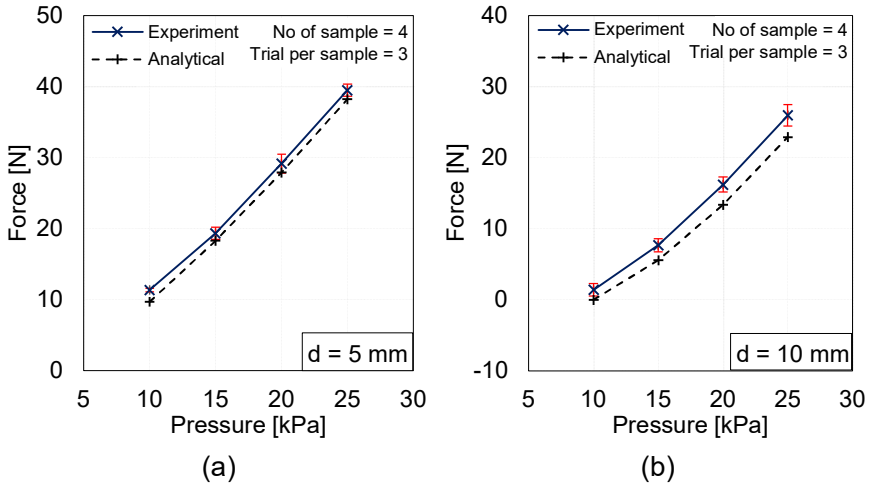

Fig. 6.6 Theoretical and experimental force plots for actuator in contact with rigid flat substrate. (a) 5 mm offset and (b) 10 mm offset [© 2022 IEEE].

6.2.3 Contact with Cylindrical Substrate

The theoretical and experimental deformed profiles and contact forces for the actuators in contact with a cylindrical substrate are presented in Fig. 6.5(b) and 6.7, respectively. The experimental force was measured for four offsets, i.e., 3, 5, 8, and 10 mm. The theoretical

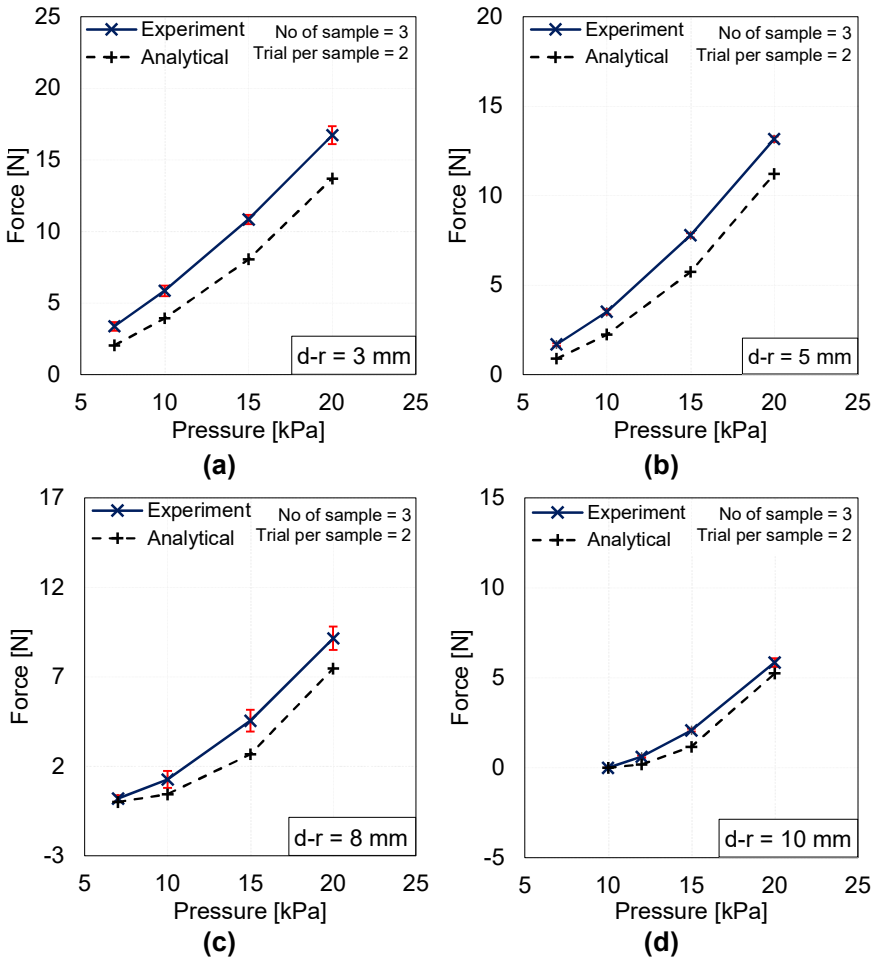

Fig. 6.7 Theoretical and experimental force plots for actuators in contact with cylindrical substrate at different offsets $d - r$ [© 2022 IEEE].

deformation of the actuators [see Fig. 6.5(b)] is slightly smaller than the actual deformation. The force behavior predicted by the analytical model also varies slightly among the offsets. This occurs due to boundary conditions of the membrane and resultant direction of the normal contact force. The boundary gets stretched a little with the deformation of the membrane and this results in contact area increment and thus additional force. At the same magnitude of air pressure, the membrane deforms more at lower offset. At 20 kPa, the discrepancy for 3 mm offset is the highest. In experiments, we measured the force generated by the actuator along the Z-direction [see Fig. 3.6(e) and 6.6(b)]; however, in simulations, we predicted the normal force at the contact region. The contact region exhibits a curved shape, so we calculated the force in Z-direction by projecting the contact area to a plane normal to Z-direction (3.29). For grasping, we used the normal force directly to predict the lifting force. The RMSE's for the above-mentioned offsets are 1.33, 1.59, 2.36, and 0.63 N, respectively.

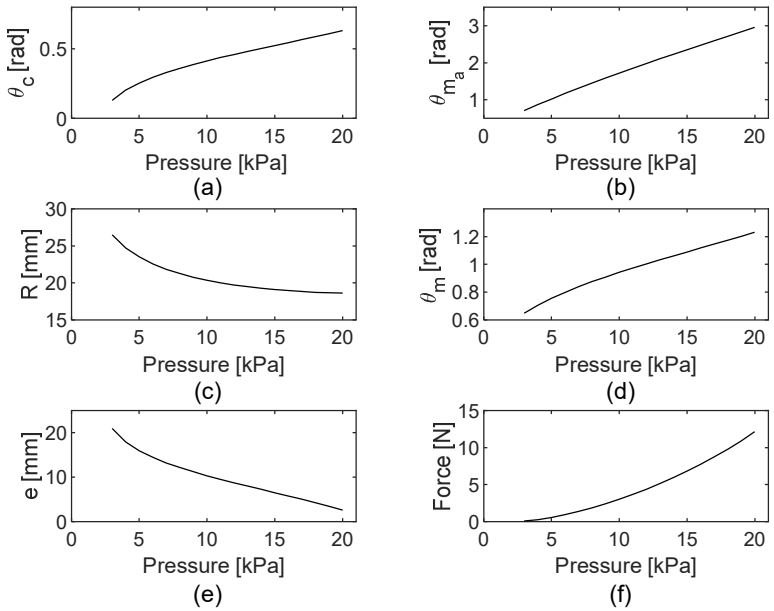

Fig. 6.8 Parameter variation with pressure for 5 mm offset cylindrical contact [© 2022 IEEE].

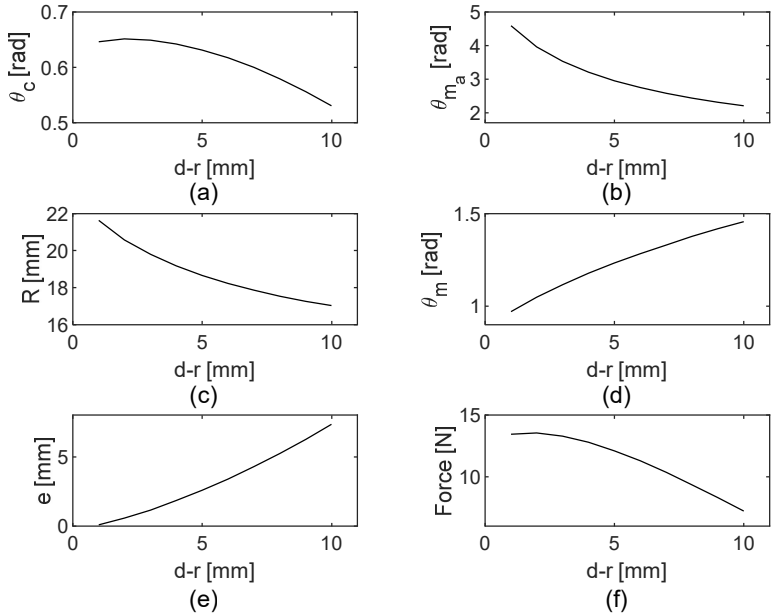

Fig. 6.9 Parameter variation with offset $d - r$ for cylindrical contact at 20 kPa air pressure [© 2022 IEEE].

For controlling a parallel gripper, the only adjustable parameters are air pressure and the offset $d - r$. The lifting force required to grasp an object can be achieved by different combinations of pressure and offset. In order to understand the deformation behavior of the actuator with respect to pressure and offset, we investigated the variation of output variables involved in the solution of nonlinear algebraic equations via simulations. The variation with

air pressure is presented in Fig. 6.8. Here, the contact angle θ_c represents the contact area and it increases with increase in pressure. The parameter e represents the portion of membrane with zero curvature and it decreases with increase in pressure. Practically, this variation seems appropriate. The variation with object offset $d-r$ is presented in Fig. 6.9. The contact angle in this case decreases with increase in $d-r$. The portion of membrane with zero curvature increases with increase in $d-r$. This variation also coincides with experience.

6.2.4 Grasping

The COF at the contact region is needed to calculate the normal force required to hold the objects. To determine the COF, friction tests were performed with two different setups,

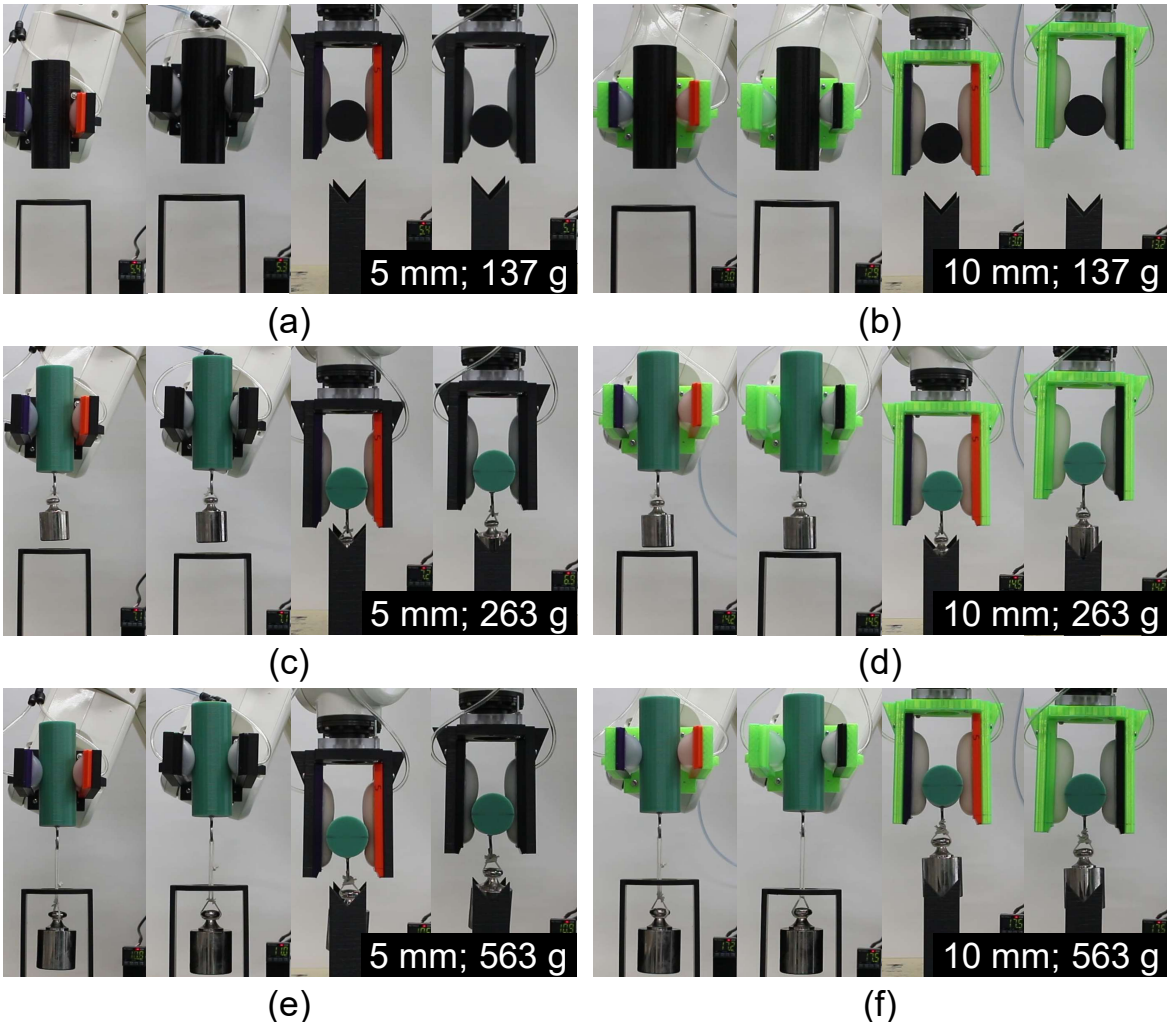

Fig. 6.10 Experimental photo snapshots of two parallel flat shell grippers grasping circular cylinders in horizontal and vertical postures [© 2022 IEEE].

Table 6.1 Analytical Model Predicted Grasping Test Data and Experimental Test Results [© 2022 IEEE]

Cylinder		Offset ($d-r$) 5 mm				Offset ($d-r$) 10 mm			
Diameter	**Weight**	***h***	***p***	**Grasp Status**		***h***	***p***	**Grasp Status**	
(mm)	(g)	(mm)	(kPa)	VP	HP	(mm)	(kPa)	VP	HP
40	137	28.1	5.5	G	G	26.4	13.0	G	G
40	263	30.3	7.2	G	G	27.9	14.5	G	G
40	563	33.7	10.9	G	G	32.1	17.5	G	G

VP – vertical posture of cylinder; HP – horizontal posture of cylinder;
G – grasp.

having contact conditions similar to the grasping experiments, as shown in Fig. 6.2(a) and (b). For worst case scenario, the test data for DS 20 versus PLA was used in the simulations to determine the normal force. The experimental COF varies with normal force; therefore, the COF taken in the simulations was different for each object. The COF was decided on the basis of required lifting force. We defined the lifting force F_L as the force required to hold the object which is applied tangentially to the contact surface (for static case, the lifting force is assumed to be equal to gravity force). The required normal force F_{ext} is then calculated from the lifting force F_L using Coulomb's law of friction as

$$F_{ext} = \frac{1}{\mu_f}\frac{F_L}{2} = \frac{1}{\mu_f}\frac{mg}{2}\,. \tag{6.2}$$

Here, we are using a parallel two-finger shell gripper, so we divided the lifting force per finger. Based on the required normal force, air pressure and vertical offset h were calculated using the analytical model for 5 and 10 mm object offsets. The predicted test data is presented in Table 6.1.

The grasping tests were performed with three 3D printed circular cylinders (PLA material) and two parallel grippers, as shown in Fig. 6.10. The experiments were performed for both horizontal and vertical postures of the cylinders. In experiments, the objects were first grasped at the predicted vertical offset, and a pressure slightly higher than the predicted value. Then, the pressure was reduced to see if the object slips or not at the predicted value. The grippers were able to grasp the objects at the predicted pressure and offset.

6.2.5 Eccentric Grasp of Cylindrical Object

The experiments for eccentric grasp of cylindrical objects were performed to validate the analytical model predicted air pressure required to resist the tilting behavior. The analytical model predicted test data is presented in Table 6.2. The photo snapshots of the eccentric grasp are shown in Fig. 6.11. At the predicted pressure, the gripper almost gets a horizontal grasp; however, some tilting effect still remains. This occurs due to stretching of the membrane. The membrane is made of silicone rubber and it gets stretched in the tilting direction due to eccentric force.

Table 6.2 Analytical Model Predicted Air Pressure for Eccentric Grasp of Cylindrical Objects

Eccentricity x_e (mm)	Diameter 40 mm; Weight 263 g; offset 5 mm		Diameter 40 mm; Weight 563 g; offset 5 mm	
	Traction Force F_t (N)	**Pressure** p (kPa)	**Traction Force** F_t (N)	**Pressure** p (kPa)
0	0.68	5.34	1.83	7.9
5	2.18	8.58	4.12	11.62
10	3.38	10.55	6.95	15.09
15	4.46	12.08	10.32	18.38

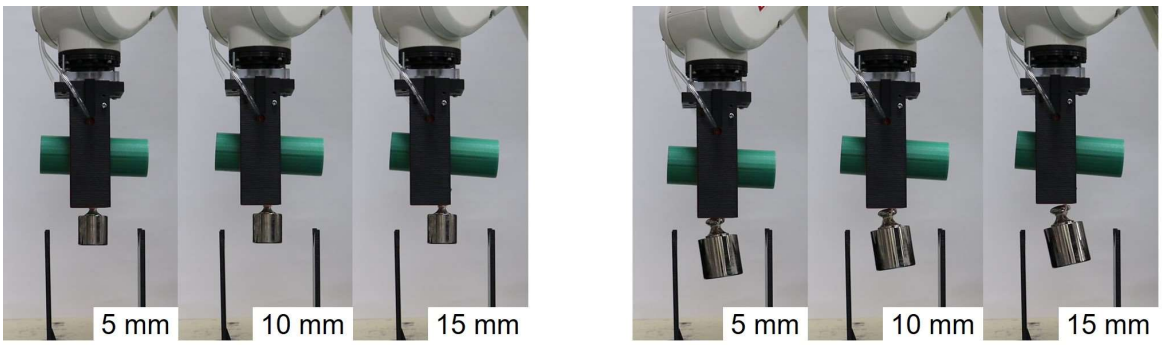

Fig. 6.11 Experimental photo snapshot of eccentric grasp of circular cylinders weighing (a) 263 g and (b) 563 g.

6.3 Pneu-net Actuator Results

For the experiments, we fabricated four sets of pneu-net actuators with uniform air chamber geometry, with DS 20 and 30 silicone rubbers. The geometric and material parameters of the actuators are presented in Table 5.1. Here, finite-strain air chamber model-based results for the pneu-net actuator are presented. For infinitesimal-strain air chamber model based pneu-net actuator results, refer [89].

6.3.1 Free-Space Deformation

Uniform Air Chamber Geometry Actuators

The experimental snapshots of free-space deformation at different air pressures are shown in Fig. 6.12. The experimental, analytical and FE simulated free-space deformation plots of

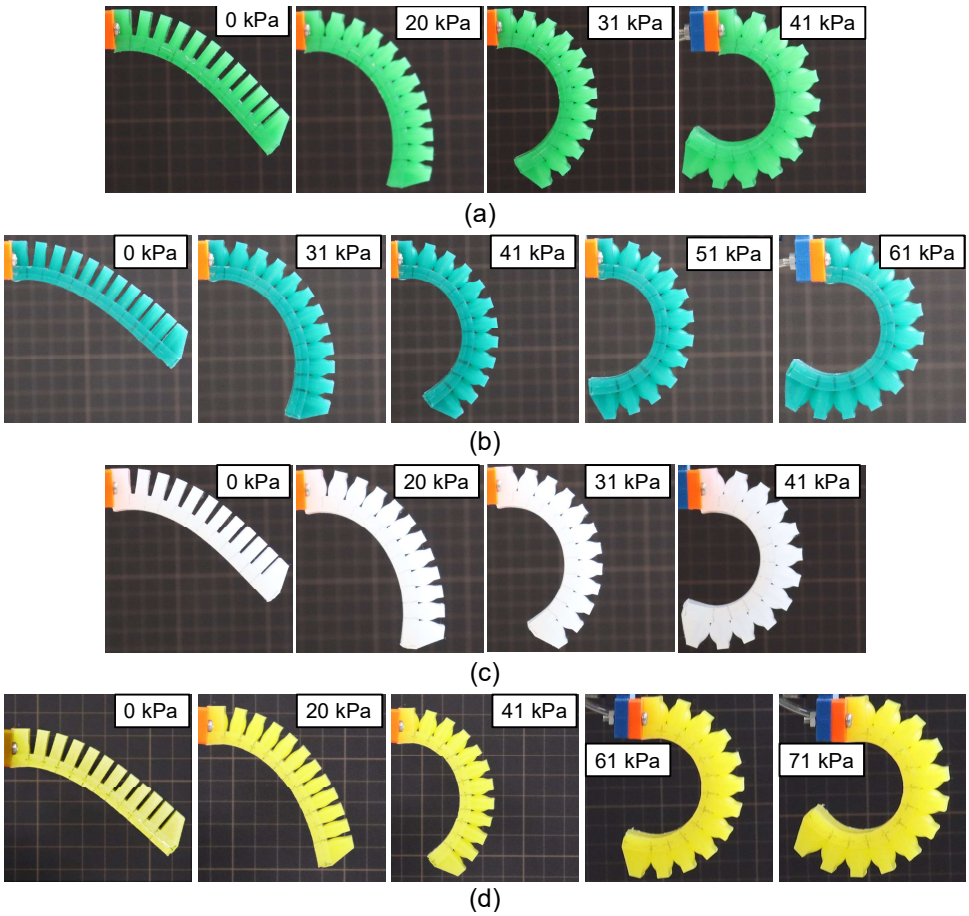

Fig. 6.12 Experimental snapshots of free-space deformation of (a) type A, (b) type B, (c) type C, and (d) type D actuators [© 2022 IEEE].

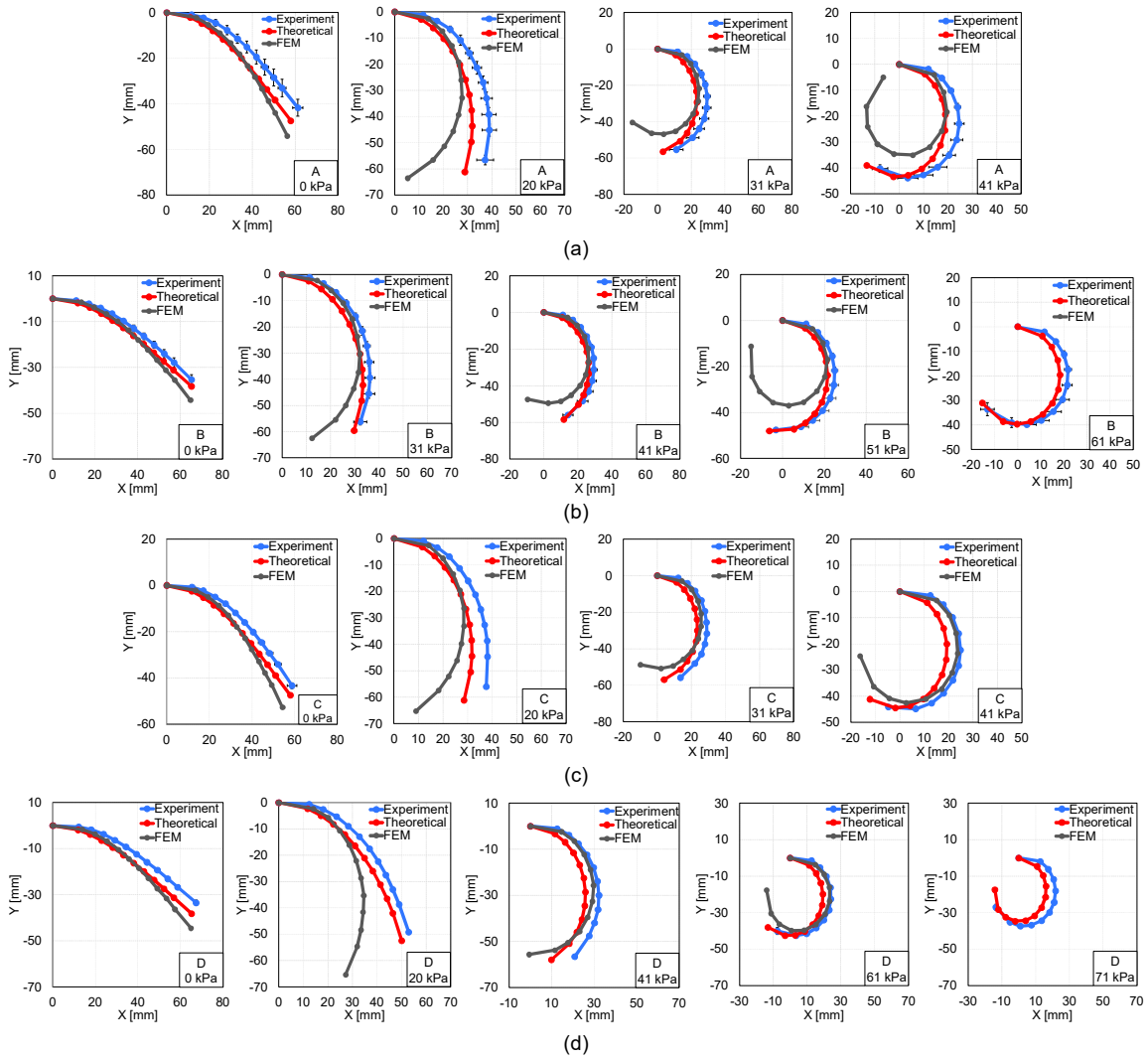

Fig. 6.13 Theoretical, FEM, and experimental free-space deformation plots of (a) type A, (b) type B, (c) type C, and (d) type D actuators. Error bars indicate the standard deviation among 9 trials [© 2022 IEEE].

the actuators at different air pressures are shown in Fig. 6.13. The deformation predicted by the analytical model is close to the experimental deformation of the actuators, while the FE simulations overestimate the deformation. The upper limit of air pressure for the analytical model is the same as that of the FE model for type A [see Fig. 6.13(a)] and C [see Fig. 6.13(c)] actuators, but higher for type B [see Fig. 6.13(b)] and D [see Fig. 6.13(d)] actuators. The FE model did not predict the deformation of type B and D actuators beyond 51 and 61 kPa, respectively, whereas the analytical model predicts up to 61 and 71 kPa for type B and D actuators, respectively. The accuracy of the analytical model for estimating the free-space deformation is better than that of the FE model. Near the clamped end of the

actuators, the deformation predicted by the analytical model is greater than the experimental and FE deformations. This occurs because of the additional stiffness provided by the air chambers to the actuator cover.

Uniform Air Chamber Geometry Actuators Having Different Length (different number of chambers)

In order to see how accurately the analytical model predicts the deformation behavior of actuators having different number of air chambers and having different length, we designed three actuators having different number of air chambers and different length, and carried out FE and analytical simulations. The actuators have 9, 11, and 13 chambers of identical geometry and have length 66 mm, 78 mm, and 90 mm, respectively. The free-space deformation simulation results are presented in Fig. 6.14, Fig. 6.15, and Fig. 6.16. Type C and D actuators were made of DS 20 and 30 silicone rubbers, respectively. In comparison to FE simulations, the analytical simulations have the same tendency as they have in Fig. 6.13.

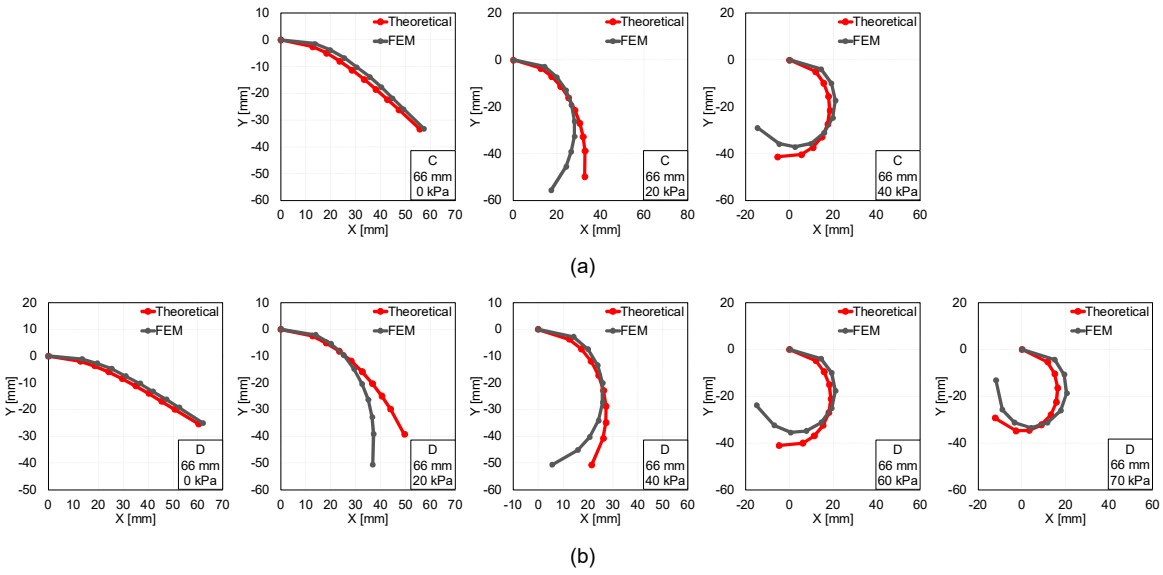

Fig. 6.14 Theoretical and FEM free-space deformation plots of 66 mm length actuator [© 2022 IEEE].

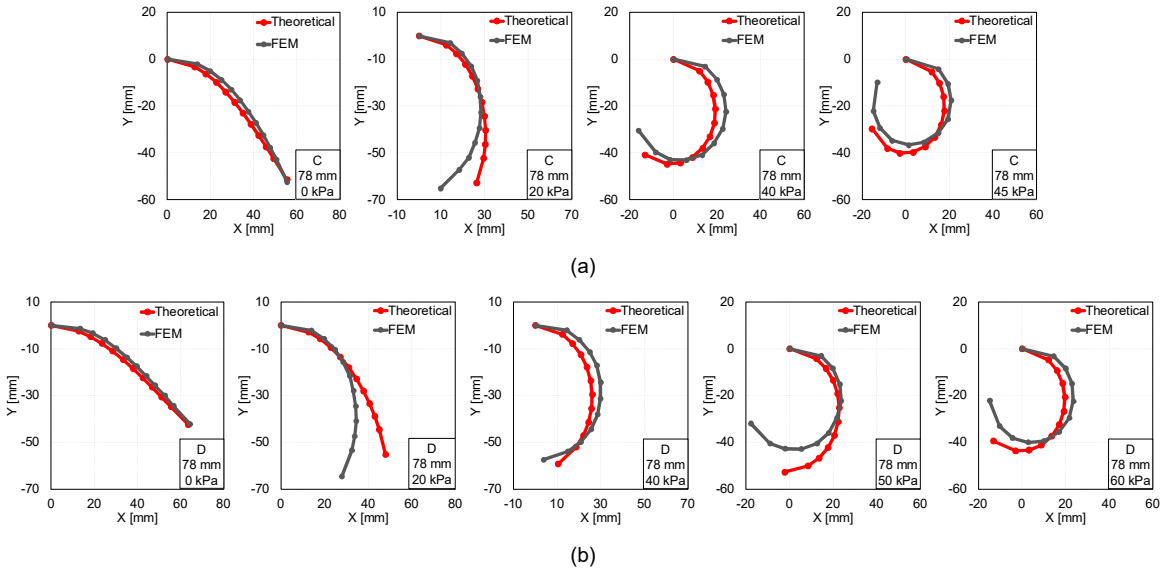

Fig. 6.15 Theoretical and FEM free-space deformation plots of 78 mm length actuator [© 2022 IEEE].

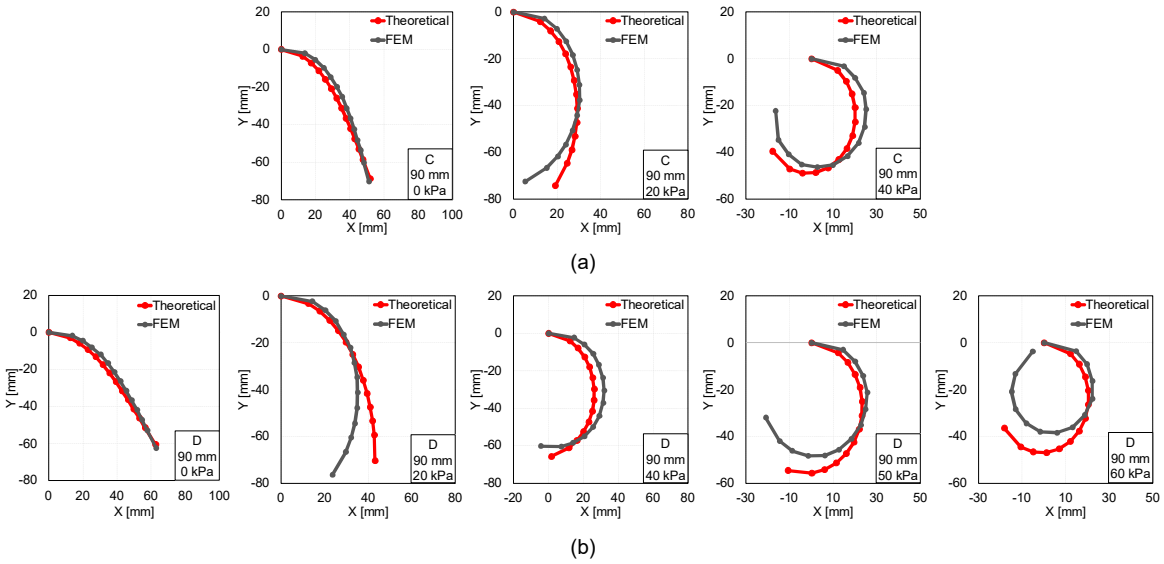

Fig. 6.16 Theoretical and FEM free-space deformation plots of 90 mm length actuator [© 2022 IEEE].

Nonuniform Air Chamber Geometry Actuator

The nonuniform geometry model was tested on an actuator made with a nonuniform air chamber distribution. Experimental snapshots of free-space deformation of the actuator are shown in Fig. 6.17(a). The actuator has denser chambers towards the tip. The experimental and analytical model simulated free-space deformation plots of the actuator are shown in Fig. 6.17(b). The deformation behavior predicted by the analytical model matches well with the experimental behavior.

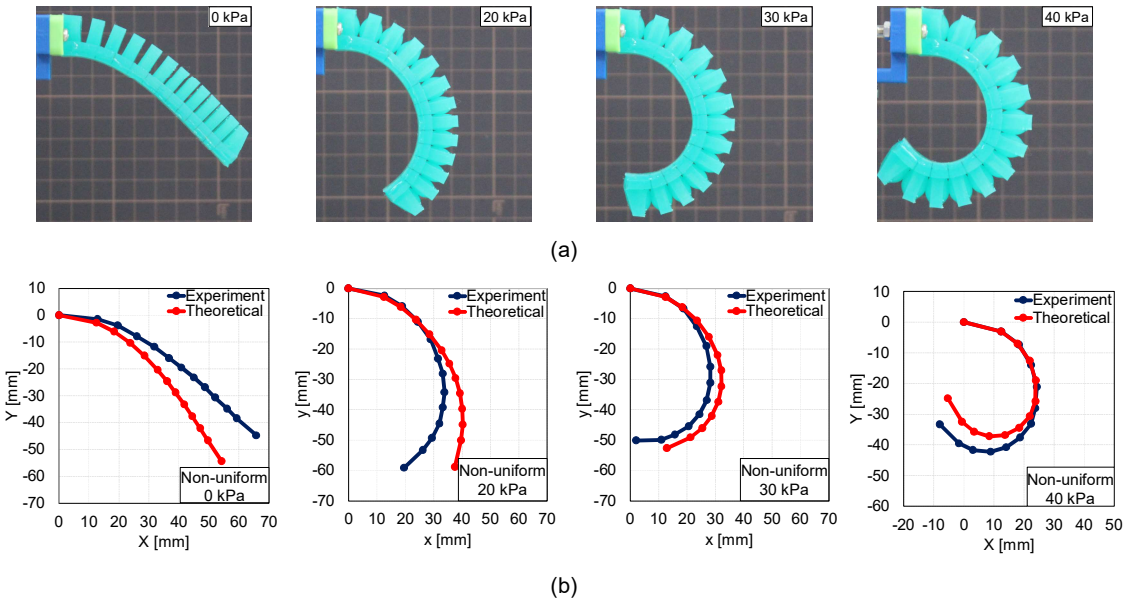

Fig. 6.17 Free-space deformation of a nonuniform geometry actuator. (a) Snapshots of experimental deformation and (b) plots of experimental and analytical model predicted deformation [© 2022 IEEE].

6.3.2 Blocked Force

Uniform Air Chamber Geometry Actuators (parallel contact or zero vertical offset at tip)

The experimental snapshots of blocked force deformation of the actuators are shown in Fig. 6.18. The experimental, analytical, and FE simulated blocked force plots of the actuators are shown in Fig. 6.19. The force results are presented for 30 kPa to 70 kPa air pressure. For air pressure below 30 kPa, the force generated by the actuators is very low in magnitude (i.e., less than 0.1 N) and it was hard to measure using our force sensor. The analytical and FE models can predict the blocked force up to 41 and 30 kPa, respectively, for type A [see Fig. 6.19(a)], and up to 51 kPa for type C actuator [see Fig. 6.19(c)]. The analytical and FE models predict the blocked force up to 71 kPa for type B [see Fig. 6.19(b)] and 61 and

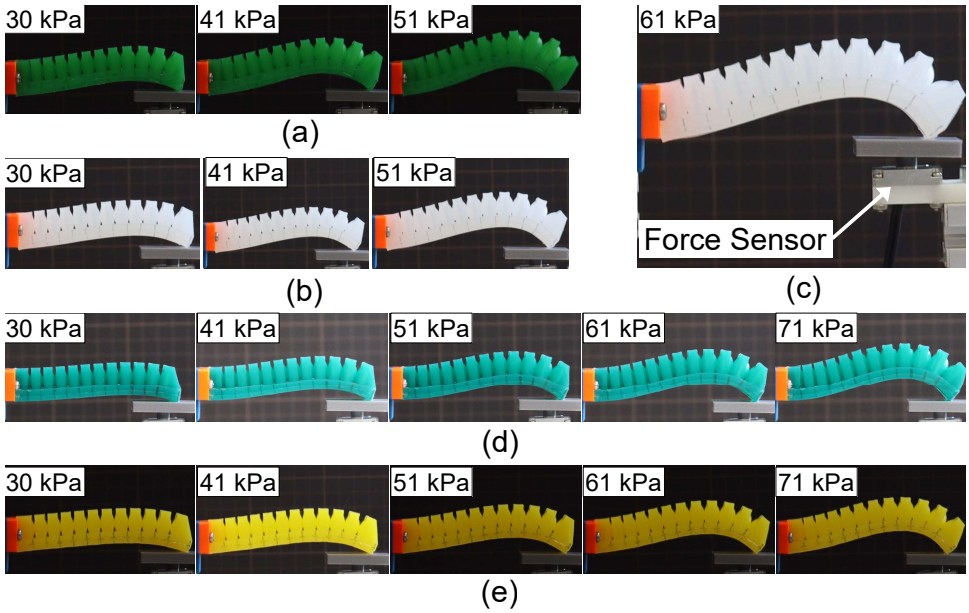

Fig. 6.18 Experimental snapshots of blocked force deformation of (a) type A, (b) type C, (c) type C, (d) type B, and (e) type D actuators. The experimental setup for force measurement is shown in (c) [© 2022 IEEE].

71 kPa, respectively, for type D [see Fig. 6.19(d)] actuator. The material of type A and C actuators was less stiff than type B and D actuators. Owing to the large deformation gradient value of air chambers, the solvers stopped prematurely at pressure magnitudes beyond this limit.

Uniform Air Chamber Geometry Actuators (non-zero vertical offset at tip)

The analytical computations and experiments were performed for different contact offsets at the tip. The experiments were performed for four different offsets, i.e., 10, 20, -10, and -20 mm. A schematic of the experimental setup is shown in Fig. 6.20. The force results are presented in Fig. 6.21. The force values predicted by the analytical model are close to the experimental force values. However, the analytical model model cannot predict the force value for negative offset after a certain air pressure magnitude. This happens due to the solver. The solver gives a solution that satisfies the boundary conditions but is practically infeasible.

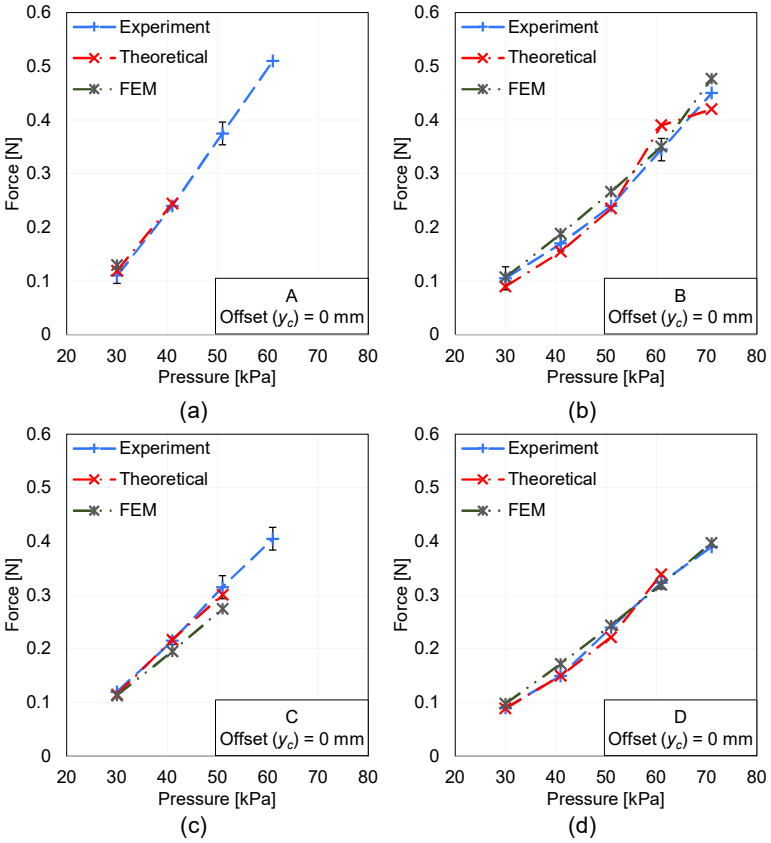

Fig. 6.19 Theoretical, FEM and experimental blocked force plots of (a) type A, (b) type B, (c) type C, and (d) type D actuators. Error bars indicate the standard deviation among 2 trials [© 2022 IEEE].

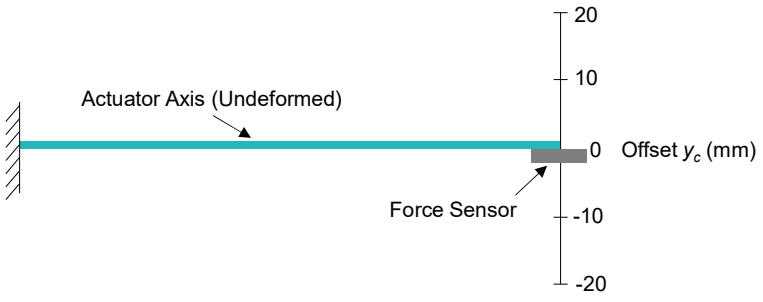

Fig. 6.20 Schematic of force measuring experiment for non-zero vertical offset at tip [© 2022 IEEE].

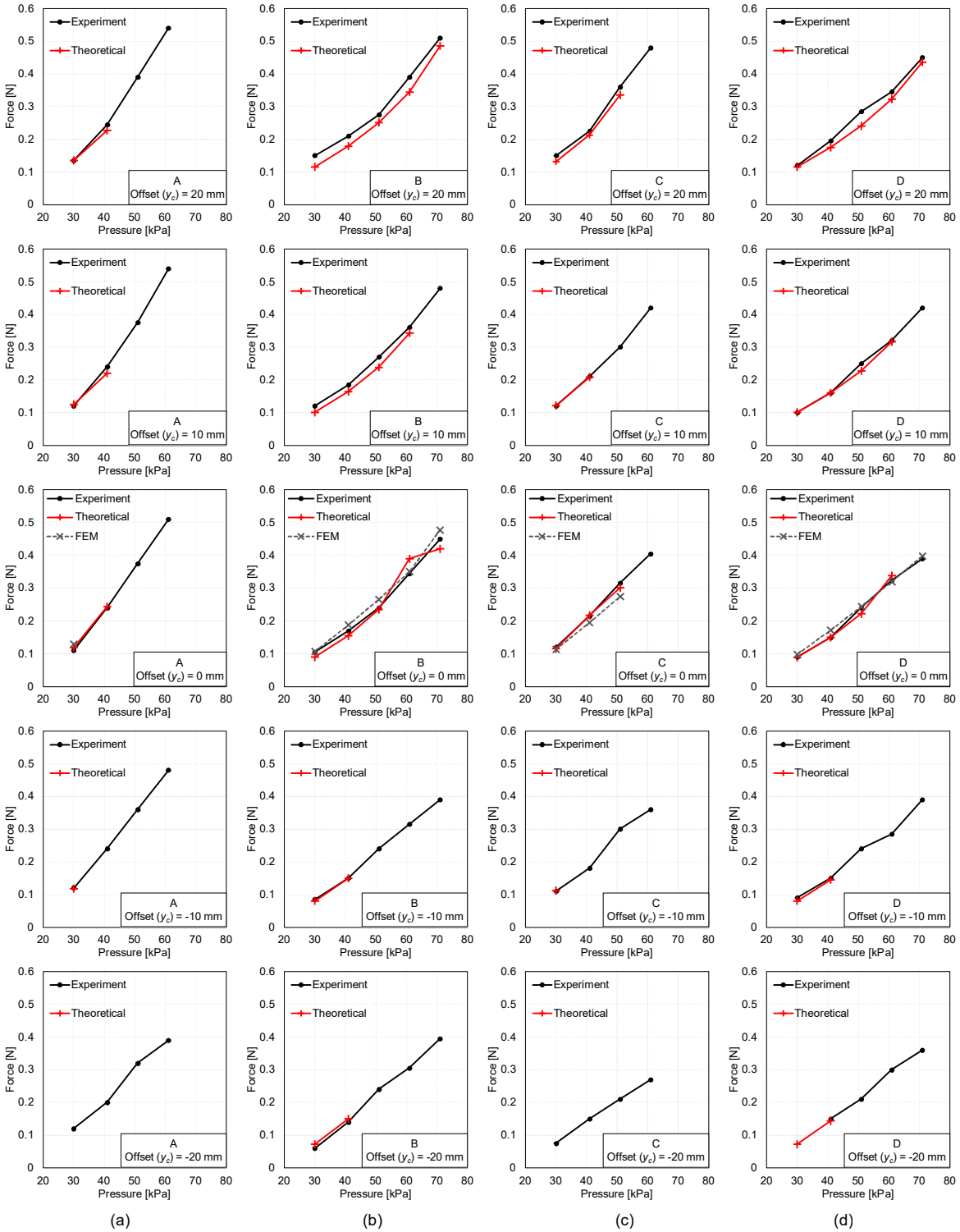

Fig. 6.21 Theoretical and experimental blocked force plots of (a) type A, (b) type B, (c) type C, and (d) type D actuators, at different offset heights y_c [© 2022 IEEE].

Uniform Air Chamber Geometry Actuators Having Different Length (parallel contact)

The blocked force simulation results for actuators having different lengths (see Subsection-6.3.1 for details on actuator lengths) for 0 mm tip offset are presented in Fig. 6.22. Based on the observed behavior, we can conclude that the developed model can be applied to actuators having different lengths.

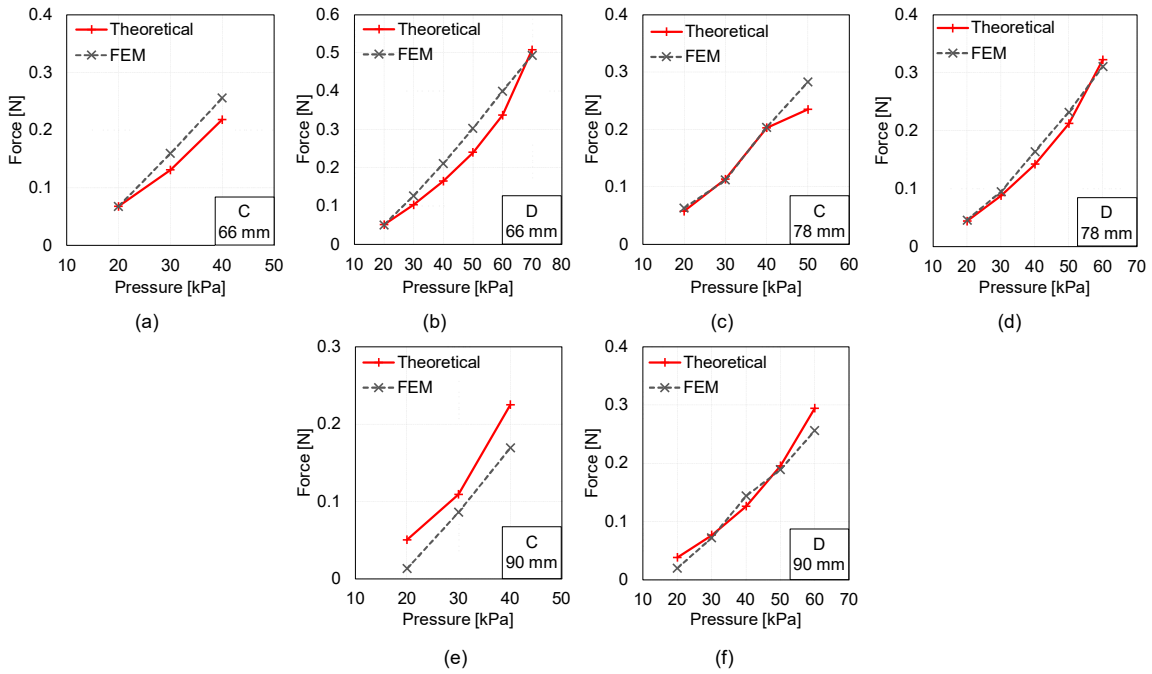

Fig. 6.22 Theoretical and FEM blocked force plots of (a) type C 66 mm, (b) type D 66 mm, (c) type C 78 mm, (d) type D 78 mm, (e) type C 90 mm, and (f) type D 90 mm actuators [© 2022 IEEE].

Blocked Force Deformation of Uniform Air Chamber Geometry Actuators (parallel contact)

The experimental, theoretical, and FE simulated blocked force deformation plots of the actuators are presented in Fig. 6.23. The analytical model overestimates the deformation, whereas the FE simulated deformation is closer to the experimental deformation. This occurs because of the additional stiffness provided by the air chambers to the actuator cover. In analytical model, this bending stiffness is not considered. This is a limitation of the current model.

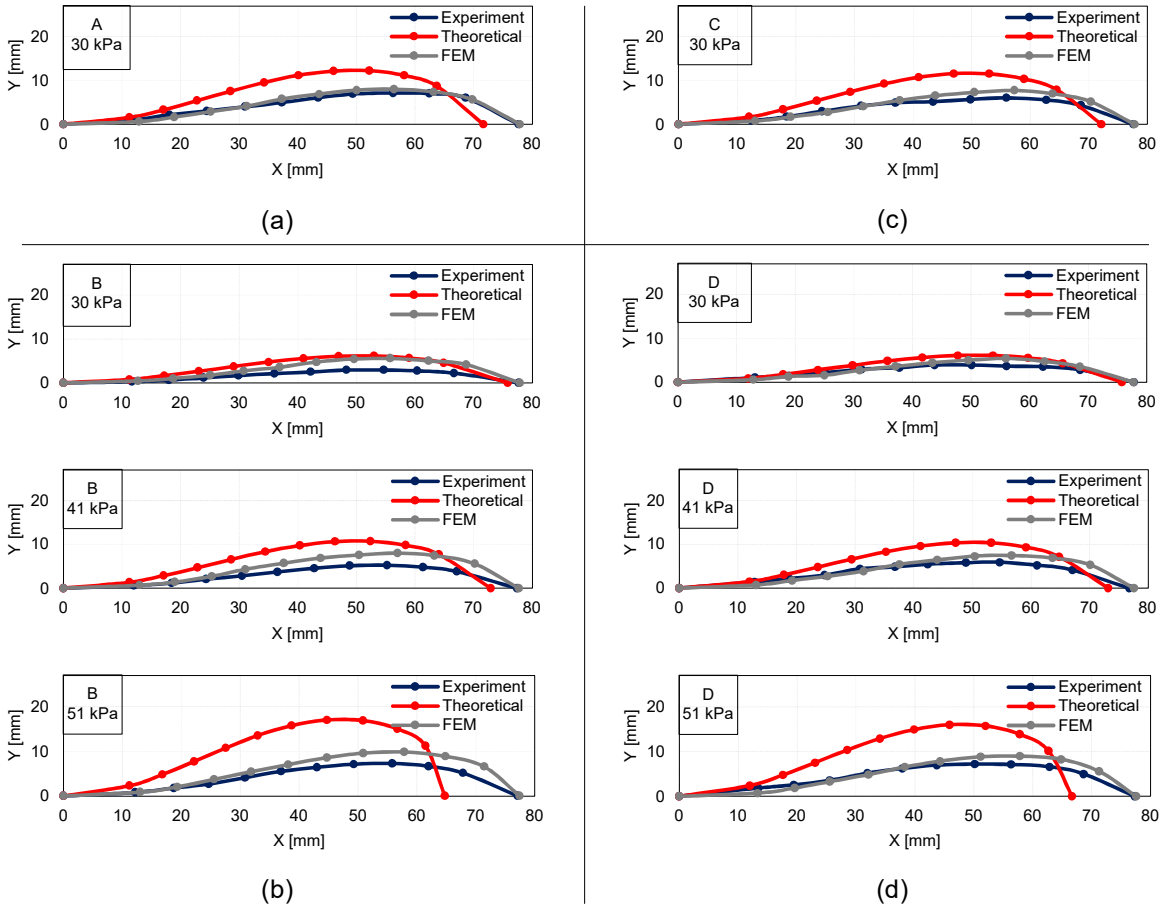

Fig. 6.23 Blocked force deformation plots of (a) type A, (b) type B, (c) type C, and (d) type D actuators [© 2022 IEEE].

6.3.3 Grasping

The analytical model predicted air pressure required to grasp the objects is presented in Table 6.3. The COF between the grasping objects (PLA) and actuators was taken as 0.96. Snapshots of the grasping experiment for type A actuator are shown in Fig. 6.24. The gripper was able to lift the circular cylinder and 3-face cone at the predicted pressure. The type B gripper (see Fig. 6.25) was able to lift the hexagonal and circular cylinders. The type C gripper (see Fig. 6.26) was able to lift the hexagonal cylinder, circular cylinder, and 3-face cone. The type D gripper (see Fig. 6.27) was able to lift the hexagonal and circular cylinders. However, the grasps were unstable. The predicted pressure is the minimum pressure required for grasping. In experiments, we did not consider any factor of safety on the predicted pressure. If a certain magnitude factor of safety would be considered, then successful grasps can be attained by the grippers. In addition, the air pressure is predicted for static case, and

Table 6.3 Analytical Model Predicted Air Pressure for Three-Finger Pneu-net Grippers [© 2022 IEEE]

Grasping Objects	**Mass** m_h(g)	**Pressure required by actuators** p (kPa)			
		A	**B**	**C**	**D**
Hexagonal Cylinder	35	—	42	37	43
Circular Cylinder	26	28	32	28	32
3-Face Cone	19	28	33	29	33
Circular Cone	20	25	29	25	29

in experiments, we moved the gripper vertically to lift the objects. This dynamic effect is also a factor contributing to the unsuccessful grasps.

The 3-face and right circular cones have a tapered geometry, which was considered while estimating the pressure, but the grippers failed to lift the circular cone. This occurs because of the contact condition at the cone surface and actuator tip. A full edge contact occurred at the surface of 3-face cone, while it did not occur for the circular cone. Moreover, the COF for an inclined surface might be different from that of a planar surface.

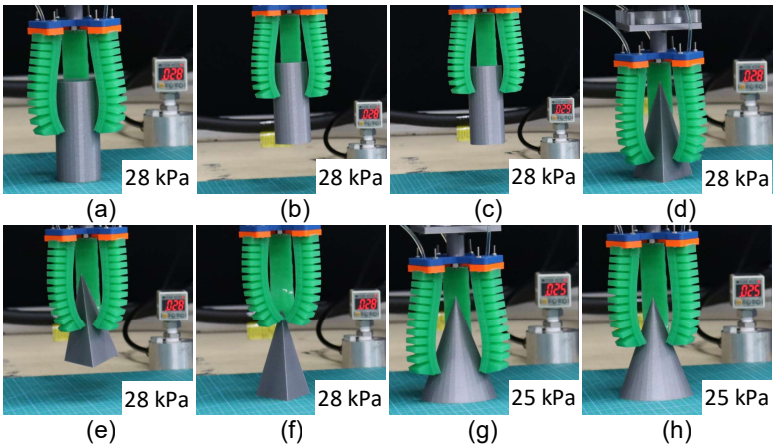

Fig. 6.24 Photo snapshots of grasping experiment for type A actuator. The experiments were performed to grasp a circular cylinder (a, b, and c), 3-face cone (d, e, and f), and circular cone (g, h) [© 2022 IEEE].

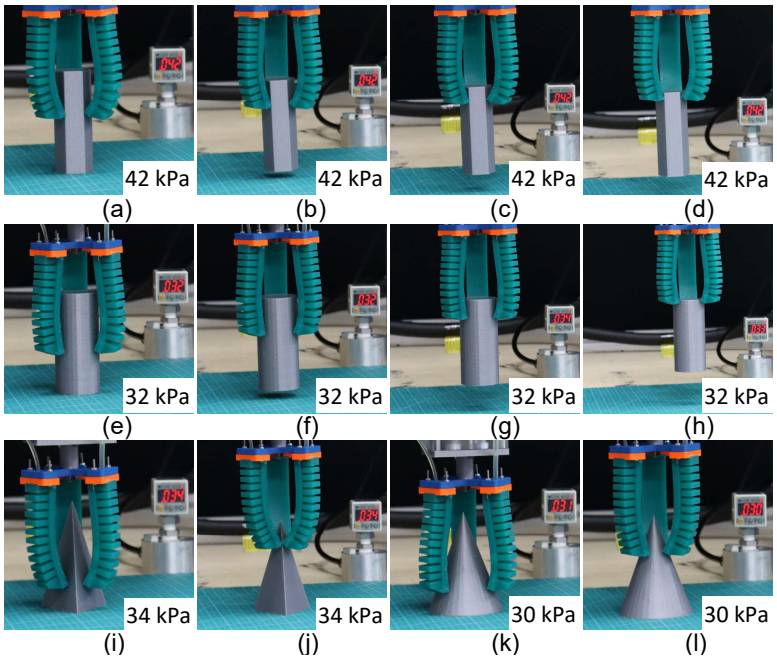

Fig. 6.25 Photo snapshots of grasping experiment for type B actuator. The experiments were performed to grasp a hexagonal cylinder (a, b, c, and d), circular cylinder (e, f, g, and h), 3-face cone (i, j), and circular cone (k, l) [© 2022 IEEE].

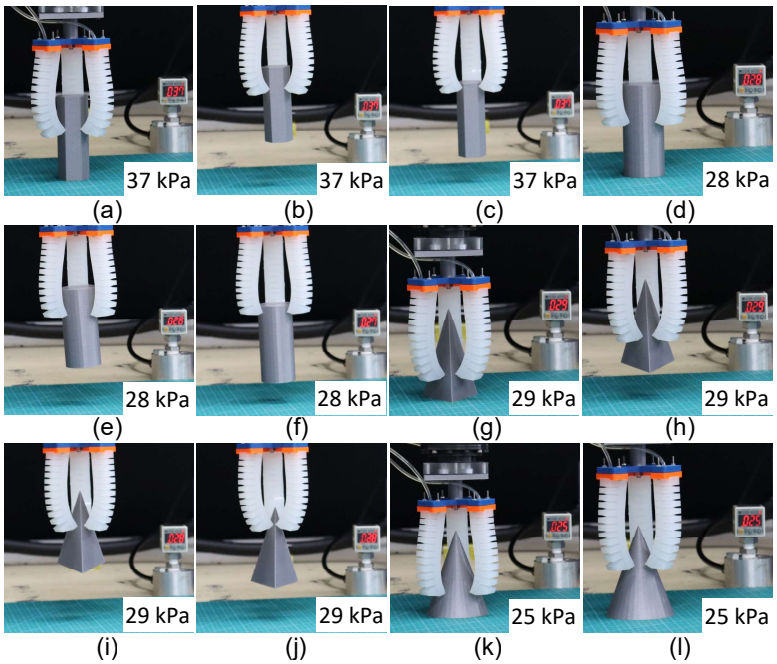

Fig. 6.26 Photo snapshots of grasping experiment for type C actuator. The experiments were performed to grasp a hexagonal cylinder (a, b, and c), circular cylinder (d, e, and f), 3-face cone (g, h, i, and j), and circular cone (k, l) [© 2022 IEEE].

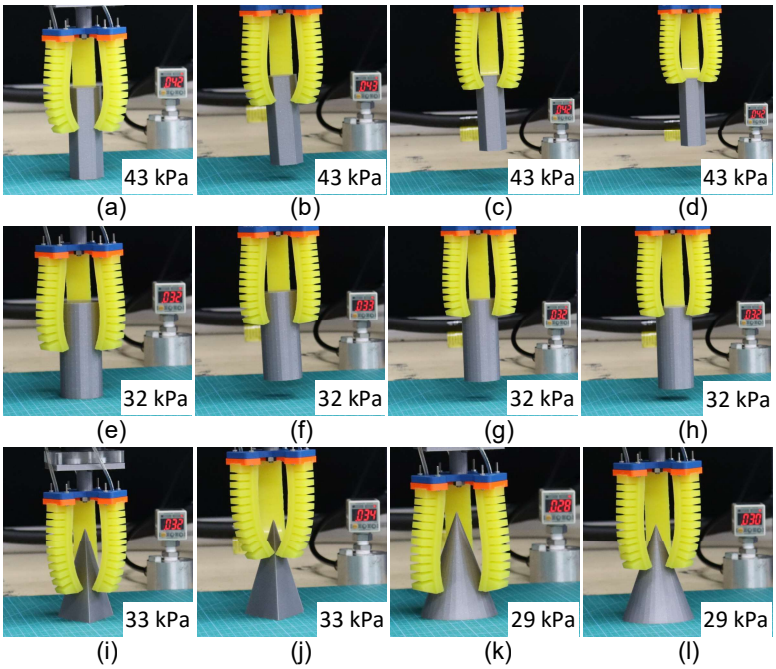

Fig. 6.27 Photo snapshots of grasping experiment for type D actuator. The experiments were performed to grasp a hexagonal cylinder (a, b, c, and d), circular cylinder (e, f, g, and h), 3-face cone (i, j), and circular cone (k, l) [© 2022 IEEE].

Chapter 7

Conclusion and Future Work

7.1 Conclusion

The work presented in this dissertation is focused on the modeling of pneumatic soft actuators. An analytical modeling approach for a flat shell and a pneu-net actuator is presented. The main contributions of our current work are as follows:

- The developed models predict deformation and force characteristics of the actuators. The force characteristics are important for defining the weight-lifting capabilities of actuators.

- The model for the flat shell gripper considers both full and cylindrical contact scenarios. The grasp dependency of cylindrical object on vertical offset parameter h is investigated. The vertical offset is a crucial parameter for the gripper to pick objects. The model provides a relationship between the vertical offset h and other parameters. For cylindrical objects, this parameter can be used to effectively place the gripper with respect to the object. The grasping test provides insight into the effect of h on the grasps. The modeling approach can be further extended to investigate the interaction of the actuator with other surfaces.

- The model can also be used to define the grasping capabilities of flat shell gripper in terms of the minimum size of object that it can grasp. Based on the deformed membrane profile, the minimum size of object being grasped by the gripper can be predicted using the smaller dimension a of the membrane. This kind of relationship between deformed profile of actuator and size of grasping object is usually absent in grippers made of rigid finger-tips but for membrane based grippers it is important to consider this behavior.

- The eccentric contact model of the flat shell gripper is applied to predict pressure required to resist tilting behavior of the object.

- The pneu-net actuator model considers axial stretch, which is generally not considered in bending actuators in other studies; however, it is an important aspect for gait-type soft robots. A brief survey on the features of existing models of pneu-net actuators is presented in Table 1.1.

- The modeling of pneu-net actuator air chambers is based on finite-strain membrane theory and contact mechanics approach. The developed model considers geometric variations in the design of air chambers. Apart from air chamber geometry, the pneu-net actuators used for grasping applications usually have a flat base. Hence, the presented rectangular cross-section beam-based model can be applied to the majority of such actuators. Theoretically, a similar modeling approach can be implemented for actuators having geometric design other than the pneu-net actuator, such as cylindrical and ribbed-type actuators [1]. By modifying the air chamber model, the actuators can be modeled using a similar approach. In contrast to constant curvature models of the actuator that predict either deformation or force characteristics, the developed model predicts the deformation and force characteristics simultaneously for the grasping state.

- In grasping experiments, we used two-finger shell and three-finger pneu-net grippers; however, the same modeling approach can be used for other configurations as well, i.e., modular design. In grasping experiments for the pneu-net gripper, we considered standard geometry objects, but the model can be applied to grasp arbitrarily shaped objects if the outer boundary and weight of the objects are known.

- The developed models are efficient in terms of computation time because they consist of nonlinear algebraic and differential equations as the final governing equations. The presented solution strategy is effective for solving the equations numerically, using a boundary value problem and a nonlinear algebraic equation solver.

- The presented models are abstract and do not require a CAD file for simulations. They only require geometric and material parameter values. They can be used with other optimization techniques to find the best-fit design parameters from a large design space (i.e., initial design) as they are more than a hundred times faster than FE models and do not need a new CAD file for each iteration.

- The material properties of elastomers are not fixed and in the developed models we can easily tune them to best fit the experimental deformation behavior. As an example,

we can tune the material parameters for free space deformation and then use them to predict the force behavior, as we did for the flat shell gripper. For the pneu-net actuator simulations, we used the experimentally calculated material parameters. But if we tune the deformation behavior by varying the material parameters then we can further reduce the model prediction error.

- The presented work also provides an insight on frictional properties of the actuators. The frictional properties vary with contact interface between the actuators and grasping objects.

- In applications, the developed models can be used to predict the air pressure required to attain a successful grasp.

As a limitation, the presented models do not consider gripper misalignment and asymmetric object grasp; however, in practice, such grasping conditions are also encountered. For the pneu-net actuator, in the presence of large deformation gradient, the solver terminated prematurely. This occurs because of the solver's internal function tolerances, which results in an unexpected solution. The model fails to predict the air pressure required for grasping circular cone even after considering the tapered geometry at contact. This is due to the lesser edge contact of the actuator tip at circular cone surface when compared with the contact at 3-face cone surface. The pneu-net actuator model does not consider the stiffness associated with air chambers.

From soft robotics perspective, the presented work enriches the modeling of soft robots and provides another way to model soft actuators. With the help of a modeling tool we can explore a larger design space. The presented work highlights the application of large strain beam and large strain membrane theories to soft robots. The presented design approach can be extended to facilitate the design of other soft robots.

7.2 Future Work

Future work could involve the optimization of flat shell actuator geometry for force and vertical offset h. The contact with the cylindrical substrate model can be further extended to study the manipulation of a cylindrical object by reducing the pressure for an eccentric grasp. In the pneu-net actuator model, we developed the finite-strain air chamber model using square membrane assumption and then used stretch mapping to predict the behavior of rectangular membrane. In future, as a scope for improvement, the air chambers could be modeled using the rectangular membrane model developed for the flat shell actuator. The models could also be further extended to study the interaction of the actuators with soft objects and dynamic behavior of the actuators.

References

[1] P. Glick, S. A. Suresh, D. Ruffatto, M. Cutkosky, M. T. Tolley, and A. Parness, "A soft robotic gripper with gecko-inspired adhesive," *IEEE Robotics and Automation Letters*, vol. 3, no. 2, pp. 903–910, 2018.

[2] J. Shintake, V. Cacucciolo, D. Floreano, and H. Shea, "Soft robotic grippers," *Advanced Materials*, vol. 30, no. 29, 2018, Art. no. 1707035.

[3] P. Polygerinos, N. Correll, S. A. Morin, B. Mosadegh, C. D. Onal, K. Petersen, M. Cianchetti, M. T. Tolley, and R. F. Shepherd, "Soft robotics: Review of fluid-driven intrinsically soft devices; manufacturing, sensing, control, and applications in human-robot interaction," *Advanced Engineering Materials*, vol. 19, no. 12, 2017, Art. no. 1700016.

[4] B. Gorissen, D. Reynaerts, S. Konishi, K. Yoshida, J.-W. Kim, and M. De Volder, "Elastic inflatable actuators for soft robotic applications," *Advanced Materials*, vol. 29, no. 43, 2017, Art. no. 1604977.

[5] J. Walker, T. Zidek, C. Harbel, S. Yoon, F. S. Strickland, S. Kumar, and M. Shin, "Soft robotics: a review of recent developments of pneumatic soft actuators," in *Actuators*, vol. 9, no. 1. Multidisciplinary Digital Publishing Institute, 2020, Art. no. 3.

[6] Z. Wang, D. S. Chathuranga, and S. Hirai, "3d printed soft gripper for automatic lunch box packing," in *2016 IEEE International Conference on Robotics and Biomimetics (ROBIO)*. IEEE, 2016, pp. 503–508.

[7] Z. Wang, M. Zhu, S. Kawamura, and S. Hirai, "Fabrication and performance comparison of different soft pneumatic actuators for lunch box packaging," in *2017 IEEE International Conference on Real-time Computing and Robotics (RCAR)*. IEEE, 2017, pp. 22–27.

[8] B. Zhang, Y. Xie, J. Zhou, K. Wang, and Z. Zhang, "State-of-the-art robotic grippers, grasping and control strategies, as well as their applications in agricultural robots: A review," *Computers and Electronics in Agriculture*, vol. 177, 2020, Art. no. 105694.

[9] K. C. Galloway, K. P. Becker, B. Phillips, J. Kirby, S. Licht, D. Tchernov, R. J. Wood, and D. F. Gruber, "Soft robotic grippers for biological sampling on deep reefs," *Soft robotics*, vol. 3, no. 1, pp. 23–33, 2016.

[10] M. Cianchetti, M. Calisti, L. Margheri, M. Kuba, and C. Laschi, "Bioinspired locomotion and grasping in water: the soft eight-arm octopus robot," *Bioinspiration & biomimetics*, vol. 10, no. 3, 2015, Art. no. 035003.

[11] T. Ranzani, G. Gerboni, M. Cianchetti, and A. Menciassi, "A bioinspired soft manipulator for minimally invasive surgery," *Bioinspiration & biomimetics*, vol. 10, no. 3, 2015, Art. no. 035008.

[12] K. Suzumori, S. Iikura, and H. Tanaka, "Applying a flexible microactuator to robotic mechanisms," *IEEE Control systems magazine*, vol. 12, no. 1, pp. 21–27, 1992.

[13] R. Deimel and O. Brock, "A novel type of compliant and underactuated robotic hand for dexterous grasping," *The International Journal of Robotics Research*, vol. 35, no. 1-3, pp. 161–185, 2016.

[14] B. Mosadegh, P. Polygerinos, C. Keplinger, S. Wennstedt, R. F. Shepherd, U. Gupta, J. Shim, K. Bertoldi, C. J. Walsh, and G. M. Whitesides, "Pneumatic networks for soft robotics that actuate rapidly," *Advanced functional materials*, vol. 24, no. 15, pp. 2163–2170, 2014.

[15] R. V. Martinez, C. R. Fish, X. Chen, and G. M. Whitesides, "Elastomeric origami: programmable paper-elastomer composites as pneumatic actuators," *Advanced functional materials*, vol. 22, no. 7, pp. 1376–1384, 2012.

[16] H. Zhao, K. O'Brien, S. Li, and R. F. Shepherd, "Optoelectronically innervated soft prosthetic hand via stretchable optical waveguides," *Science robotics*, vol. 1, no. 1, 2016, Art. no. eaai7529.

[17] A. Koivikko, E. S. Raei, M. Mosallaei, M. Mäntysalo, and V. Sariola, "Screen-printed curvature sensors for soft robots," *IEEE Sensors Journal*, vol. 18, no. 1, pp. 223–230, 2017.

[18] K. C. Galloway, P. Polygerinos, C. J. Walsh, and R. J. Wood, "Mechanically programmable bend radius for fiber-reinforced soft actuators," in *2013 16th International Conference on Advanced Robotics (ICAR)*. IEEE, 2013, pp. 1–6.

[19] F. Connolly, P. Polygerinos, C. J. Walsh, and K. Bertoldi, "Mechanical programming of soft actuators by varying fiber angle," *Soft Robotics*, vol. 2, no. 1, pp. 26–32, 2015.

[20] Y. Li, Y. Chen, Y. Yang, and Y. Wei, "Passive particle jamming and its stiffening of soft robotic grippers," *IEEE Transactions on robotics*, vol. 33, no. 2, pp. 446–455, 2017.

[21] Y. Yang, Y. Chen, Y. Li, Z. Wang, and Y. Li, "Novel variable-stiffness robotic fingers with built-in position feedback," *Soft robotics*, vol. 4, no. 4, pp. 338–352, 2017.

[22] B. C. Mac Murray, X. An, S. S. Robinson, I. M. van Meerbeek, K. W. O'Brien, H. Zhao, and R. F. Shepherd, "Poroelastic foams for simple fabrication of complex soft robots," *Advanced Materials*, vol. 27, no. 41, pp. 6334–6340, 2015.

[23] A. Argiolas, B. C. Mac Murray, I. Van Meerbeek, J. Whitehead, E. Sinibaldi, B. Mazzolai, and R. F. Shepherd, "Sculpting soft machines," *Soft Robotics*, vol. 3, no. 3, pp. 101–108, 2016.

[24] S. Song and M. Sitti, "Soft grippers using micro-fibrillar adhesives for transfer printing," *Advanced Materials*, vol. 26, no. 28, pp. 4901–4906, 2014.

[25] R. Niiyama, X. Sun, C. Sung, B. An, D. Rus, and S. Kim, "Pouch motors: Printable soft actuators integrated with computational design," *Soft Robotics*, vol. 2, no. 2, pp. 59–70, 2015.

[26] R. MacCurdy, R. Katzschmann, Y. Kim, and D. Rus, "Printable hydraulics: A method for fabricating robots by 3d co-printing solids and liquids," in *2016 IEEE International Conference on Robotics and Automation (ICRA)*. IEEE, 2016, pp. 3878–3885.

[27] Z. Wang, Y. Torigoe, and S. Hirai, "A prestressed soft gripper: design, modeling, fabrication, and tests for food handling," *IEEE Robotics and Automation Letters*, vol. 2, no. 4, pp. 1909–1916, 2017.

[28] D. K. Patel, A. H. Sakhaei, M. Layani, B. Zhang, Q. Ge, and S. Magdassi, "Highly stretchable and uv curable elastomers for digital light processing based 3d printing," *Advanced Materials*, vol. 29, no. 15, 2017, Art. no. 1606000.

[29] C. J. Thrasher, J. J. Schwartz, and A. J. Boydston, "Modular elastomer photoresins for digital light processing additive manufacturing," *ACS applied materials & interfaces*, vol. 9, no. 45, pp. 39 708–39 716, 2017.

[30] J. Wang, Y. Fei, and W. Pang, "Design, modeling, and testing of a soft pneumatic glove with segmented pneunets bending actuators," *IEEE/ASME Transactions on Mechatronics*, vol. 24, no. 3, pp. 990–1001, 2019.

[31] Z. Wang, R. Kanegae, and S. Hirai, "Circular shell gripper for handling food products," *Soft robotics*, vol. 8, no. 5, pp. 542–554, 2021.

[32] Y. Kuriyama, Y. Okino, Z. Wang, and S. Hirai, "A wrapping gripper for packaging chopped and granular food materials," in *2019 2nd IEEE International Conference on Soft Robotics (RoboSoft)*. IEEE, 2019, pp. 114–119.

[33] N. Chavan-Dafie, K. Lee, and A. Rodriguez, "Pneumatic shape-shifting fingers to reorient and grasp," in *2018 IEEE 14th International Conference on Automation Science and Engineering (CASE)*. IEEE, 2018, pp. 988–993.

[34] K. P. Becker, N. W. Bartlett, M. J. Malley, P. M. Kjeer, and R. J. Wood, "Tunable friction through constrained inflation of an elastomeric membrane," in *2017 IEEE International Conference on Robotics and Automation (ICRA)*. IEEE, 2017, pp. 4352–4357.

[35] H. Choi and M. Koc, "Design and feasibility tests of a flexible gripper based on inflatable rubber pockets," *International Journal of Machine Tools and Manufacture*, vol. 46, no. 12-13, pp. 1350–1361, 2006.

[36] R. Kanegae, Z. Wang, and S. Hirai, "Easily fabricatable shell gripper for packaging multiple cucumbers simultaneously," in *2020 IEEE International Conference on Real-time Computing and Robotics (RCAR)*. IEEE, 2020, pp. 188–192.

[37] Y. Makiyama, Z. Wang, and S. Hirai, "A pneumatic needle gripper for handling shredded food products," in *2020 IEEE International Conference on Real-time Computing and Robotics (RCAR)*. IEEE, 2020, pp. 183–187.

[38] P. Rothemund, A. Ainla, L. Belding, D. J. Preston, S. Kurihara, Z. Suo, and G. M. Whitesides, "A soft, bistable valve for autonomous control of soft actuators," *Science Robotics*, vol. 3, no. 16, 2018.

[39] N. Kuppuswamy, A. Alspach, A. Uttamchandani, S. Creasey, T. Ikeda, and R. Tedrake, "Soft-bubble grippers for robust and perceptive manipulation," in *2020 IEEE/RSJ International Conference on Intelligent Robots and Systems (IROS)*. IEEE, 2020, pp. 9917–9924.

[40] J. Amend, N. Cheng, S. Fakhouri, and B. Culley, "Soft robotics commercialization: Jamming grippers from research to product," *Soft robotics*, vol. 3, no. 4, pp. 213–222, 2016.

[41] S. Song, D.-M. Drotlef, D. Son, A. Koivikko, and M. Sitti, "Adaptive self-sealing suction-based soft robotic gripper," *Advanced science*, vol. 8, no. 17, 2021, Art. no. 2100641.

[42] A. Zolfagharian, M. P. Mahmud, S. Gharaie, M. Bodaghi, A. Z. Kouzani, and A. Kaynak, "3d/4d-printed bending-type soft pneumatic actuators: fabrication, modelling, and control," *Virtual and Physical Prototyping*, vol. 15, no. 4, pp. 373–402, 2020.

[43] P. Polygerinos, S. Lyne, Z. Wang, L. F. Nicolini, B. Mosadegh, G. M. Whitesides, and C. J. Walsh, "Towards a soft pneumatic glove for hand rehabilitation," in *2013 IEEE/RSJ International Conference on Intelligent Robots and Systems*. IEEE, 2013, pp. 1512–1517.

[44] J. Shintake, H. Sonar, E. Piskarev, J. Paik, and D. Floreano, "Soft pneumatic gelatin actuator for edible robotics," in *2017 IEEE/RSJ International Conference on Intelligent Robots and Systems (IROS)*. IEEE, 2017, pp. 6221–6226.

[45] B. S. Homberg, R. K. Katzschmann, M. R. Dogar, and D. Rus, "Robust proprioceptive grasping with a soft robot hand," *Autonomous Robots*, vol. 43, no. 3, pp. 681–696, 2019.

[46] J.-H. Low, I. Delgado-Martinez, and C.-H. Yeow, "Customizable soft pneumatic chamber–gripper devices for delicate surgical manipulation," *Journal of Medical Devices*, vol. 8, no. 4, 2014.

[47] J. Zhou, S. Chen, and Z. Wang, "A soft-robotic gripper with enhanced object adaptation and grasping reliability," *IEEE Robotics and automation letters*, vol. 2, no. 4, pp. 2287–2293, 2017.

[48] Y. Hao, T. Wang, Z. Ren, Z. Gong, H. Wang, X. Yang, S. Guan, and L. Wen, "Modeling and experiments of a soft robotic gripper in amphibious environments," *International Journal of Advanced Robotic Systems*, vol. 14, no. 3, 2017, Art. no. 1729881417707148.

[49] T. Wang, L. Ge, and G. Gu, "Programmable design of soft pneu-net actuators with oblique chambers can generate coupled bending and twisting motions," *Sensors and Actuators A: Physical*, vol. 271, pp. 131–138, 2018.

[50] M. Zhu, Y. Mori, T. Wakayama, A. Wada, and S. Kawamura, "A fully multi-material three-dimensional printed soft gripper with variable stiffness for robust grasping," *Soft robotics*, vol. 6, no. 4, pp. 507–519, 2019.

[51] L. Rosalia, B. W.-K. Ang, and R. C.-H. Yeow, "Geometry-based customization of bending modalities for 3d-printed soft pneumatic actuators," *IEEE Robotics and Automation Letters*, vol. 3, no. 4, pp. 3489–3496, 2018.

[52] R. B. Scharff, J. Wu, J. M. Geraedts, and C. C. Wang, "Reducing out-of-plane deformation of soft robotic actuators for stable grasping," in *2019 2nd IEEE International Conference on Soft Robotics (RoboSoft)*. IEEE, 2019, pp. 265–270.

[53] R. L. Truby, R. K. Katzschmann, J. A. Lewis, and D. Rus, "Soft robotic fingers with embedded ionogel sensors and discrete actuation modes for somatosensitive manipulation," in *2019 2nd IEEE International Conference on Soft Robotics (RoboSoft)*. IEEE, 2019, pp. 322–329.

[54] W. Park, S. Seo, and J. Bae, "A hybrid gripper with soft material and rigid structures," *IEEE Robotics and Automation Letters*, vol. 4, no. 1, pp. 65–72, 2018.

[55] T. Sun, Y. Chen, T. Han, C. Jiao, B. Lian, and Y. Song, "A soft gripper with variable stiffness inspired by pangolin scales, toothed pneumatic actuator and autonomous controller," *Robotics and Computer-Integrated Manufacturing*, vol. 61, 2020, Art. no. 101848.

[56] B. S. Homberg, R. K. Katzschmann, M. R. Dogar, and D. Rus, "Haptic identification of objects using a modular soft robotic gripper," in *2015 IEEE/RSJ International Conference on Intelligent Robots and Systems (IROS)*. IEEE, 2015, pp. 1698–1705.

[57] J. H. Low, W. W. Lee, P. M. Khin, S. L. Kukreja, H. Ren, N. V. Thakor, and C.-H. Yeow, "A compliant modular robotic hand with fabric force sensor for multiple versatile grasping modes," in *2016 6th IEEE International Conference on Biomedical Robotics and Biomechatronics (BioRob)*. IEEE, 2016, pp. 1230–1235.

[58] Y. Yang, Y. Chen, Y. Li, M. Z. Chen, and Y. Wei, "Bioinspired robotic fingers based on pneumatic actuator and 3d printing of smart material," *Soft robotics*, vol. 4, no. 2, pp. 147–162, 2017.

[59] A. M. Nasab, A. Sabzehzar, M. Tatari, C. Majidi, and W. Shan, "A soft gripper with rigidity tunable elastomer strips as ligaments," *Soft robotics*, vol. 4, no. 4, pp. 411–420, 2017.

[60] Y. Hao, J. Gao, Y. Lv, and J. Liu, "Low melting point alloys enabled stiffness tunable advanced materials," *Advanced Functional Materials*, 2022, Art. no. 2201942.

[61] Y. Hao, Z. Gong, Z. Xie, S. Guan, X. Yang, Z. Ren, T. Wang, and L. Wen, "Universal soft pneumatic robotic gripper with variable effective length," in *2016 35th Chinese control conference (CCC)*. IEEE, 2016, pp. 6109–6114.

[62] H. Yuk, S. Lin, C. Ma, M. Takaffoli, N. X. Fang, and X. Zhao, "Hydraulic hydrogel actuators and robots optically and sonically camouflaged in water," *Nature communications*, vol. 8, no. 1, pp. 1–12, 2017.

[63] S. Walker, J. Rueben, T. V. Volkenburg, S. Hemleben, C. Grimm, J. Simonsen, and Y. Mengüç, "Using an environmentally benign and degradable elastomer in soft robotics," *International Journal of Intelligent Robotics and Applications*, vol. 1, no. 2, pp. 124–142, 2017.

[64] S. Terryn, J. Brancart, D. Lefeber, G. Van Assche, and B. Vanderborght, "Self-healing soft pneumatic robots," *Science Robotics*, vol. 2, no. 9, p. eaan4268, 2017, Art. no. eaan4268.

[65] A. D. Marchese, R. K. Katzschmann, and D. Rus, "A recipe for soft fluidic elastomer robots," *Soft robotics*, vol. 2, no. 1, pp. 7–25, 2015.

[66] D. Trivedi, C. D. Rahn, W. M. Kier, and I. D. Walker, "Soft robotics: Biological inspiration, state of the art, and future research," *Applied bionics and biomechanics*, vol. 5, no. 3, pp. 99–117, 2008.

[67] D. Rus and M. T. Tolley, "Design, fabrication and control of soft robots," *Nature*, vol. 521, no. 7553, pp. 467–475, 2015.

[68] L. Hines, K. Petersen, G. Z. Lum, and M. Sitti, "Soft actuators for small-scale robotics," *Advanced materials*, vol. 29, no. 13, 2017, Art. no. 1603483.

[69] C. Yang, R. Kang, D. T. Branson, L. Chen, and J. S. Dai, "Kinematics and statics of eccentric soft bending actuators with external payloads," *Mechanism and Machine Theory*, vol. 139, pp. 526–541, 2019.

[70] P. Paoletti, G. Jones, and L. Mahadevan, "Grasping with a soft glove: intrinsic impedance control in pneumatic actuators," *Journal of The Royal Society Interface*, vol. 14, no. 128, 2017, Art. no. 20160867.

[71] F. Connolly, C. J. Walsh, and K. Bertoldi, "Automatic design of fiber-reinforced soft actuators for trajectory matching," *Proceedings of the National Academy of Sciences*, vol. 114, no. 1, pp. 51–56, 2017.

[72] A. Garriga-Casanovas, I. Collison, and F. Rodriguez y Baena, "Toward a common framework for the design of soft robotic manipulators with fluidic actuation," *Soft robotics*, vol. 5, no. 5, pp. 622–649, 2018.

[73] R. J. Webster III and B. A. Jones, "Design and kinematic modeling of constant curvature continuum robots: A review," *The International Journal of Robotics Research*, vol. 29, no. 13, pp. 1661–1683, 2010.

[74] G. Alici, T. Canty, R. Mutlu, W. Hu, and V. Sencadas, "Modeling and experimental evaluation of bending behavior of soft pneumatic actuators made of discrete actuation chambers," *Soft robotics*, vol. 5, no. 1, pp. 24–35, 2018.

[75] B. Gorissen, W. Vincentie, F. Al-Bender, D. Reynaerts, and M. De Volder, "Modeling and bonding-free fabrication of flexible fluidic microactuators with a bending motion," *Journal of Micromechanics and Microengineering*, vol. 23, no. 4, 2013, Art. no. 045012.

[76] Y. Shapiro, A. Wolf, and K. Gabor, "Bi-bellows: Pneumatic bending actuator," *Sensors and Actuators A: Physical*, vol. 167, no. 2, pp. 484–494, 2011.

[77] G. Zhong, Y. Hou, and W. Dou, "A soft pneumatic dexterous gripper with convertible grasping modes," *International Journal of Mechanical Sciences*, vol. 153, pp. 445–456, 2019.

[78] G. Runge, M. Wiese, L. Günther, and A. Raatz, "A framework for the kinematic modeling of soft material robots combining finite element analysis and piecewise constant curvature kinematics," in *2017 3rd International Conference on Control, Automation and Robotics (ICCAR)*. IEEE, 2017, pp. 7–14.

[79] S. Sadati, S. E. Naghibi, A. Shiva, Y. Noh, A. Gupta, I. D. Walker, K. Althoefer, and T. Nanayakkara, "A geometry deformation model for braided continuum manipulators," *Frontiers in Robotics and AI*, vol. 4, 2017, Art. no. 22.

[80] D. Trivedi, A. Lotfi, and C. D. Rahn, "Geometrically exact models for soft robotic manipulators," *IEEE Transactions on Robotics*, vol. 24, no. 4, pp. 773–780, 2008.

[81] N. Giri and I. D. Walker, "Three module lumped element model of a continuum arm section," in *2011 IEEE/RSJ International Conference on Intelligent Robots and Systems*. IEEE, 2011, pp. 4060–4065.

[82] S. Wakimoto, K. Suzumori, and K. Ogura, "Miniature pneumatic curling rubber actuator generating bidirectional motion with one air-supply tube," *Advanced Robotics*, vol. 25, no. 9-10, pp. 1311–1330, 2011.

[83] P. Polygerinos, Z. Wang, J. T. Overvelde, K. C. Galloway, R. J. Wood, K. Bertoldi, and C. J. Walsh, "Modeling of soft fiber-reinforced bending actuators," *IEEE Transactions on Robotics*, vol. 31, no. 3, pp. 778–789, 2015.

[84] Z. Wang and S. Hirai, "Chamber dimension optimization of a bellow-type soft actuator for food material handling," in *2018 IEEE International Conference on Soft Robotics (RoboSoft)*. IEEE, 2018, pp. 382–387.

[85] W. Hu, R. Mutlu, W. Li, and G. Alici, "A structural optimisation method for a soft pneumatic actuator," *robotics*, vol. 7, no. 2, 2018, Art. no. 24.

[86] E. Coevoet, T. Morales-Bieze, F. Largilliere, Z. Zhang, M. Thieffry, M. Sanz-Lopez, B. Carrez, D. Marchal, O. Goury, J. Dequidt *et al.*, "Software toolkit for modeling, simulation, and control of soft robots," *Advanced Robotics*, vol. 31, no. 22, pp. 1208–1224, 2017.

[87] S. E. Navarro, O. Goury, G. Zheng, T. M. Bieze, and C. Duriez, "Modeling novel soft mechanosensors based on air-flow measurements," *IEEE Robotics and Automation Letters*, vol. 4, no. 4, pp. 4338–4345, 2019.

[88] V. Bortnikova, V. Yevsieiev, V. Beskorovainyi, I. Nevliudov, I. Botsman, and S. Maksymova, "Structural parameters influence on a soft robotic manipulator finger bend angle simulation," in *2019 IEEE 15th International Conference on the Experience of Designing and Application of CAD Systems (CADSM)*. IEEE, 2019, pp. 35–38.

[89] Sachin, Z. Wang, and S. Hirai, "Analytical modeling of a soft pneu-net actuator based on finite strain beam theory," in *2021 IEEE/RSJ International Conference on Intelligent Robots and Systems (IROS)*. IEEE, pp. 632–638.

[90] A. Libai and J. G. Simmonds, *The nonlinear theory of elastic shells*. Cambridge university press, 2005.

[91] A. Srivastava and C.-Y. Hui, "Large deformation contact mechanics of long rectangular membranes. i. adhesionless contact," *Proceedings of the Royal Society A: Mathematical, Physical and Engineering Sciences*, vol. 469, no. 2160, 2013, Art. no. 20130424.

[92] Z. Liu, F. Wang, S. Liu, Y. Tian, and D. Zhang, "Modeling and analysis of soft pneumatic network bending actuators," *IEEE/ASME Transactions on Mechatronics*, 2020.

[93] C. Majidi, R. F. Shepherd, R. K. Kramer, G. M. Whitesides, and R. J. Wood, "Influence of surface traction on soft robot undulation," *The International Journal of Robotics Research*, vol. 32, no. 13, pp. 1577–1584, 2013.

[94] G. Cao, B. Chu, and Y. Liu, "Analytical modeling and control of soft fast pneumatic networks actuators," in *IECON 2020 The 46th Annual Conference of the IEEE Industrial Electronics Society*. IEEE, 2020, pp. 2760–2765.

[95] G. Fang, C.-D. Matte, R. B. Scharff, T.-H. Kwok, and C. C. Wang, "Kinematics of soft robots by geometric computing," *IEEE Transactions on Robotics*, vol. 36, no. 4, pp. 1272–1286, 2020.

[96] Q. Xu and J. Liu, "Effective enhanced model for a large deformable soft pneumatic actuator," *Acta Mechanica Sinica*, vol. 36, no. 1, pp. 245–255, 2020.

[97] K. M. de Payrebrune and O. M. O'Reilly, "On constitutive relations for a rod-based model of a pneu-net bending actuator," *Extreme Mechanics Letters*, vol. 8, pp. 38–46, 2016.

[98] G. Gu, D. Wang, L. Ge, and X. Zhu, "Analytical modeling and design of generalized pneu-net soft actuators with three-dimensional deformations," *Soft Robotics*, 2020.

[99] Z. Wang and S. Hirai, "Soft gripper dynamics using a line-segment model with an optimization-based parameter identification method," *IEEE Robotics and Automation Letters*, vol. 2, no. 2, pp. 624–631, 2017.

[100] W. Zhou and Y. Li, "Modeling and analysis of soft pneumatic actuator with symmetrical chambers used for bionic robotic fish," *Soft robotics*, vol. 7, no. 2, pp. 168–178, 2020.

[101] Sachin, Z. Wang, T. Matsuno, and S. Hirai, "Analytical modeling of a membrane-based pneumatic soft gripper," *IEEE Robotics and Automation Letters*, vol. 7, no. 4, pp. 10 359–10 366, 2022.

[102] Sachin, Z. Wang, and S. Hirai, "Analytical modeling of a soft pneu-net actuator subjected to planar tip contact," *IEEE Transactions on Robotics*, vol. 38, no. 5, 2022, doi: 10.1109/TRO.2022.3160048.

[103] B. Storakers, "Variation principles and bounds for the approximate analysis of plane membranes under lateral pressure," *Journal of Applied Mechanics*, vol. 50, no. 4a, pp. 743–749, 1983.

[104] A. Kydoniefs and A. Spencer, "Finite axisymmetric deformations of an initially cylindrical elastic membrane," *The Quarterly Journal of Mechanics and Applied Mathematics*, vol. 22, no. 1, pp. 87–95, 1969.

[105] R. W. Ogden, *Non-linear elastic deformations*. Dover Publication, 1997.

[106] L. He, J. Lou, Y. Dong, S. Kitipornchai, and J. Yang, "Variational modeling of plane-strain hyperelastic thin beams with thickness-stretching effect," *Acta Mechanica*, vol. 229, no. 12, pp. 4845–4861, 2018.

[107] L. E. Dubins, "On plane curves with curvature." *Pacific Journal of Mathematics*, vol. 11, no. 2, pp. 471–481, 1961.

[108] Z. Wang and S. Hirai, "Geometry and material optimization of a soft pneumatic gripper for handling deformable object," in *2018 IEEE International Conference on Robotics and Biomimetics (ROBIO)*. IEEE, 2018, pp. 612–617.

Appendix A

Initial Pressure p_{in} in Algorithm 4

The initial guess pressure p_{in} is defined as the pressure needed to initiate the contact between the gripper and object. Based on the deformed geometry and relative position of the object, the guess pressure can be calculated from the equations for free space state. To initiate contact, the maximum inflation δ of the membrane should be equal to object offset $\delta = d - r$. Now, from membrane inflation δ, the initial arc angle θ_{in} at contact initiation can be calculated from (3.6) as

$$\theta_{in} = 2\tan^{-1}\frac{(d-r)}{a} \ . \tag{A.1}$$

The initial stretch $\lambda_{1_{in}}$ along actuator width can be calculated using (3.5) as

$$\lambda_{1_{in}} = \frac{\theta_{in}}{\sin\theta_{in}} \ . \tag{A.2}$$

The stretch $\lambda_{2_{in}}$ along actuator length can be calculated using (3.1) as

$$\lambda_{2_{in}} = 1 + \frac{a}{b}\left(\lambda_{1_{in}} - 1\right) \ . \tag{A.3}$$

The stretch along the third principal direction can be calculated using (3.2). The radius of curvature R_{in} can be calculated using (3.4) as

$$R_{in} = \frac{a}{\sin\theta_{in}} \ . \tag{A.4}$$

We can then calculate the pressure required to initiate the contact by substituting equation (A.1), (A.2), (A.3), and (A.4) into (3.7) and solving it for p.

Appendix B

Inclined Contact of Square Membrane

The finite-strain model developed in Section-4.3 for the air chambers was tested on a flat shell actuator made of a square membrane. The photo snapshots of the actuator are shown in Fig. B.1. The membrane is made of DS 20 silicone rubber and has a thickness of 1.1 mm and side length 15 mm.

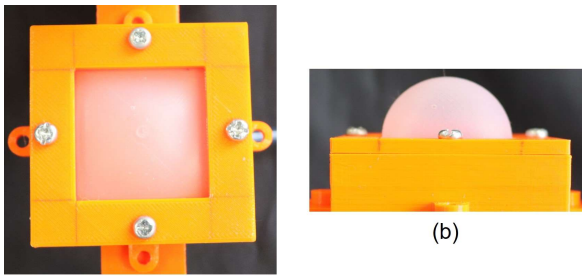

(a) (b)

Fig. B.1 Flat shell actuator made of square membrane. (a) Undeformed state and (b) free-space inflation.

B.1 Contact Widths

The maximum contact width along Z_0-direction exists along the point of contact initiation and it can be calculated by equating the deformed and undeformed length along Z_0-direction; in final form, it can be written as

$$c_z = (c_1 + c_2)\,\frac{a-\rho^*}{a}\,. \tag{B.1}$$

B.2 Contact Force

The contact region between the membrane and substrate is assumed to be elliptical. The area of the elliptical contact region is calculated from the contact widths as

$$A_c = \frac{\pi}{4}(c_1 + c_2)\, c_z \,. \tag{B.2}$$

The contact force is calculated as

$$F_p = p\, A_c \,. \tag{B.3}$$

B.3 Results

B.3.1 Deformed Profile

The deformed profiles of the membrane for $d = 5$ mm and $\theta_s = 10^\circ$ are shown in Fig. B.2 (b) and (c). The dotted black color curve represents the analytical model predicted deformed profile of the membrane and it matches well with the actual profile.

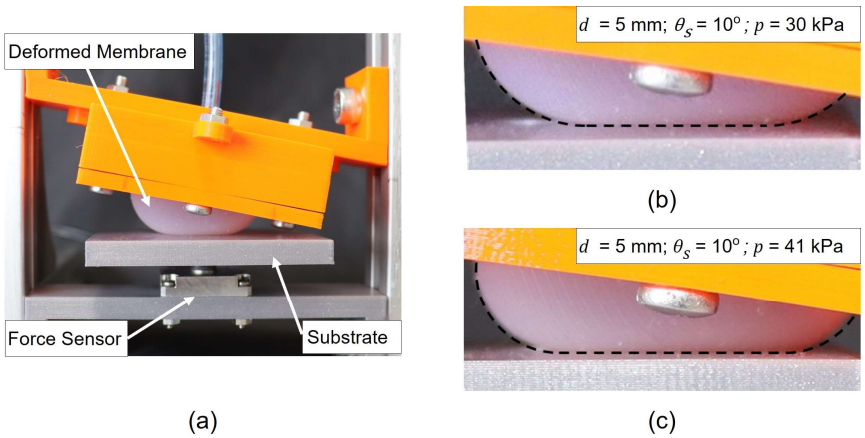

Fig. B.2 (a) Experimental setup for force measurement. Actual and theoretical (dashed curve) deformed profile of square membrane in contact with a 10° inclined substrate at (b) 30 kPa and (c) 41 kPa .

B.3.2 Force

The force characteristics of the membrane in contact with parallel and inclined substrates are shown in Fig. B.3. In simulations, the material properties were chosen from the best fit with

experimental force data. The shear modulus μ of membrane material was taken as 111 kPa. The force results are presented for $d = 5$ mm at $\theta_s = 0^\circ$ and 10° inclinations.

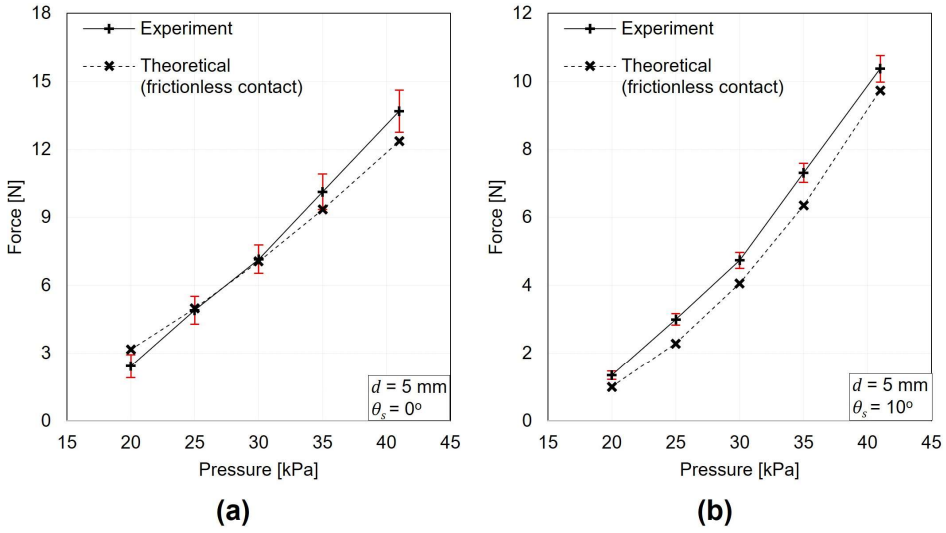

Fig. B.3 Theoretical and experimental force plots for square membrane in contact with a rigid substrate at $d = 5$ mm and inclination angles θ_s (a) 0° and (b) 10°. The error bars are variation among three actuators.